Concurrent Trajectory Optimization and Aircraft Design for the Air Cargo Challenge 2022 Competition

Nuno Miguel Bento de Matos

Thesis to obtain the Master of Science Degree in

Aerospace Engineering

Supervisor: Prof. André Calado Marta

Examination Committee

Chairperson: Prof. Filipe Szolnoky Ramos Pinto Cunha
Supervisor: Prof. André Calado Marta
Member of the Committee: Prof. Alexandra Bento Moutinho

December 2021

To my family and friends.

Acknowledgments

Firstly, I want to thank Instituto Superior Técnico for all the good memories and teachings that shaped my vision of the world and made me always sought for higher levels of knowledge.

A special thanks to Prof. André Marta who was always present in aiding and guiding my journey of producing this thesis.

Also, I want to express my gratitude for all of the Olissipo Air Team members whom will forever have a special place in my heart. They showed me that only together a world can go strong.

Finally, I want to thank my parents and brother for the continuous support and dedication that always motivated me to push through my own limitations. An additionally thank you to my girlfriend who helped and supported me overgrow my barriers and continue to pursue my objectives.

To all my friends who helped me succeed in this journey, thank you for your support and may we keep developing this journey forward.

Resumo

Nesta tese, foi desenvolvida uma ferramenta de otimização de projeto de aeronave aeroestrutural acoplado com trajetória para a competição Air Cargo Challenge 2022 para a obtenção de um projeto conceptual ótimo. A ferramenta desenvolvida usa o *OpenAeroStruct*, um otimizador aeroestrutural de baixa fidelidade que integra o método "vortex-lattice method" como modelo aerodinâmico e um elemento treliça, viga e torção de 1D para o modelo estrutural. Foi adicionado um módulo de otimização de trajetória com a opção de métodos de interpolação b-spline para aumento da eficiência do otimizador. Foram também adicionados dois modelos de propulsão para determinar a resposta propulsiva da aeronave a uma entrada de controlo. A ferramenta tem a possibilidade de controlar a geometria da aeronave (asa e dimensionamento da cauda) e variáveis de estado e controlo (acelerador e incidência do estabilizador), juntamente com prevenção de falhas estruturais.

Usando algoritmos de gradiente, a competição Air Cargo Challenge foi estudada usando dois métodos: otimização de pontuação individual e otimização de pontuação global. Mostra-se que a carga carregada é de extrema importância, juntamente com a escolha da trajetória e as condições de equilíbrio da aeronave durante o voo. Adicionalmente, a geometria ótima da aeronave é deduzida.

O método de interpolação b-spline para a otimização de trajetória revelou-se promissora com uma diminuição no tempo computacional de 43%, obtendo, também, uma melhor resposta por parte do otimizador. Os modelos propulsivos mostraram a importância de representar com precisão o comportamento de um sistema.

Palavras-chave: Otimização de trajetória, Projeto aeroestrutural, Otimização multidisciplinar, Eficiência de otimização, Air Cargo Challenge

Abstract

In this work, a coupled aerostructural aircraft design and trajectory optimization framework is developed for the Air Cargo Challenge 2022 competition to ultimately achieve the optimal conceptual design decisions. It is based on the *OpenAeroStruct* framework, a low-fidelity aero-structural optimizer that uses the vortex-lattice method for the aerodynamic solver and a 1D truss, beam and torsional finite element for the structural solver. Additional capabilities were developed, namely a trajectory optimization module using a collocation method, with the option of using b-spline interpolation methods to increase optimizer efficiency. Two different propulsive models were also added to accurately determine the aircraft propulsive response to control input. The framework controls both aircraft geometry (wing planform and tail sizing) as well as the trajectory control (throttle and stabilizer incidence) and state variables, while successfully preventing structural failure.

Using gradient-based algorithms, the Air Cargo Challenge competition was studied using two methods: single score optimization and global score optimization. Optimal conceptual tendencies were observed and analysed. Single optimization revealed individual parts (climb, distance and payload) optimal results. Global optimization showed that cargo carried is of the utmost importance along with the trajectory choice and the trimmed conditions of the aircraft in each flight segment. Furthermore, wing and tail surface area relation was deduced along with optimal wing planform surface area.

Trajectory optimization b-spline interpolation efficiency method revealed promising with a decrease in computational time of 43% and a better optimizer response overall. The propulsive models showed the importance of accurately representing a system's behaviour.

x

Contents

List of Tables

List of Figures

Nomenclature

Greek symbols

α Angle of attack.

β Rhombus box angle.

γ Climb/descent angle.

δ_{stab} Stabilator incidence angle.

δ_t Throttle.

$\zeta_x, \zeta_y, \zeta_{fx}, \zeta_{fz}$ Defects for the longitudinal displacements and forces.

θ_t Tail twist angle.

θ_w Wing twist angle.

Λ_t Tail sweep angle.

Λ_w Wing sweep angle.

μ Molecular viscosity coefficient.

μ_{track} Track's friction coefficient.

ρ Density.

σ_y Yield stress.

τ_w Wing dihedral angle.

τ_t Tail dihedral angle.

ϕ Bank angle.

Roman symbols

b_w Wing span.

b_t Tail span.

C Capacity.

C_D Coefficient of drag.

C_{D_w} Wing coefficient of drag.

C_{D_t} Tail coefficient of drag.

$C_{D_{to}}$ Take-off coefficient of drag.

C_L Coefficient of lift.

C_{L_w} Wing coefficient of lift.

C_{L_t} Tail coefficient of lift.

$C_{L_{to}}$ Take-off coefficient of lift.

$C_{L_{max}}$ Maximum coefficient of lift.

C_M Coefficient of moment.

C_{l_w} Wing 2D coefficient of lift.

C_{l_t} Tail 2D coefficient of lift.

C_m 2D Coefficient of moment.

CG Center of gravity.

CG_p Payload center of gravity.

CG_{empty} Empty center of gravity.

c_w Wing chord.

c_t Tail chord.

D Drag.

e Specific energy.

E Young modulus.

E_{max} Maximum energy.

G Shear modulus.

h CG position.

h_n Neutral CG position.

h_{tip} Tail available space at tip chord.

h_{vs} Vertical space available at tip chord.

k Propulsive system loss energy factor.

KS Kreisselmeier–Steinhauser failure function.

L Lift.

l_{ds} Lateral diagonal available space.

l_{fit} Tail diagonal available space.

l_t Tail-wing distance.

T Thrust.

t/c Thickness-chord ratio.

t_{spar} Spar thickness.

t_{skin} Skin thickness.

t_{tube} Tube thickness.

$t_{intersect}$ Tube intersection.

$t_{elapsed}$ Elapsed flight time.

ue Usable energy factor.

V_{VT} Tail volume coefficient.

v Air speed velocity.

W Aircraft weight.

W_0 Empty weight.

W_b Battery weight.

W_p Payload weight.

Subscripts

∞ Free-stream condition.

i Computational index.

x, z Cartesian components.

$\dot{x}, \dot{z}$ Cartesian velocity components.

Glossary

ACC   Air Cargo Challenge is a university student's competition where the objective is to design the most efficient and optimized RC controlled UAV with several constraints and mission goals.

CFD   Computational Fluid Dynamics is a branch of fluid mechanics that uses numerical methods and algorithms to solve problems that involve fluid flows.

CSM   Computational Structural Mechanics is a branch of structure mechanics that uses numerical methods and algorithms to perform the analysis of structures and its components.

ESC   Electronic Speed Controller is the propulsive system component responsible for adjusting the power transferred from the battery to the motor.

FEM   Finite Element Method is a structural numerical method used to solve partial differential equations by subdividing large systems into smaller, simpler parts called finite elements.

LLT   Lifting Line Theory is a computational fluid dynamics numerical method to calculate the lift and drag distributions of a lifting surface where the influences of thickness and viscosity is neglected.

MDAO   Multidisciplinary Design Analysis and Optimization is a method to analyse and simultaneously optimize several coupled disciplines in order to achieve an optimal solution in regards to every field applied.

MDF   Multidisciplinary Feasible is an optimization architecture developed to solve optimization problems involving different disciplines.

MDO   Multi-Disciplinar Optimization is an engineering technique that uses optimization methods to solve design problems incorporating two or more disciplines.

UAV   Unmanned Air Vehicle is an aircraft piloted by remote control or on board computers.

VLM   Vortex-lattice method is a mathematical model that predicts lift distribution over a three-dimensional wing based on its geometry.

XDSM   Extended Design Structure Matrix is a diagram method to describe MDF formulated problems.

Chapter 1

Introduction

1.1 Motivation

Nature is the ultimate path for the optimal life and through its existence it always tried to improve and adapt to every scenario, being alive for millions of years. Humans, being part of Nature, are no different. We always thrived to achieve the best solution for every problem, being it agriculture, travelling, hunting or every other field as a way to simplify and adapt our lives to build a better and stronger society.

Engineering is the source of most problem solutions nowadays, specially on aircraft design, where rigorous and complex systems are involved. Aircraft design is the search for the best solution for any air vehicle problem, which, in its foundation, is an optimization problem with hundreds of design variables and highly complex systems. It makes a lot of sense to study and optimize some areas of this vast engineering subject that ultimately provides better assets for future designs.

Three major subjects of optimization study are aerodynamics, structures and trajectory, which have many ramifications of their own. The aerodynamics field allows for the study of the best geometry in every component that is subjected to the air flow and in contact with it. This field allows for the optimization of primarily drag and lift while guaranteeing stability of the whole aircraft. Structures subject is the search for the lightest reliable structure possible, being its optimization highly focused on mass reduction and highly constrained by manufacture processes. Finally, trajectory optimization searches for the best trajectory possible for the mission at hand which usually (not done in this work) tends to fuel burn minimization.

It is apparent that any of these three subjects is a vast field of research and alone can bring extraordinary improvements in aircraft design. However, more interesting than using these fields alone is coupling them into one global aircraft design optimization in which the final solution is better than any of the three alone. This introduces MDAO (Multi-disciplinary Design Analysis and Optimization) which is a growing topic in engineering in recent years.

Being able to use all three fields and apply them together into the search of the optimal solution is the Nature's way of finding and selecting the best species in every aspect of survival. MDAO in aircraft design has the possibility to revolutionize the aircraft design methodology.

1.2   Topic Overview

In this work, three major fields in aircraft design are studied and applied into one final solution through optimization: Design (Aerodynamics and Structures), Trajectory and MDAO. This section presents a brief overview of these fields and the recent paths each has taken towards the future.

1.2.1   Aircraft Design

Aircraft design, as a discipline of finding air vehicle solutions, started long ago with several failure designs (da Vinci's omithoper for example) but it only successfully found its attention boost with the Wright bothers after their first successful flight in 1903 where the first "strut-and-wire biplanes" created an "era that covers the general period from 1903 to 1930" [1]. Since that very first proof that heavier-than-air vehicles were possible, aircraft's designs have been growing exponentially with time, being more and more designs being tested and experimented every year.

This subject consists of finding a reliable solution to an air vehicle problem, where all areas of design must be accounted for (structures, control, aerodynamics, etc.). Historically, the design is done by multiple teams, where each team has the responsibility to study and create a solution in a specific field that respects the constrains given by the problem itself and the other team's needs. The final result is a hierarchy design solution constructed by every team's solution individually, which is not the best solution in a multi-disciplinary field as the one studied in this work.

In this work the fields of aerodynamics and structures are used and analysed in a coupled manner. Aero-Structural design optimizations tend to find the most efficient wing but also the most structurally reliable as well. Many articles [2–5] have studied this path of aircraft design and concluded that the strong coupling from both disciplines prove useful the usage of aerostructural design analysis tools. The reason these coupled optimizations are very useful is because they simultaneously optimize both fields for specific objectives that would be very difficult to achieve using sequential optimizations. Optimizing the aerodynamics of a wing and then its structure is not the same as optimizing both simultaneously. Figure 1.1 shows the difference in both designs in a Lift distribution optimization.
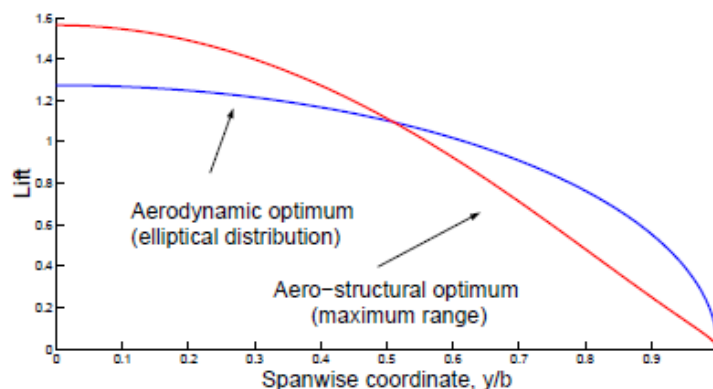
Figure 1.1: Difference between aerodynamic and aerostructural optimum lift distribution [4].

Methodologies on design take many forms but typically an aircraft design follows three usual phases

[6]: Conceptual Design, Preliminary Design and Detail Design. The first gives an overview of the aircraft to be designed based on the overall specifications and constrains needed, giving "the overall shape, size, weight and performance" [6]. So, the conceptual design lays the draft of what the aircraft should look like, being generally supported by low fidelity analysis and studies. Then, preliminary design entails the further investigation of the design and a higher fidelity study approach where the geometry, structure and control aspects of the aircraft begin to be more formally defined. "At the end of the preliminary design phase the airplane configuration is frozen and precisely defined" [6]. Finally the Detail Design phase concludes the aircraft by defining the connection elements between structures and every other small detail left for the construction of the vehicle. Also, notice that, following Raymer [6] statements, "if major changes were demanded during the preliminary phase, the conceptual design process would have been seriously flawed to begin with". Thus, this work's purpose is to search for the optimal overall characteristics for the ACC 2022 best aircraft - conceptual design - and ultimately find the optimal starting point for the aircraft's preliminary and detail design configurations.

1.2.2 Trajectory Optimization

Trajectory optimization studies the aircraft's flight pattern and mission profile as a way to find the best trajectory possible for the aircraft that increases the overall performance based on the metrics chosen for the problem. Typically, aircraft trajectory optimizations are conducted to minimize fuel consumptions but it can also be used to, in vigilance missions, to improve data collection [7] and search efficiency [8], or to improve long endurance missions [9].

There are two major trajectory optimizations methods, indirect and direct. Both work with numerical integration methods differing in the way these are executed (more details in Sec. 2.5). This work focus around the direct collocation method which is an implicit direct trajectory optimization based methodology.

Several approaches to aircraft trajectory analysis and optimization are multi-point based, meaning the trajectory is divided into several different flight segments and each segment is analysed individually. Such examples of this approach can be seen in the works of Liem et al. [10], where several flight conditions are considered to achieve a more robust design. However, although this approach optimizes for different flight segment conditions (trajectory) of the aircraft it does not consider the behaviour of the segments as a whole, which is the ultimate purpose of this work. Figure 1.2 shows the typical different flight segments of an aircraft flight profile: take-off, climb, cruise, loiter, descent and landing. This work will focus on a single multi-segment trajectory optimization considering the take-off, climb and cruise segments while respecting the flight's continuity. A simplified trajectory optimization scheme methodology as used in this work is presented in fig 1.3.

1.2.3 Multidisciplinary Design Optimization

Multidisciplinary Design Optimization (MDO) is a design optimization approach that couples different disciplines in the finding of the best solution for a given objective. OpenMDAO [12] is one framework
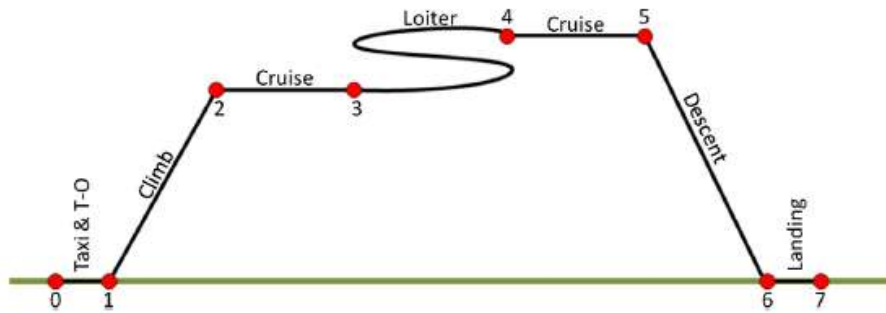
Figure 1.2: Typical aircraft misson profile [11].

Figure 1.3: Simplified diagram of the trajecory optimization scheme used in this thesis.

that tackles this problem. The current work uses as basis the OpenMDAO scheme that allows for both multidisciplinary design analysis and optimization.

The multidisciplinary analysis (MDA) scheme allows different types of processes - sequential or parallel - that involves every discipline implemented and converges to a solution that satisfies simultaneously every discipline.

The MDO framework component changes design variables and respects constraints in order to achieve, through iterations of MDA, the optimal solution for the problem, using either gradient and non-gradient methods.

Several works have been conducted with MDO approaches in the aircraft field. A good example is [13], where a morphing wing is analysed in a multidisciplinary manner to investigate its benefits; or [14] that searches for a tow-steered composite wing structure optimization.

Additionally, these types of frameworks can be used with either low fidelity - [15] - or high fidelity - [14] - computational methods, proving its wide range of applicability and usage. This thesis, as a conceptual design approach, will use low-fidelity methods that are described in Chap. 2.

1.3 Air Cargo Challenge 2022

The Air Cargo Challenge (ACC) is a student's competition where the objective lays in the development of a radio controlled (RC) airplane with several design constrains and different mission goals.

Since the very first occurrence of this competition, founded in 2003 at Instituto Superior Técnico, the goal was highly linked to the payload carried by the aircraft. Early competitions where scored based mostly on the payload carried by the aircraft, being the trajectory evaluation almost non-existing.

4

Throughout the years, the competition has been evolving to a more general purpose mission where both payload and trajectory take an important place in the score's formula. For the 2022 edition the mission purpose is to carry as many blood bags as possible as further as possible [16]. The ACC 2022 focuses on three distinct trajectory phases - take-off, climb and cruise, all of which are accounted for with the same weight in the final score.

Aircraft's in this event must follow a set of regulations that change each year's edition but typically consist of small fixed wing aircraft with 2 to 5m wing span, depending on the regulations. A typical ACC aircraft can be seen in Figure 1.4 where the aircraft designed by the team of Instituto Superior Técnico (Olissipo Air Team) for the ACC 2019 edition is shown.

Figure 1.4: Olissipo Air Team's aircraft for the ACC 2019 competition.

Typically the aircraft is limited in its size by a geometric restriction, batteries used and the propulsion system. As a way to normalize and create a fair competition, this event has always one major restriction - the electrical motor and propeller used are the same for all teams, which limits the maximum thrust. This way, the design and construction main purpose is to optimize all the mission goals' requirements without changing the propulsion system. For the ACC 2022, this involves maximizing lift for take-off and speed for cruise while actively reducing the overall weight of the aircraft. Knowing this, it is obvious to assume that an aero-structural optimization is a must if one's purpose it to achieve the best possible solution. However, since the cruise and climb are involved as part of the score's evaluation, the trajectory chosen for the aircraft plays an important role that should not be ignored. For this reason, a trajectory coupled and aero-structural optimization is a must for the pursue of the optimal solution. This pursuit is the purpose of this thesis.

1.4 Objectives and Deliverables

This work has two main purposes - create a useful framework to be used in ACC competitions (more specifically ACC 2022) and contribute to the development of trajectory coupled MDAO efficiency and results improvements.

As mentioned, this thesis uses an OpenMDAO based aerostructural framework following the work of [15] where both propulsion and trajectory models are implemented. Additionally, several design variables, constraints and performance metrics are added to the system to more rigorously represent the problem at hand.

The objectives of this work include:

- Develop and implement a propulsion model representative of the usual electrical motors used in ACC competitions;

- Develop an efficient trajectory optimization based method that allows for reliable solutions at low computational cost;

- Define adequate conditions and metrics to define the ACC 2022 competition aircraft, its constraints and its behaviour;

- Perform coupled aircraft design and trajectory optimization to achieve an improved conceptual design and compare with the already designed aircraft by team Olissipo Air Team;

- Understand the competition's scoring scheme by comparing single score (distance, height or payload) with global score optimizations;

The contribution of this work will be the trajectory efficiency improvement analysis study and all the code developed that consists of the ACC framework created, which will allow for a growth in design efficiency for future ACC competitions. The major deliverable is the developed coupled aero-structural design and trajectory optimization framework that can be used in future ACC competitions by allowing simple performance metrics, variables or constraints to be added and implemented.

1.5 Thesis Outline

Chapter 2 introduces the theoretical overview used to explore the four five subjects used along this thesis - MDO, aerodynamics, structures, propulsion and trajectory.

The models used to create the developed framework are explored in Chap. 3. It describes the efficient trajectory optimization model implemented, two different propulsive model implementations considering constant power and battery decay, and all the competition related models incorporated.

In Chap. 4, the framework developed is detailed and its functioning is broken down. Additionally, a framework verification is conducted where a mesh study is conducted and the framework's results are analysed.

The final results are presented in Chap. 5. It starts with the problem formulation and then each single score segment is evaluated and a global optimization study is conducted. Additionally, both the efficient trajectory optimization model implemented and the propulsive system model possibilities results are explored.

Lastly, the work's achievements are summarized in Chap. 6, where suggestions for future developments are presented.

Chapter 2

Theoretical Overview

This chapter contains an overview of the different disciplines used in this work. It intends to briefly explore and explain the theory behind the created framework.

It is divided in five sections, each refering to a specific discipline: Multidisciplinary Optimization explains the concepts and more specifically the models used in this work; Computational Fluid Dynamics introduces the aerodynamic computational models used; Computational Structural Mechanics explores the *OpenAeroStruct*'s wingbox structural computational model; Electric Propulsive System briefly described the general electrical system used in the aircraft covered by this work; and Trajectory Optimization Methods intends to explore the different possible methods and explain further the model approached in this work.

2.1 Multidisciplinary Optimization

As described in [17] Multidisciplinary Optimization, or MDO, can be described as a collection of mathematical techniques for multi-variable optimization in which the optimization clearly crosses disciplinary boundaries simultaneously. A common example in aircraft design is the coupled aerodynamic and structural optimization. Such example can be found in the works of Abdelkader Benaouali [18] or Giulio Molinari [19] where the strong coupling between structural and aerodynamic performance of the wing is used in favour of an MDO optimization scheme.

An MDO problem can be posed as a standard non-linear programming problem where one must find the set of design variables that optimize a given objective subjected to certain constraints [20]. The complexity of this method results from the discipline analyses and their coupling management. An MDO formulation not only depends on the design variables but also on the analysis of the different disciplines of the problem, meaning the discipline analysis is interdependent - one analysis requires as input the output of other analysis. MDO are a formal setting for managing this interdependence in the design process [21].

Using the same terminology as [20], MDO can be built with different types of "architectures" - Monolithic and Distributed. Monolithic architectures cast its problems as a single optimization problem, while

Distributed decompose the optimization problem into hierarchical optimization sub-problems.

For this thesis, a Multidisciplinary Feasible (MDF) monolithic architecture is used which has the advantages of being, when compared to other monolithic architectures, the smallest optimization problem, where only the design variables, objective function and constraints are controlled directly by the optimizer [20].

Figure 2.1 depicts an MDF architecture example approach for three disciplines in the form of an extended design structure matrix (XDSM) diagram [22]. This architecture is defined in this example with steps from 0 to 7 and three typical groups: Optimization, MDA and Functions. Step 0 starts the optimization with the set of design variables $x^{(0)}$ that flow into the MDA (steps 1 to 5) segment together with the coupling variables $y^{(0)}$. In this step each analysis group produces a new set of coupling variables that is introduced iteratively into the next analysis group. Note that horizontal lines in this scheme present outputs and vertical lines represent inputs. After a full MDA iteration the new set of coupling variables y_i are used for the next MDA iteration until a certain convergence criteria is met in the process. With the MDA converged, the variables x and y are used to calculate the objective and constraint functions (step 6). These are introduced into the optimizer group (step 7). Here the set of variables x are changed according to the algorithm used and a new cycle of the optimizer begins. If the optimizer's stopping criteria is met, the set of optimal variables x^* and y^* are defined.
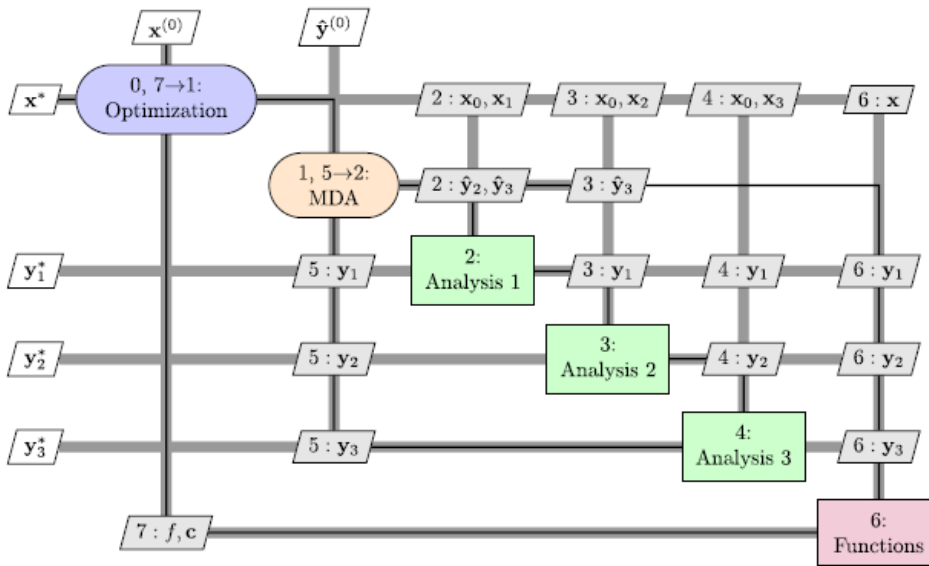
Figure 2.1: MDF architecture diagram with a Gauss-Seidel multidisciplinary analysis [20].

Typically a Gauss-Seidel fixed point iteration (as presented in Fig. 2.2) or a Newton-based method [23] is used to converge the MDA segment. As explained before, this process uses a full MDA convergence in each optimization iteration step, producing a set of converged coupling variables that together with the design variables deduce the objective and constraint functions values. This process ensures that each optimization iteration is "multidisciplinary feasible" since each iteration point guarantees the feasibility of the iteration's solution achieved. This detail ensures that, even if the optimizer ends prematurely, the solution achieved is a physically realizable design point [24]. However, this does not mean the

solution respects its constraint functions [20].
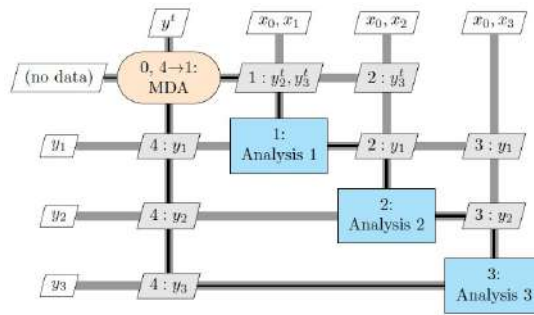
Figure 2.2: Gauss-Seidel fixed point iteration method schematic [25].

2.2 Computational Fluid Dynamics

Aerodynamics studies the body-fluid interactions and their products. In aircraft design this usually translates to the determination of lift and drag of every component of the aircraft.

For an aerodynamic analysis, one can choose between high or low fidelity methods. Both have their advantageous and disadvantages: high fidelity methods usually tend to produce results that predict the physical interactions more accurately but are highly dependable on computational resources; and low fidelity methods are more computationally efficient but produce less accurate solutions. A trade-off must always be sought and the method to be chosen depends on the problem presented. Taking as example the work of Mohammad Zadeh and Sayadi [26], an efficient multi-fidelity modelled is built to reduce computational costs, where both high fidelity models and low fidelity models are combined with meta-models as a way to reliably improve efficiency. Another example are surrogate based models [27] that approximate a high-fidelity result data into fitting functions to create a more efficient design space search.

In optimization frameworks and when considering many fields of study and analysis simultaneously it is advantageous to use low fidelity and highly efficient methods since these usual involve several iterations and analyses to search for the optimum solution. This reason led for the creation of OpenAeroStruct (OAS), which is highly efficient using the low fidelity Vortex Latice Method (VLM). This method is further explored next.

2.2.1 Vortex-Lattice Method (VLM)

The Vortex-Lattice Method (VLM) used is based on Anderson 1991 [28] that combines multiple modern numerical lifting-line theory (LLT) models, as described by Philips ans Snyder (2000) [29]. However, the VLM method is more general than the LLT models since it can model low aspect ratio wings, swept wings and delta wings [30].

This method models the wing as a combination of horseshoe vortices. Each horseshoe vortex, as illustrated in Fig. 2.3, consists of a "a bound vortex in the spanwise direction and two trailing vortices that

extend into the freestream direction" [30], which look similar to a typical horseshoe. Each vortex filament of the horseshoe induces a flow field around its surrounding space. Each filament has its strength and circulation, producing the Lift on the surface.
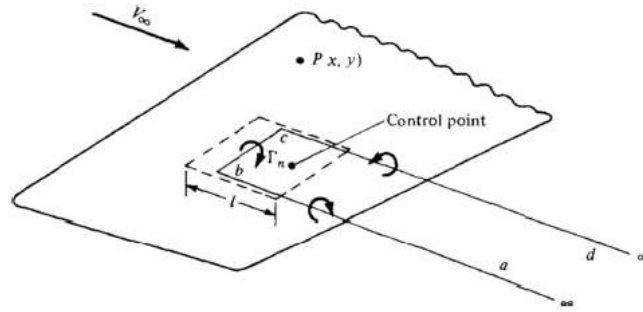
Figure 2.3: Example of a horseshoe vortex in a generic location of a wing surface [30].

The Biot–Savart [30] law relates the velocity of the flow field at an arbitrary point P caused by a segment dl of a vortex filament with circulation strength Γ via

$$dV = \frac{\Gamma}{4\pi} \frac{\vec{dl} \times \vec{r}}{|\vec{r}|^3} \quad ,$$

(2.1)

which, integrating over a semi-infinite straight vortex filament, leads to

$$V = \frac{\Gamma}{4\pi h} = a\Gamma \quad ,$$

(2.2)

where h is the distance from point P to the finite start point of the vortex filament and a the aerodynamic influence coefficient of the considered horseshoe panel to point P.

The VLM method will consist of spanwise and chordwise horseshoe panels that, by imposing flow tangency conditions in each panel, result in a linear system of equations of the form

$$[A][\Gamma] = \{\vec{V_\infty} \cdot \vec{n}\} \quad ,$$

(2.3)

where $[A]$ is the aerodynamic influence coefficient matrix formed by the aerodynamic influence coefficients of all horseshoe panels to every control point of the modelled wing; and $\vec{n}$ is the normal to the panel.

By solving this linear system of equations, the circulation of each panel is determined which in turn can be used to calculate the force acting in each panel as

$$\vec{F_i} = \rho \Gamma_i (\vec{V_\infty} + \vec{v_i}) \times \vec{l_i},$$

(2.4)

where $\vec{v_i}$ is the induced velocity at the center of the bound vortex, and $\vec{l_i}$ is the bound vortex vector.

Lift and drag result from the panel forces decomposed into the normal and streamwise directions. Additionally, to improve the drag estimation model, a skin friction drag is calculated using flat-plate-based estimates (Raymer [6], sec. 12.5.3) [30].

2.3   Computational Structural Mechanics

Structures is the field where material mechanical behaviour is studied. The purpose of this engineering area is to provide mechanically reliable solutions to the problems at hand. Such problems can be spar sizing, wing skin compression strength, composite structure layup and many others. In this thesis, a structural failure analysis is used to size the wing's spar, ultimately reduce its mass while prevent it from failing under operating loads.

Similar to the aerodynamics field, structural analysis can use both high fidelity and low fidelity models. High fidelity analysis, while more accurate, bring additional computational requirements and slow optimization cycles. On the other hand, low fidelity models are less computationally dependent and can accelerate optimization results. As mentioned before, this work is a conceptual design optimization with the purpose of finding the optimum starting conceptual point for the competition's winning design, hence the usage of a low fidelity model for the structural integrity.

OpenAeroStruct [30] offers two types of spars to model the structural behaviour of the wing: tubular spar and wingbox. Both can be seen in the environment of the competition or similar aircrafts. Taking for example 2019's Olissipo Air Team's design (Fig. 2.4 (a)), a tubular spar is used while another 2019 team (Fig. 2.4 (b)) used a small wingbox scheme - similar to a rectangular spar. Typically, tubular systems tend to be easier to assemble, specially when using wing-connectors [31]. However, these are not the most optimized solutions when compared to the wingbox schemes, reason for its wide usage in commercial aircrafts, specially since composite wingbox schemes were introduced that heavily reduced the cost production and increased the load-bearing properties [32]. For this thesis, the wingbox model is used since it can provide lower weight solutions and it is in agreement with the Olissipo Air Team's recent structural studies and developments.

(a) Tubular spar.
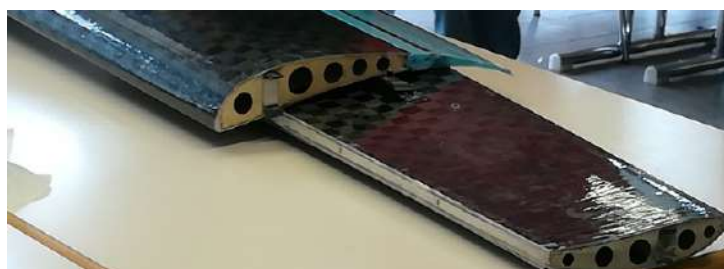
(b) Small wingbox spar.

Figure 2.4: Typical spar geometries on the ACC 2019 competition design.

2.3.1 Finite Element Method (FEM) Model

The Finite Element Method (FEM) model is a spatial beam element approach with six DOFs (degrees of freedom) per node. This element is a combination of truss, beam and torsional elements, which simultaneously carry axial, bending and torsional loads [30]. The element is presented in Fig. 2.5.
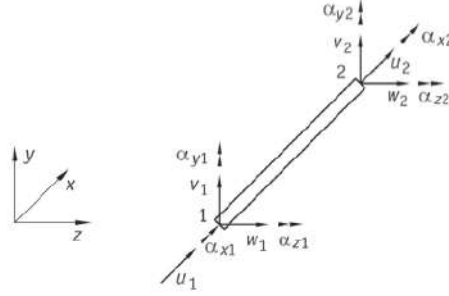
Figure 2.5: FEM element used for the structural model chosen [30].

The element comprises a 2 node system, with a total of 12 DOFs, where each node can translate in every direction (x, y and z) and can rotate in respect to all three axis (x, y and z). The local stiffness matrix is calculated for each element in the local frame as

$$K_e = \begin{bmatrix}
k_1 & 0 & 0 & 0 & 0 & 0 & -k_1 & 0 & 0 & 0 & 0 & 0 \\
0 & 12k_2^z & 0 & 0 & 0 & 6k_2^z l & 0 & -12k_2^z & 0 & 0 & 0 & 6k_2^z l \\
0 & 0 & 12k_2^y & 0 & -6k_2^y l & 0 & 0 & 0 & 12k_2^y & 0 & -6k_2^y l & 0 \\
0 & 0 & 0 & k_3 & 0 & 0 & 0 & 0 & 0 & -k_3 & 0 & 0 \\
0 & 0 & -6k_2^y l & 0 & 4k_2^y l^2 & 0 & 0 & 0 & 6k_2^y l & 0 & 2k_2^y l^2 & 0 \\
0 & 6k_2^z l & 0 & 0 & 0 & 4k_2^z l^2 & 0 & -6k_2^z l & 0 & 0 & 0 & 2k_2^z l^2 \\
-k_1 & 0 & 0 & 0 & 0 & 0 & k_1 & 0 & 0 & 0 & 0 & 0 \\
0 & -12k_2^z & 0 & 0 & 0 & -6k_2^z l & 0 & 12k_2^z & 0 & 0 & 0 & -6k_2^z l \\
0 & 0 & -12k_2^y & 0 & 6k_2^y l & 0 & 0 & 0 & -12k_2^y & 0 & 6k_2^y l & 0 \\
0 & 0 & 0 & -k_3 & 0 & 0 & 0 & 0 & 0 & k_3 & 0 & 0 \\
0 & 0 & -6k_2^y l & 0 & 2k_2^y l^2 & 0 & 0 & 0 & 6k_2^y l & 0 & 4k_2^y l^2 & 0 \\
0 & 6k_2^z l & 0 & 0 & 0 & 2k_2^z l^2 & 0 & -6k_2^z l & 0 & 0 & 0 & 4k_2^z l^2
\end{bmatrix} \quad, \tag{2.5}$$

where $k_1 = \frac{EA}{L}$, $k_2^z = \frac{EI_z}{L^3}$, $k_2^y = \frac{EI_y}{L^3}$, $k_3 = \frac{GJ}{L}$, and E is the Young's modulus, A is the element cross-sectional area, L is the element length, G is the shear modulus, J is the polar moment of inertia, and the I's are the second moments of area about the three local coordinate directions [30].

Afterwards, the global stiffness matrix is assembled using transformed local stiffness matrices by applying transformation matrices to each local element to transform from local to global coordinates.

Finally, the linear system of equations to be solved is

$$[K]\vec{u} = \vec{F} \quad, \tag{2.6}$$

where $[K]$ is the global stiffness matrix, $\vec{u}$ the displacement vector and $\vec{F}$ the forces. The forces result from the aerodynamic model, calculated for each wing section and applied to every structural element node (more details in Chap. 4).

From this linear system of equations, the nodes displacements are determined and these will be used for MDA convergence and stress analysis. The latter will be further discussed next.

2.3.2 WingBox Model

As seen, the FEM model used does not consider the spar geometry explicitly, it is based only on its sectional properties. Hence, any geometric system can be modelled into this FEM model as long as all properties needed for the well functioning of the model can be determined.

Following Chauhan and Martins [33] notes on how the wingbox system was developed and implemented, this comprises two topics: properties calculation and stress determination. A typical wingbox section can be vizualized in Fig. 2.6.
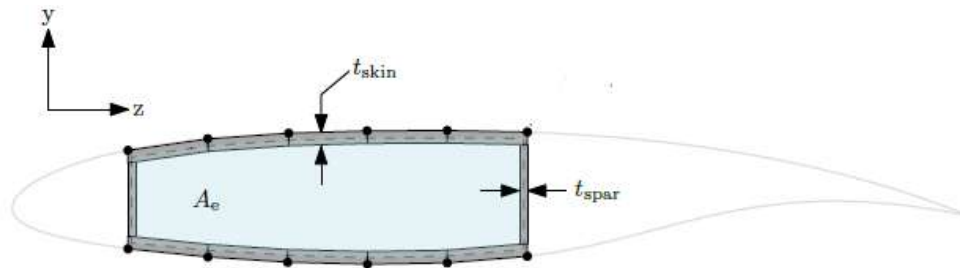
Figure 2.6: Typical wingbox section geometry scheme [33].

For the wingbox structural properties, the section is divided in several parallelograms (using the airfoil coordinates starting to end points) by using thickness values and extruding along the local chordwise y-axis. These are used to calculate the various area and moment of inertia contributions, which summed up determine the total aforementioned properties.

The torsional constant is calculated as explained in the book of Megson [34], where a closed section with small wall thickness and uniform shear flow is considered.

Finally the last properties needed are the elastic modulus of the material - E and G - that are granted by the material properties used for the problem (more details in Subsec. 5.1.2).

For the stress calculations, this model uses, the Kreisselmeier–Steinhauser (KS) function [35] which allows for several stress inputs to be analysed in a single constraint manner. Stresses are calculated at four distinct points in the wingbox with particular stress combinations as illustrated in Fig. 2.7. These 4 points are used to simplify the problem and to only consider the worst case scenarios, resulting in a "conservative estimate of the maximum Von Mises stress" [33].

With this model, the displacement and stress calculations can be determined for any applied nodal loads, which will then be implemented in the MDA analysis for convergence and in the optimization cycle for failure constraint determination.

2.4 Electric Propulsive System

Electric Propulsive System refers to the propulsive system of the aircraft, responsible for generating thrust. Usually a propulsion system involves a propulsive engager (thermal engine or electric motor) and a propulsive actuator (fan blades or propellers). Also, there must be an energy source - either from combustion (fossil fuel) or electrical storage. Figure 2.8 schematically describes in a simple manner any
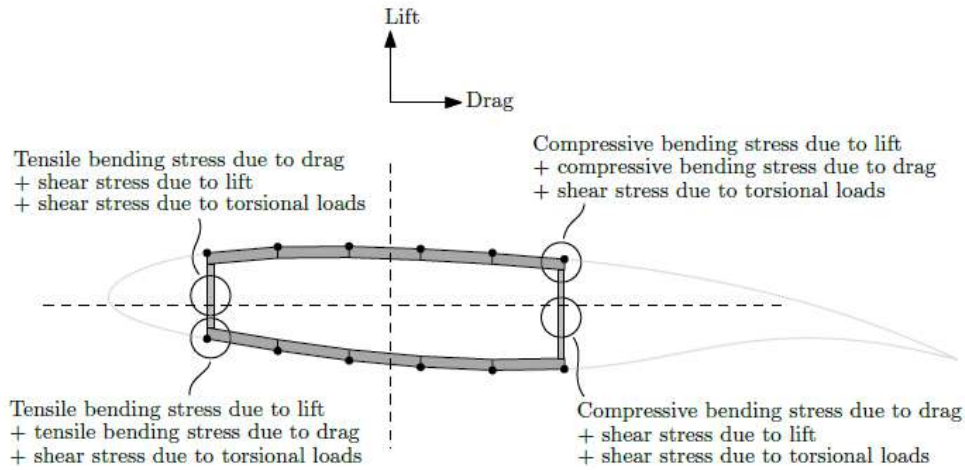
Figure 2.7: Wingbox stress analysis critical points considered [33].

propulsion system composition.
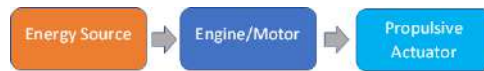
Figure 2.8: Simplified propulsive system diagram.

To better understand the typical electrical propulsion system used in the environment of this work's purpose, one must first consider separately the motor (energy transformation) and the propeller (output thrust). Additionally, another component must be considered in this system - the electronic speed controller (ESC) - which is responsible for adjusting the power transferred from the battery to the motor.

Starting with the input energy transferred into the motor and its rotational speed response, first a type of electrical storage must be considered. Following the ACC 2022 rules [16], the batteries allowed are LiPo, LiIo or LiFePo, which are Lithium based batteries. Several works have been conducted to study the discharge functions of these batteries, such as [36], that suggests a way to calculate a constant power Lithium battery discharge curve based on more known constant electrical discharge curves. These discharge curves describe the voltage output of a battery through time while discharging. Figure 2.9 presents a typical discharge curve.

As it can be observed, the voltage tends to rapidly decrease in the first moments and stabilize in an almost constant value until finally there is a quick drop to zero in the last few moments. The voltage plateau achieved is highly dependent on the battery's discharge rate, being lower the higher the discharge rate is.

The battery flows its energy into the ESC which will control the power input to the motor by means of a radio control signal sent by an operator. For this work, the ESC could be modelled as a power loss factor and an explanation for the variable input thrust of the aircraft and its associated power consumption.

Finally, the electrical motor is a tool that converts electrical power to mechanical power. Electrical motors can be brushed or brushless, difference lays in their mechanism. In a brushed motor, the wire coils form an armature that acts as an electromagnet. It is fed electric current, whose direction is reversed
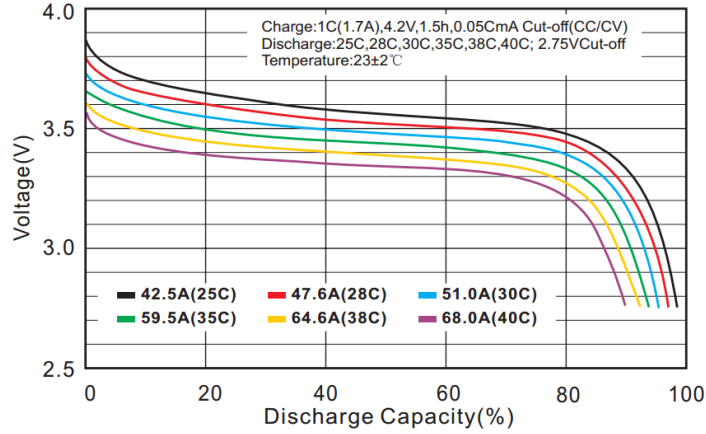
Figure 2.9: Lipo batteries discharge curves based on discharge rate [37].

through a mechanical commutator. With the change of current's direction, the polarity of the armature's electromagnet also changes and because there is a stationary magnet around it, the armature rotates. In brushless motors, the rotor is the permanent magnet and the coils are static. Commutation is done electronically, which is more precise than with mechanical brushes [38].

In a study conducted by Junid et al. [39], "if efficiency, range and high speed at varying loads and throttle are top priority, a brushless ESC system, preferably fanned, is recommended", which makes it preferable to use brushless motors instead of brushed ones. Additionally, previously mentioned work from Bronz et al. [40] states that brushless motors "have numerous advantages such as having a higher efficiency than brushed motors, longer lifetime, generating less noise, having higher power to weight ratio", which make them "more reliable for the UAV applications." Competition regulation [16] also states that only one motor can be used - the AXI 2826/10 GOLD LINE V2 - which is a brushless motor. For the propulsion system, the motor could be simply modelled as a transformation tool from input power (electrical) to output power (mechanical) with a loss fraction associated.

On the output thrust segment, a propeller is used and studied. Several works have been conducted in this field such as [41] where a thrust model is developed based on momentum theory, blade-element theory and vortex theory, which all combined proved good approximations to the experimental data.

Since this thesis underlays a conceptual design optimization, an easy and simple model should be explored and implemented. Following what was done in [15] or [42] a momentum theory approach could be modelled and implemented.

Momentum theory was first developped by Rankine and R.E Froude [41] and is based on a consideration of the momentum and kinetic energy imparted to the mass of air flowing through the propeller [43]. This theory ultimately results in the power supplied to the propeller disk,

$$P_{disk} = TV_\infty + \frac{k}{2}T(-V_\infty + \sqrt{V_\infty^2 + \frac{2T}{\rho A disk}}) \quad , \tag{2.7}$$

where T is the thrust, V_∞ is the freestream velocity, ρ is the air density and A_{disk} is the disk area of the propeller. A detail explanation of this result can be read in McCormick [44]. Additionally, following [42], a factor k is implemented to model the induced losses of the propeller, since the momentum theory does

15

not consider the losses due to torque from propeller profile drag, blade tip and hub losses, and effect of number of blades [41]. This factor k will be further discussed in Sec 3.2.

Summarizing, the operator chooses a certain control of thrust power (δ_t) that imposes a certain power consumption of the battery and consequently a power output from the brushless motor. Afterwards the momentum theory model implemented uses this input power and calculates the thrust output of the system. Parallel to this, a calculation of energy consumption can be achieved by keeping track of the power consumed from the battery through time. It is important to note that the control thrust variable, although named as such, will control the power input to the motor, being heavily dependent on the discharge curve of the battery used.

Further study is conducted on this model to simulate its behaviour by comparing it to real scenario experiments in wind tunnel testing. This study is presented in Sec. 3.2 where all parameters of this model are tested and studied to create a reasonable model for the system and consequently provide a good propulsion model estimate for the optimization problem at hand.

2.5   Trajectory Optimization Methods

Trajectory is a wide spectrum field where many variables can be accounted for as well as many degrees of freedom for the analysis of body motion to understand its behaviour through space as a function of time. Trajectory optimization then becomes the "set of methods that are used to find the best choice of trajectory, typically by selecting the inputs to the system, known as controls, as functions of time" [45].

There are two types of variables in this optimization scheme: state and control variables. State variables can not be defined and are a result from the system's inputs. On the other hand, control variables are input variables that are used to influence and change the state variables. Both are functions of time and can have physical relations between them. For example, in the work of Chauhan and Martins [42], the purpose is to optimize the take-off trajectory of an electric VTOL (tilt-wing) aircraft, where the state variables used are the horizontal and vertical speed and displacements components and the control variables are the wing's tilt angle and the electrical power used, being the optimization goal to find the optimal set of control and state variables that lead to the lowest energy consumption.

There are many techniques for numerically solving trajectory optimization problems [46], classified as either indirect or direct methods. Betts [46] describes these methods schematically presented in Fig. 2.10.
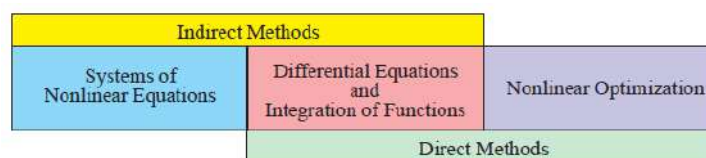
Figure 2.10: Indirect and direct trajectory optimization methods diagram [46].

Indirect methods usually require the solution of non-linear multipoint boundary value problems [46],

16

while direct methods do not require those solutions but instead use non-linear optimization. Another common way to distinguish these methods is that a direct method discretizes and then optimizes, while an indirect method optimizes and then discretizes [45].

This thesis implements a direct collocation method (or direct transcription method) which is considered powerful for solving general optimal control problems [46]. This method involves the parametrization of the trajectory into state and control variables and solving implicit or explicit numerical integration equations while respecting several constraints - the defects. The defects are the result of the dynamics of the problem. All trajectory problems have dynamic equations that describe the relations between the trajectory variables of the problem that usually involve differential equations. The defects represent the disparity metric of these differential equations and can be represented as

$$v - \dot{x} = 0 \quad , \tag{2.8}$$

where $\dot{x}$ is the derivative of x (state variable) in respect to time, and v another variable of the problem (velocity for example), where

$$\dot{x} = v, \quad \int_{t_k}^{t_{k+1}} \dot{x} dt = \int_{t_k}^{t_{k+1}} v dt \tag{2.9}$$

This formulation starts by dividing all variables defined for the trajectory, which are a function of time, in finite intervals of time and describing them in a polynomial manner of a specific degree in each interval. These intervals must guarantee the function's continuity but do not need to respect each function's derivatives continuity. In each interval, the dynamics described for the problem must be guaranteed, so a numerical integration method is used to calculate the defects value and a constraint is used to verify if the defects respect their expected null value. Next, for each "collocation point" corresponding to the beginning and end of each interval (for a linear interpolation) the state and control variables' initial values are chosen to start the trajectory optimization. The optimization can then be initialized to maximize or minimize a certain objective and the trajectory's state and control variables will be "collocated" into their optimum values while respecting every constrained added to the problem and always their defects.

In this thesis, a trapezoidal direct collocation method [47] is used where the numerical integration method used follows the trapezoidal method as

$$x_{k+1} - x_k = \frac{1}{2}(t_{k+1} - t_k)(v_{k+1} + v_k) \quad . \tag{2.10}$$

Chapter 3

Framework Models Development

This work focus on the implementation of a low-fidelity design optimization for the ACC 2022's competition. For this, the following fields of study were used: Aerodynamics, Structures, Trajectory and Propulsion. The first two result from the models described in Sec. 2.2 and Sec. 2.3 implemented in OpenAeroStruct [30] where the coupling from both disciplines is described in Chap. 4. The other two fields are further developed here.

The trajectory model, described in Sec. 3.1, introduces an improved approach to the simple direct collocation method vastly known and used by implementing b-spline function approximations to decrease computational resources while keeping result convergence and accuracy.

The propulsion model, described in Sec. 3.2, introduces a better approximation for the problem than any other simple model approach. Since the competition only allows for one specific motor and propeller, using experimental data to model the propulsion system will describe the propulsion system of the aircraft more accurately.

Finally, Sec.3.3 includes the competition's specific models, where the general aircraft and variables used are detailed.

3.1 Trajectory Model

The trajectory model implemented in this work is a direct collocation control point based method implemented with an additional use of B-spline interpolation to increase efficiency and results reliability. This section provides a brief explanation of the method and a study conducted on its efficiency improvement.

3.1.1 Model Description

Trajectory control optimization usually lays upon two different approaches: shooting and collocation methods. The first one uses an explicit integration method, while the latter uses an implicit integration method. Both methods are used in many applications and the best method depends on the application. For this reason and because of its simplicity in design and comprehensibility, the direct collocation

method was implemented in this thesis. This method was implemented using simple trapezoidal integration along with the problem's dynamics. This works by imposing the dynamic constraints of the trajectory in analysis - defects - with a differential equation solution based on trapezoidal function approximation approach (see Sec. 2.5 for more details about the system's dynamics).

Although the implicit method would work on its own, the efficiency of such method using simple trapezoidal function simplifications is poor and not reliable when the number of steps and control points increases. In an attempt to solve this problem, the implementation of B-spline curves was introduced, a curve data fitting method which is known for its inherit smoothness and continuity.

Gradient based optimization, and every optimization for that matter, are highly dependent on the number of design variables of the problem. For this trajectory optimization problem, the number of trajectory variables are inherently dependent on the number of control points chosen for the system, meaning the more control points chosen, the more accurate the solution is but also less efficient the optimization becomes. An interesting approach to solve this problem would be to relax the control points needs, thus increasing the efficiency, but maintain the accuracy of the solution. Such approach was defined using a 3rd order B-spline function approximation and the results will be discussed in this section.

The purpose of B-splines is to create a curve that fits the dynamics criteria defined by the system with less control points than the number of steps used to verify the system's dynamics. The idea is to have less control points that ultimately describe the same end solution or one that is close. Figure 3.1 shows the visual explanation of the aforementioned.
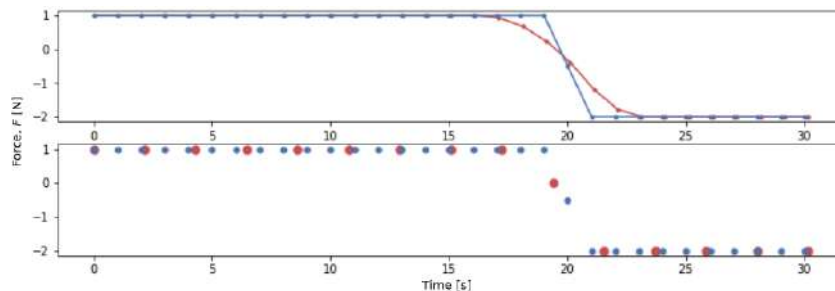
Figure 3.1: B-spline approach and control point visualization compared with unmodified direct collocation control point mechanism.

As seen, B-spline curve (red) is a smooth function approximation while the unmodified version is not derivative continuous throughout. However, this result shows similar solutions for the given function at hand. However, the number of control points is highly reduced. Notice that for the correct dynamic system evaluation, a significant number of steps must be calculated and, by using this b-spline interpolation, a good function approximation is achieved with relative ease and a low number of control points. For the example shown, the number of control points was reduced from 30 (blue dots) to 15 (red dots) which, as it will be studied later, results in a significant efficiency increase.

19

3.1.2 BangBang problem

To better understand the benefits of the suggested implementation, the *BangBang* problem was studied [48]. *BangBang* provides a simple well studied problem that allows to understand the advantageous of different approaches to trajectory optimization.

The goal of this problem's trajectory optimization is to minimize the time needed for a unit mass particle with no viscous forces applied to travel 300 meters in one direction while starting and ending in a stand still position (velocity must be null in the beginning and the end of the trajectory). Figure 3.2 presents a visualization of the problem.
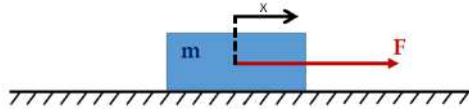
Figure 3.2: BangBang problem visualization.

Additionally, the problem is constrained by the system's dynamics,

$$\begin{cases} \dot{x} = v \\ \dot{v} = F \end{cases} \tag{3.1}$$

and by the boundary conditions

$$\begin{cases} x(t_i) = 0 \ [m], x(t_f) = 300 \ [m] \\ v(t_i) = 0 \ [m/s], v(t_f) = 300 \ [m/s] \end{cases}, \tag{3.2}$$

being x, v and F the particle's position, velocity and force for a given time, respectively. Both t_i and t_f represent the initial and final time instances.

The design variables of the problem are the n control points that carry three variables each - position, x, velocity, v, and force, F.

First, the optimal solution achieved by the unmodified trapezoidal implicit integration procedure implemented for the direct collocation method is analysed. Figure 3.3 shows the graphical results for the gradual increase of the number of control points given for the system.

Clearly, there are significant gains by including more control points into our system, especially for a low number of control points. However, after 30 the results are practically unchanged and the increase of the number of control points produces insignificant improvements, thus the ideal number of control points for this problem is 30. The dots shown throughout Fig. 3.3 show not only the control point's location, but also the limit step given for the system's dynamics verification. This last segment is quite important when understanding the mechanism of the spline implementation which, unlike this first method, does not have coincident control and step points. Instead, the control points generate a fitting curve (b-spline) which then is used to evaluate the function's value on the step's points needed for the dynamic verification of the system.

Figure 3.3: Problem's design variables values throughout time with the unmodified version of the direct collocation method used for the varying number of total control points.

3.1.3 B-spline efficiency study

The B-spline method can be implemented as a curve fitting function to every variable of the problem at hand, meaning, all three of the design variables (x, v and F) can be described as a spline. In this work, an incremental study was produced. First, the force is implemented as a spline, then the velocity and finally the position. Finally a conclusion is drawn from this approach.

Figure 3.4 presents the N2 diagrams for the conducted study. This method creates a different segment where it can be clearly seen the implementation done. For both diagrams, the $dynamics$ group is responsible for delivering the constraint and objective function values, while the $indeps$ group provides the control points of the independent variables of the problem. For the spline transformation problem (b), an additional $interp_f$ group is created that is responsible for receiving the control points given by the $indeps$ group and delivering independent variable spline approximation values for the system's dynamics. This interface allows for the difference in number of control points and dynamic verification steps.

Additionally, and referring to every N2 diagram in this thesis, this type of diagram can be read by seeing the variable input and output flow. Taking as example the trajectory variables and the $thrust$ variable b-spline module (see Fig. 3.4 (b)), the variable $thrust_value$ flows as input into the module $interp_f$ which produces the output variable $thrust$. These output variables can then be used as input variables in other modules or be used as optimization goals or constraints. As a simplification, every diagonal square indicates a presence of a module and every square outside the diagonal represents modules interaction through input-output basis.

Following aforementioned methodology and using a 30 control point method, the force b-spline approximation was studied. Figure 3.5 and Tab. 3.1 yield the results produced for the force's b-spline implementation where the unmodified model was also included for comparison.

Graphic visualization clearly shows the method and the spline implementation on the force variable applied to the unit mass system. As expected, few control nodes produced unreliable solutions, whereas
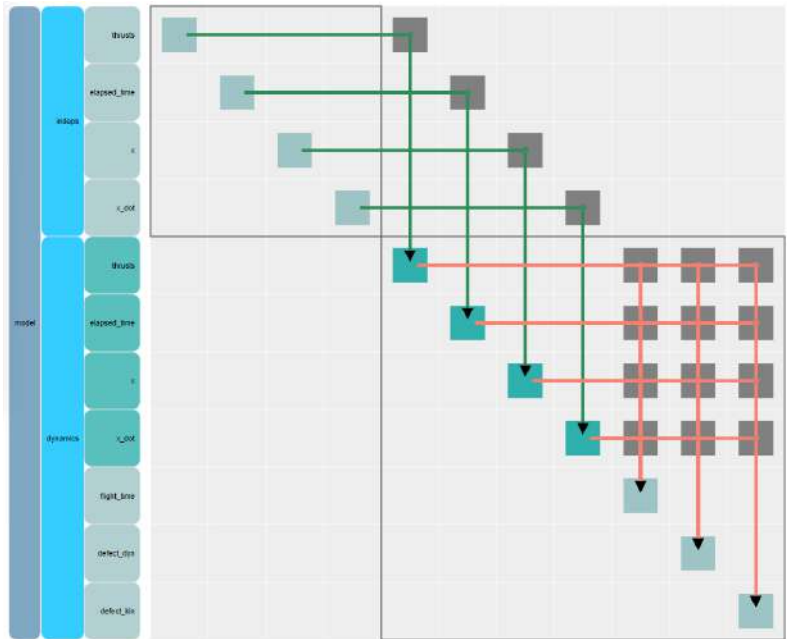
(a) Unmodified direct collocation method N2 Diagram.
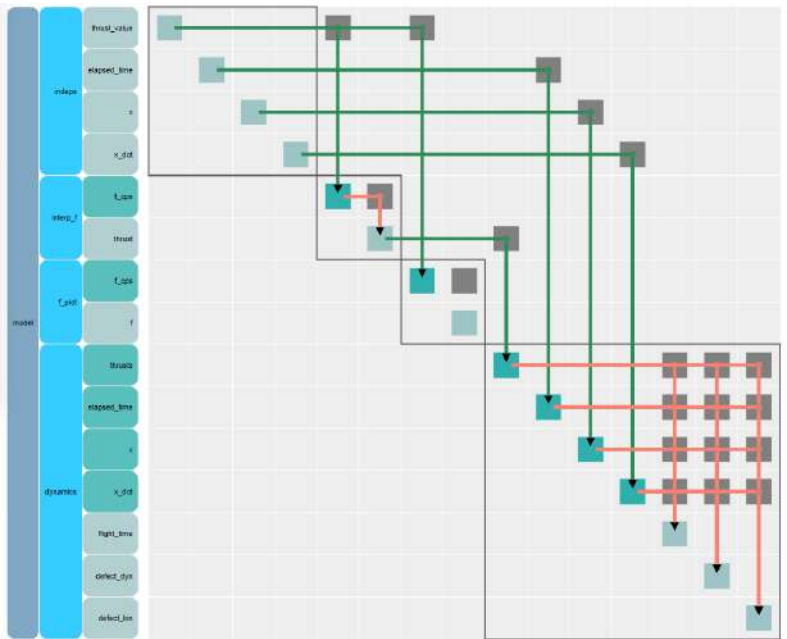
(b) B-spline direct collocation method N2 Diagram for thrust b-pline approximation.

Figure 3.4: N2 Diagrams for both unmodified and modified direct collocation methods used for the efficiency study.

more nodes produced better solutions. The importance of this method is the time reduction for the same operation when comparing the unmodified and b-spline modified version. For 12 or 16 force control points, the results were similar to the best found in the study conducted for the unmodified bangbang problem. Furthermore, this process allowed for a 80 function evaluation gain for the 12 and 16 control points. Also, using 12 or 16 force control points produces an objective function value (time of the trajectory) only 1.37% and 0.46% different from the one found previously.

To best evaluate the influence of b-spline approximation on both velocity and displacement, the
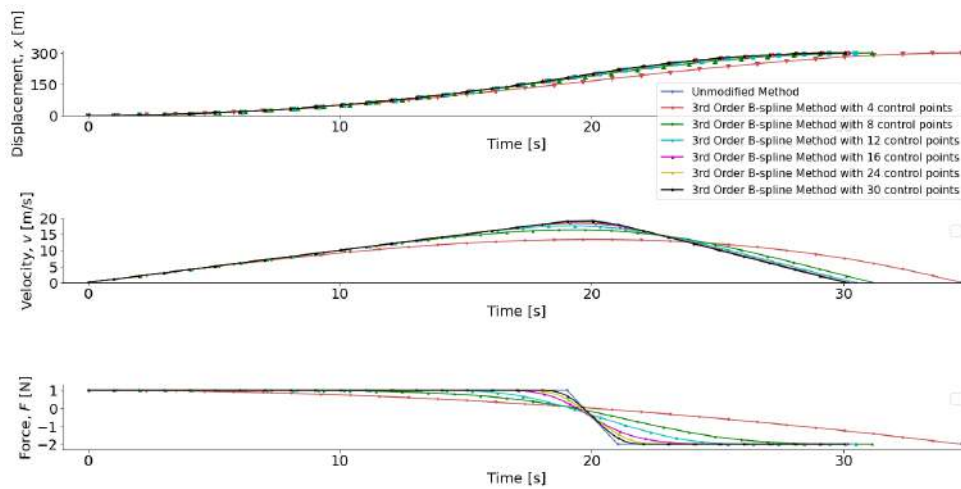
Figure 3.5: Problem's design variables values throughout time with both the modified and unmodified version of the direct collocation method used for the varying number of force spline control points.

number of force control points will be kept constant to evaluate the velocity based spline and then the number of velocity control points will also be kept constant to evaluate the position based spline. Although this does not evaluate all influences on this problem, this study is only meant to help understand the influence and needs of b-spline implementation as a reliable relaxation method to ultimately reduce the time cost of the trajectory optimization.

As before, a variable number of control points for the velocity was tested and the results are shown in Fig. 3.6 and Tab. 3.1. The number of force spline control points was kept equal to 16.
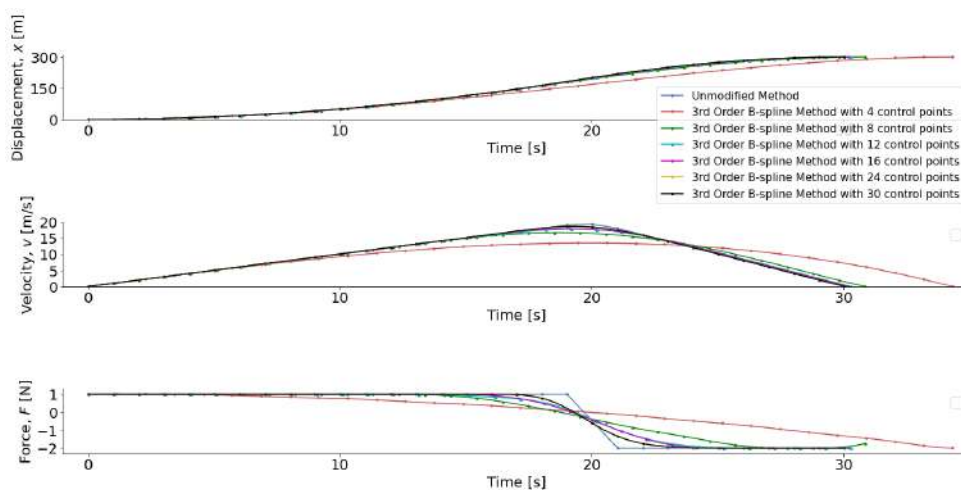
Figure 3.6: Problem's design variables values throughout time with both the modified and unmodified version of the direct collocation method used for the varying number of velocity spline control points.

As expected, the number of control points defines the result's accuracy, being a higher number a better approximation for the optimal solution of the problem. Results show that 16 control points, the maximum error for the trajectory elapsed time is only 1.03%, which is within a good margin of error and assures close to optimum solutions. Furthermore, this was achieved with a decrease of over 10% in computation time.

23

Finally the displacement spline study was conducted in a similar manner with 16 control points for both force and velocity. Figure 3.7 and Tab. 5.5 comprises these results.
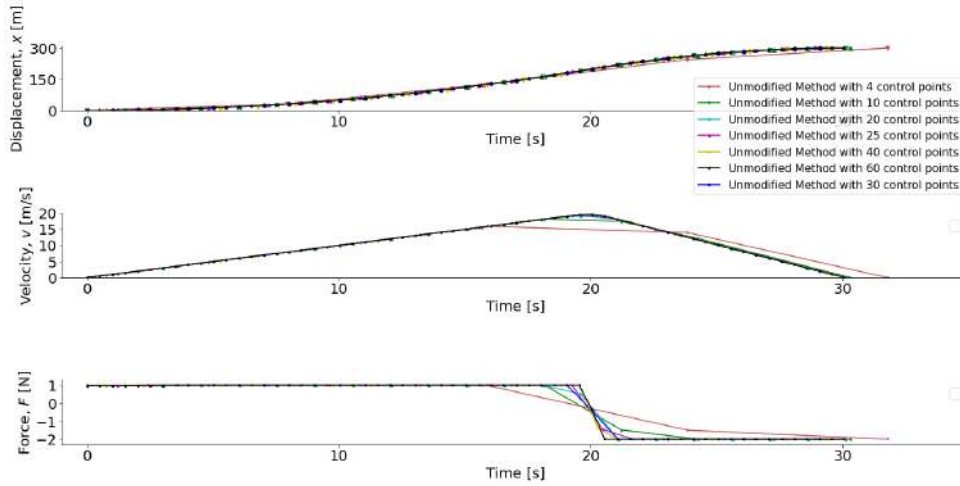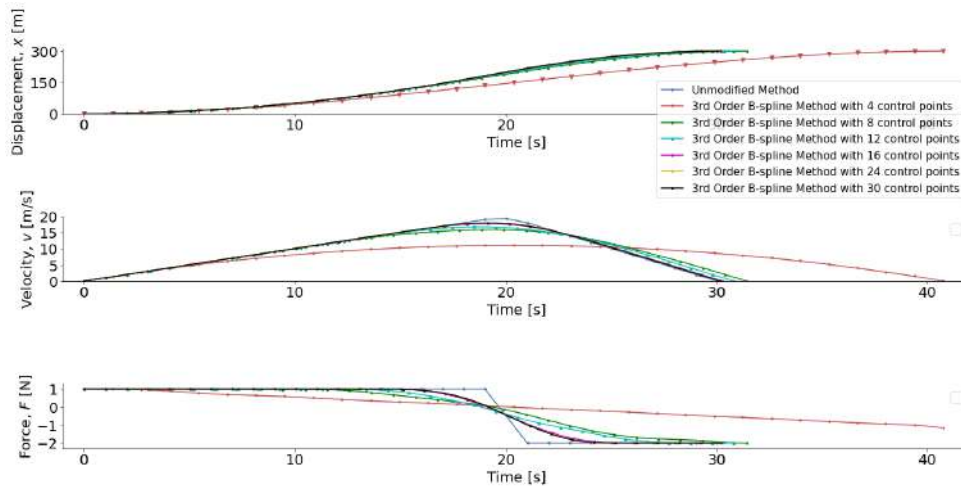

Figure 3.7: Problem's design variables values throughout time with both the modified and unmodified version of the direct collocation method used for the varying number of displacement spline control points.

Once again, a lower number of control points produced worse results and a higher number of control points achieve a better solution. However, although being faster than the unmodified version, the displacement's results also decreased the efficiency of the optimization in some cases - the function evaluations were slightly higher. This might be explained by the large flexibility of the splines that worsen the convergence.

Table 3.1: Results for the efficiency study conducted for all the B-spline implementations: thrust, velocity and displacement.

	Thrust B-spline				Velocity B-spline				Displacement B-spline			
Control Points	Func Evals	Grad eval	Time	Error (%)	Func Evals	Grad eval	Time	Error (%)	Func Evals	Grad eval	Time	Error (%)
4	22	22	34.5	15.3	38	33	34.3	14.8	41	35	40.8	36.3
8	21	21	31.0	3.7	46	44	30.9	3.2	182	81	31.4	5.1
12	20	20	30.3	1.4	58	54	30.3	1.3	277	111	30.8	3.0
16	20	20	30.0	0.5	54	53	30.2	1.0	98	61	30.3	1.3
24	20	20	30.0	0.2	66	66	30.0	0.5	56	55	30.2	1.0
30	21	20	29.9	0.1	69	68	30.0	0.5	66	64	30.2	1.0

3.1.4 Final Remarks

B-spline implementation increased the overall efficiency of the trajectory optimization, but interesting results surfaced when implementing sequentially the spline transformation. Contrary to what would be expected, although transforming both the state and control variables of the problem into b-splines resulted in efficiency gains, the best gain was achieved by only using the control variable (force) as a b-spline approximation which produced the most accurate results of all three methodologies studied.

Another important observation is related to the trajectory and time accuracy of the optimization when using the implemented spline method. Although force and velocity physical representation did not converge to the unmodified solution, the displacement's spline results and the elapsed time converged to low relative errors easily. This implies that although the velocity and force fields were not accurately

described, the trajectory itself was very well described. Being the latter the objective of this work, the spline implementation highly increases the efficiency of the optimization with low cost in the trajectory results.

Finally, b-splines also relax the high demands of the initial solution of the trajectory optimization for this problem and is expected to do so on the main problem at hand. Trajectory optimization results and convergence is highly dependent on the initial solution guess, which results in a trial and error study most of the time. B-spline implementation resulted in a better acceptance of the initial conditions, having the system more freedom to search new solutions.

Since the B-spline approximation method showed good efficiency improvements and solution finding easiness, it was implemented in the final problem optimization framework (more details in Chap. 5).

3.2   Propulsion Model

As Sec. 2.4 described, the propulsion system of the aircraft is composed by a battery, a controller, a motor and a propeller. In an attempt to model this system as close as possible to reality with low computational requirements, several experimental data were used for curve fitting models of power and thrust with velocity and throttle. The goal of this model is to calculate the generated thrust from throttle input. Two distinct models with different fidelities will be created: the first one will consider a constant power source; the second will add a battery discharge curve. The experimental data and resulting models are explained in detail next.

3.2.1   Wind Tunnel Experimental Data

To retrieve the propulsion motor response, two different experimental analyses were conducted, Full Throttle response and Variable Throttle response, conducted at different airspeeds.

The experiment included an open wind tunnel with a force scale apparatus to measure electric voltage and current and the propeller thrust. The propulsion system, apart from the battery, was connected to the force scale and powered by a power supply. Electrical power is obtained multiplying voltage with current, and Thrust values are obtained from reading from a load cell. The experimental apparatus is presented in Fig. 3.8.
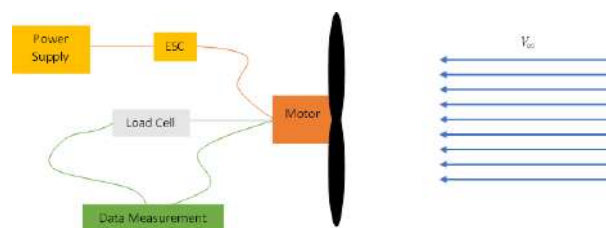
Figure 3.8: Experimental apparatus schematic for the full throttle and variable throttle responses.

The experiment was conducted by setting the wind tunnel speed to specified values and turning on the propulsion system either at full or with variable throttle. The full throttle response will provide the

25

maximum thrust output of the propulsion system and the variable throttle will describe how the propulsion system behaves as a function of the throttle control variable.

Full Throttle Data

For the constant power supply case, the propulsion system was tested and its data collected for several airspeeds. Results are presented in Fig. 3.9.

The experiment was conducted with the propulsion system described in the ACC 2022 competition regulations [16] and a generic power supply and ESC. The material and experiment settings were:

- Propeller - *Aeronaut CAMcarbon Light 10"x6"*
- Motor - *AXI 2826/10 GOLD LINE V2*
- Power Supply - 12V
- Esc - full throttle

As expected, the thrust tend to be lower as the airspeed increases. This is explained by the reduction of the propellers induced momentum on the flow. As the speed increases, the difference between the input and output speeds in the propeller decreases, which lowers the momentum increase in the fluid, which consequently reduces the thrust produced.

This data reveals important information about the propulsion system maximum values. First, maximum thrust is around 17 N. Secondly, thrust varies non-linearly with speed.

These results served as a good verification as to why simple propulsion models (momentum theory) do not perfectly describe a system. Figure 3.9 also presents the same experimental results with two additional curves, a quadratic fitting curve for the experimental data and a theoretical curve derived from Eq. (2.7) with a loss factor k of 1.5.
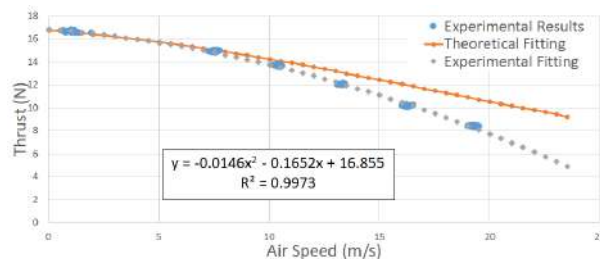
Figure 3.9: Wind tunnel data of the motor thrust response at full throttle: experimental fit and theoretical fit.

The experimental quadratic curve proves to be a good fit for the results at hand, proven by the R^2 of 0.9973. On the other hand, looking at the theoretical curve, for low airspeeds (0-10 m/s), the results are coherent but for higher airspeeds the discrepancy increases and the results clearly differ from the real values observed. This is expected since this simple theoretical model does not consider several losses (see Sec. 2.4). The k factor introduced, although it corrects the initial thrust value of the curve, represents a linear loss factor that does not fit well with non-linear loss phenomena.

Although the simple theoretical propulsion model tested did not result in good approximations, it proves useful if project did not have a specific propulsion system, since it is not possible to analyse

in experiment every possible propulsion system. For the rest of this work, the experimental fit curve presented in Fig. 3.9 will be used to describe the maximum thrust values available for the maximum power input values.

As for the power consumption of the propulsion system for this experimental analysis, Fig. 3.10 presents the measured data as well as the quadratic fitting function for that data. This data will provide the maximum power consumption at each airspeed value that will be used to locate the correct point in the thrust-speed curve.
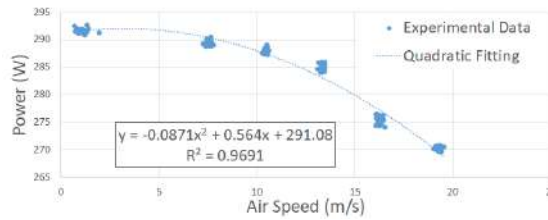
Figure 3.10: Wind tunnel data of the motor electrical power at full throttle.

Variable Throttle Data

The second experiment studied the dependence of thrust and power with the throttle input from the controller (ESC), still using a constant power supply. In this study a specific curve is analysed, however, any curve can be made possible by adjusting the ESC accordingly. This property of the system will be further discussed later.

Figure 3.11 displays the experimental of the electric power for each throttle input. Figure 3.11 (a) presents the full range experiment, while 3.11 (b) presents the active portion of the propulsion system.
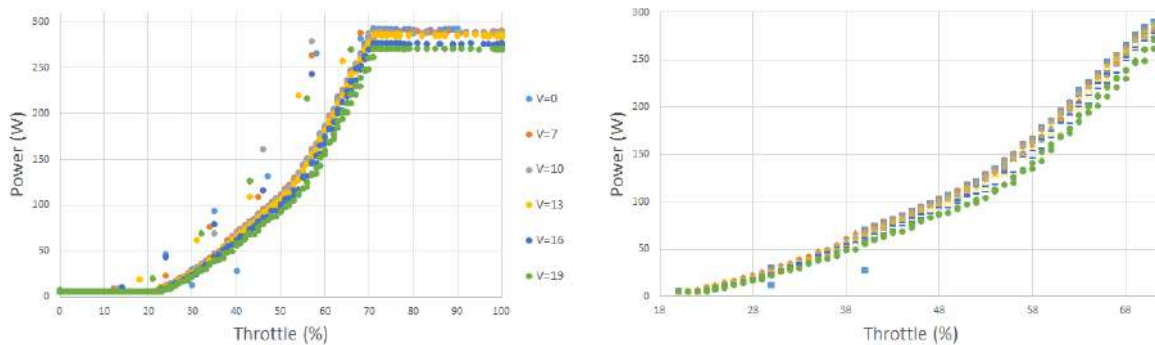
(a) Full Throttle range experimental data.

(b) Active range for the data retrieved.

Figure 3.11: Wind tunnel data of the motor electric power at variable throttle settings.

Two important aspects of this experiment can be discussed. Firstly, the dependency of power on throttle remains approximately the same no matter the airspeed. Secondly, the differences come from the maximum power reduction observed earlier on the full throttle results. Notice how in 3.11 (b) the higher the airspeed the lower the curve is and the lower the maximum power is. Additionally, the curve in 3.11 (a) has two plateaus: one at 0-20% throttle and another at 70-100% throttle. This is explained

by how the ESC works: its working principle based on rectangular waves with different width's acting on the same frequency, that is, the ESC works with pulse width modulation (PWM) that controls the power output to the motor and propeller. The higher the width the more power it delivers and vice-versa. However, these controllers have a working range. Below that range the controller does not power the motor, and above it, the controller is capped at maximum power output. This can be adjusted to coincide with the throttle range. However, studying the active portion of the controller is enough to study its properties since adapting this way would not change this zone, only flatten or elongate. Furthermore, the PWM can be programmed to change the behaviour of the curve and transform the curve into any needed function. So, as expected, the power increases with throttle and caps at different maximum levels for different airspeeds, which coincide with the maximums achieved in the first experiment.

Additionally, as Fig. 3.12 demonstrates, the experimental fitting achieved for the thrust-speed curve produces good accuracy on the experimental data achieved. This curve was achieved by using the Power consumption data retrieved at each Throttle point and using a linear approximation to deduce the Thrust with the maximum Power for a certain velocity as

$$T(\delta_t, v) = \frac{P(\delta_t)}{P_{max}} * T(v) \quad , \tag{3.3}$$

where δ_t and $T(v)$ are the throttle value and the Thrust experimental function respectively. This way, for any power-throttle behaviour, thrust can be obtained.
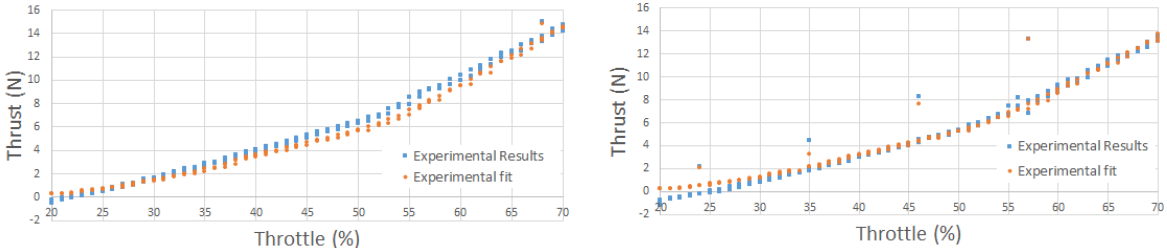
(a) Experimental fitting curve for Thrust with a air velocity field of 7m/s

(b) Experimental fitting curve for Thrust with a air velocity field of 10m/s

Figure 3.12: Two examples of experimental Thrust fitting using previous deduced function.

Sources of Error

Every experiment, because of its nature, has sources of error. Those presented here include: uncertainty in the current and voltage readings; load cell readings; and airspeed measure. These errors make the readings slightly different from reality. However, for the purpose of this work, which is to find the optimal conceptual design, the experimental data collected represents the propulsion more accurately than any other low fidelity approximation model for the system.

3.2.2 Battery Discharge Curve Approximation

Before completely defining the propulsion system, a model for the battery must be obtained based on its behaviour with time and energy consumption.

As explained in Sec. 2.4, batteries have specific discharge curves as depicted in Fig. 2.9 that depend on the discharge rate that consequently depend on their capacity. Figure 3.13 depicts a 2000mAh lithium-ion (lipo) battery discharge behaviour for different discharge rates.
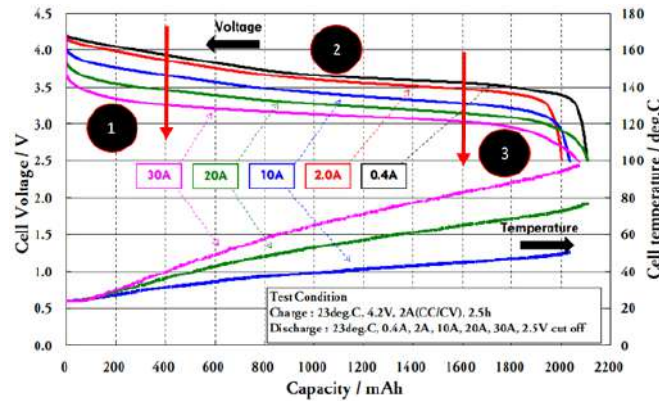
Figure 3.13: Discharge behaviour of a 2000mAh battery for 4 different discharge rates (0.2C, 1C, 5C, 10C and 15C) [49].

As it can be observed, there are three typical regions in a discharge curve of a lipo battery. The first region is characterized by a fast decrease in voltage, typically from 4.2V to 3.3V-3.9V depending on the discharge rate. This region typically lasts the first 20% of the battery capacity. The second zone is an almost constant voltage region where the voltage values change almost linearly until 80% of the capacity is reached. After that starts the third region when the battery voltage starts to rapidly decline and it is unwise to use the battery past this point.

Additionally, it is worth mentioning that the higher the discharge rate, the lower the second zone plateau is. For the work at hand, the aircraft flight should be around 5 minutes, which, at a maximum power of 280W (based on experiments) needs $E = 5 \times 60 \times 280 = 84kJ$ of energy. This leads to a range of 2000-10000 mAh batteries. Examining Fig. 3.13, the plateau reached for the curves is between 3.3V and 3.9V, thus, the value of 3.7V will be considered to define the voltage at the beginning of this plateau.

The battery discharge approximation model intends to simulate the battery discharge curve considering its stored energy and the three regions aforementioned. Firstly, in the first 20% capacity, a rapid exponential discharge zone from 4.2V to 3.7V is considered. Afterwards, from 20% to 80% capacity, a linear decline in voltage is considered from 3.7V to 3.2V - notice that the higher the batteries capacity is, the more time will higher voltage remain. Finally, after 80% capacity, the battery is assumed empty. Figure 3.14 presents the curve approximation implemented in this thesis and two battery modulation for two different capacities as an example.

This model was constructed with one initial exponential zone calculated, followed by a linear zone
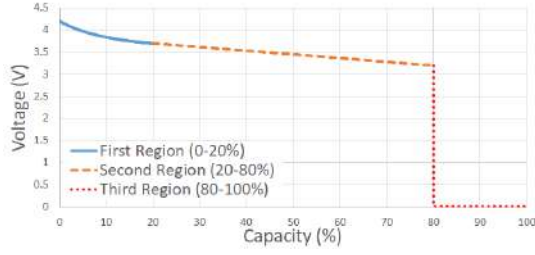
(a) Battery discharge model for any battery on this work dependent on the Capacity percentage consumed.
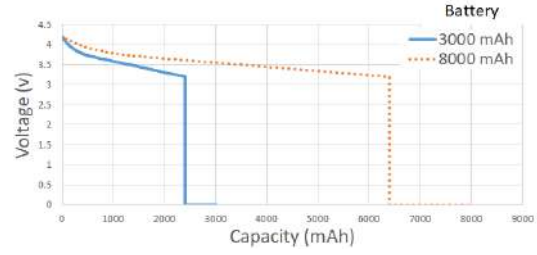
(b) Battery discharge model application for a 3000 mAh and 8000 mAh batteries.

Figure 3.14: Implemented discharge curve function for any battery based on the work's problem characteristics.

from 3.7V to 3.2V and a flat zone with 0V available. The exponential zone is defined as

$$V_x = V_f + (V_i - V_f)\frac{e^{-C_{\%_x}*A} - e^{-C_{\%_f}*A}}{e^{-C_{\%_i}*A} - e^{-C_{\%_f}*A}} \quad , \text{with} \quad A = 10 \quad , \tag{3.4}$$

with V_x, V_i, V_f, $C_{\%_x}$, $C_{\%_i}$, $C_{\%_f}$ and A the voltage at a given point x, the voltage at the initial and final points of the region, the capacity percentage depleted at a given point x and at the initial and final points of the region, and the exponential factor, respectively.

Note that this analysis was made for a single cell battery, the model implementation is explained next for a three cell battery as imposed by the ACC 2022 regulations [16].

3.2.3 Model Implementation

As aforementioned, there were two models implemented for this work: a simple constant power model and a battery discharge model.

Constant Power Propulsion Model

For the constant power model, the battery is assumed as a constant power source where the diminishing of the voltage through time is neglected.

This model is built based on the power-throttle, thrust-speed and power-speed curves. Firstly, a throttle input δ_t is given and with it, using the power-throttle curve, the power given to the propulsion system is calculated. Afterwards, using the power-speed curve, the maximum power for the given speed is determined. With it, using the thrust-speed curve, the output thrust is calculated. Energy is calculated by keeping track of the power chosen by the throttle input in each collocation point. Figure 3.15 presents the implemented model schematically.

For this model, the power-throttle curve was, based on the ESC characteristics, transformed into a linear region to simplify the problem. The new transformed power-throttle curve is presented in Fig. 3.16.
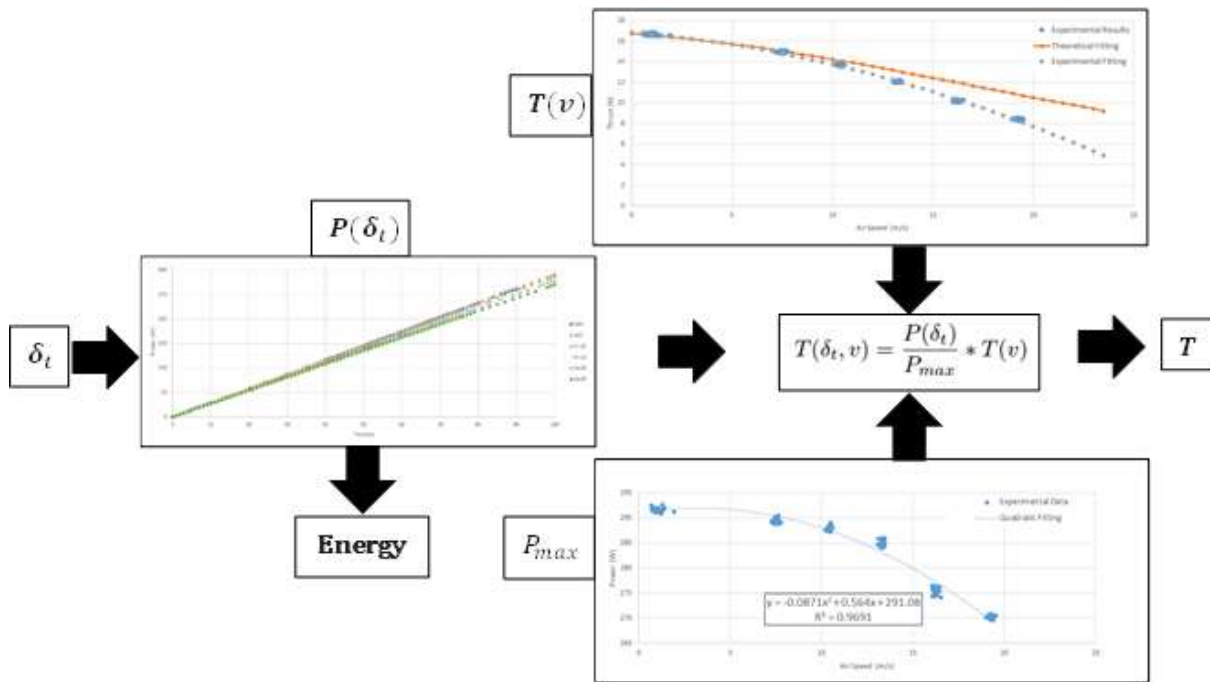
Figure 3.15: Propulsion model for the constant power battery source.
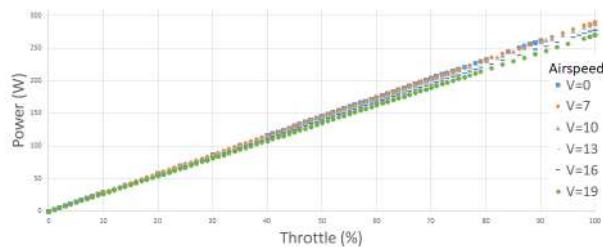
Figure 3.16: Modified power-throttle curve for different airspeeds.

Battery Discharge Propulsion Model

For the battery discharge propulsion model, the complexity is increased by adding the maximum available power decrease on the battery derived from its usage in flight.

This model will use as input the electric current injected into the propulsion system. For the propulsion system used - brushless motor - the ESC controls the input current of the system while maintaining the voltage input. Higher current implies higher power which produces increased thrust. At a given point in the batteries voltage-capacity curve, the voltage is registered. Afterwards, with the input δ_t given, the input current is calculated and, consequently, the power input is deduced. Then, the thrust is calculated as the first model explained, by using the thrust-speed and the power-speed curves.

In this case, a current-throttle curve (Fig. 3.17) is adopted with the same reasoning as the modified power-throttle, a linear approximation. This curve was based in the power-throttle one by dividing the power results by the average value of the voltage throughout the experiments - 11.5V.

Finally, the discharge percentage of the battery is calculated by keeping track of the current input at each collocation point and multiplying these values by the elapsed time in flight. This discharge
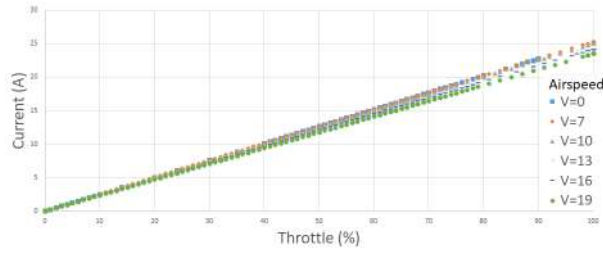
Figure 3.17: Current-throttle curve for different airspeeds.

percentage is then used to calculate the voltage input of the battery at each collocation point. The schematic of the model is presented in Fig. 3.18.
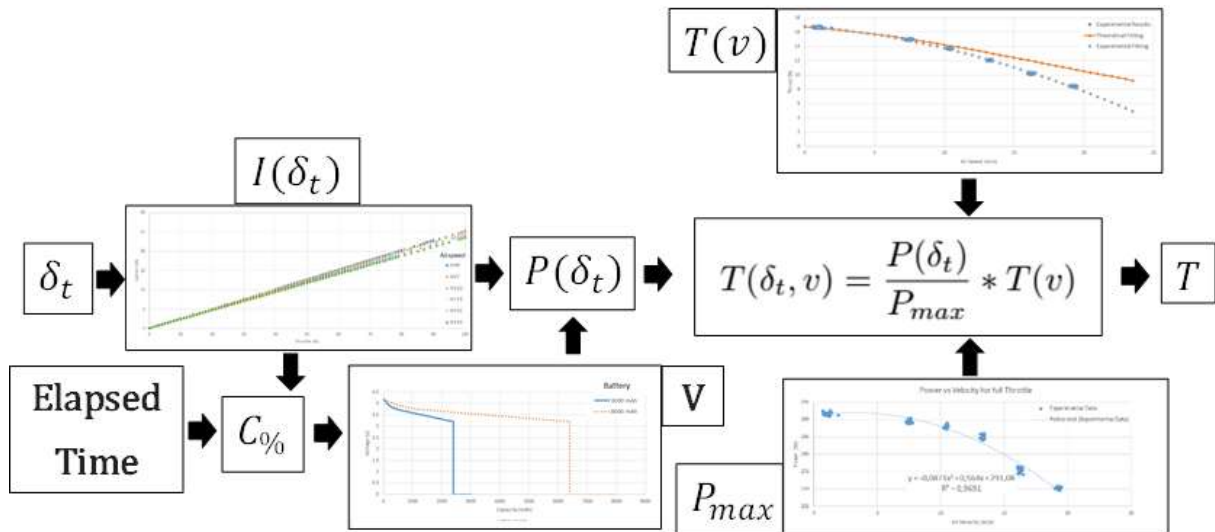
Figure 3.18: Propulsion model for the modelled discharge battery.

3.3 Competition and Flight Related Models

In this section, the specific models implemented to describe the ACC competition aircraft are explained. First, a general description of the aircraft and its modelled dynamics are explained and, afterwards, the models are introduced.

3.3.1 General Aircraft Configuration

To better understand the problem and the solution this thesis presents, the typical aircraft configuration and dynamics must be explained first. Following Olissipo Air Team's configuration idea, the aircraft is thought to be a tail dragger where most of the take-off run is conducted supported only on two wheels. Figure 3.19 presents the team's 2021 prototype where the typical configuration sought for can be visualized.

Additionally, the tail is dimensioned as a V configuration to meet the team's requirements and allow for a lower structural weight. Since OpenAeroStruct [30] only models wings and tails, the aircraft design

32

Figure 3.19: Olissipo Air Team's 2021 prototype configuration.

variables are focused on these two surfaces (more details in Chap. 5). However, drag additions due to the aircraft body are considered (see Subsec. 3.3.2).

For the dynamics, to simplify the problem at hand and since the trajectory planned for the aircraft is high radius turns with most flight forward, only the longitudinal dynamics are implemented, where only the longitudinal components of forces, velocity and position are considered.

3.3.2 Cargo Bay Drag Model

The cargo bay of the aircraft is designed to carry a variable number of simulated blood bags. The number of bags controls the size of the payload and it is determined by the aircraft performance which is highly dependent on the aforementioned size. The model proposed calculates the added drag on the aircraft based on the number of blood bags used.

The first problem considering this model is the bags arrangement inside the cargo bay. It is expected for the airplane, based on the team's early studies, to carry between 5 to 10 blood bags depending on the speed definition for each aircraft. For this work, pile arrangements are considered as $m \times n$, where n describes the number of upward blood bag lines and m the described the number of possible lined-up bags. Figure 3.20 schematically describes these configurations.
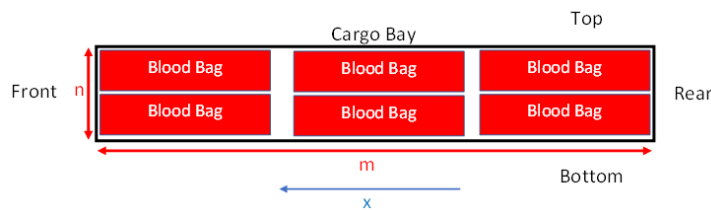
Figure 3.20: Cargo bay pile arrangement scheme.

The pile arrangement and the size of the blood bag - 150 x 100 x 30 mm^3 [16] - will define the size requirement for the cargo bay. All is needed is a parasite drag calculation model to describe its influence on the flight. Following [50], any aircraft minimum, zero lift, parasite drag component influence can be calculated as

$$C_{Dmin} = \frac{1}{S_{ref}} C_f \times FF \times IF \times S_{wet} \quad , \tag{3.5}$$

where S_{ref}, C_f, FF, IF and S_{wet} represent the reference area, surface skin friction coefficient, form

factor, interference factor and surface wetted area, respectively.

For the fuselage, the interference factor is considered 1 and the form factor is, based on Hoerner [51],

$$FF = 1 + \frac{1.5}{f^{1.5}} + \frac{7}{f^3} \quad , \tag{3.6}$$

where f is the fineness ratio, described as

$$f = \frac{l}{\sqrt{\frac{4A_{max}}{\pi}}} \quad , \tag{3.7}$$

for any cross-sectional geometry. Since the fuselage - cargo bay - is directly behind the propeller turbulent induced flow, the skin friction coefficient used is based on a full turbulent flow approximation given by Schlichting and Gersten [52] relation, given by

$$C_f = \frac{0.455}{(log_{10}R_e)^{2.58}} \quad , \tag{3.8}$$

where R_e is the Reynolds number. Finally, the fuselage wetted area is constituted by the fluid immersed surfaces - two lateral sides and the under side (the wing is dimensioned to be mounted on top of the cargo bay). This calculation depends on the $m \times n$ scheme chosen and it is increased by the electronic space and tail joint needs. Electronic components have a predicted 200mm space reserved and the tail connection has 150mm of space reserved.

In order to choose the best pile arrangement for the model at hand, a comparison was produced using the proposed model. Figure 3.21 presents the parasite drag for different types of blood bags arrangements.
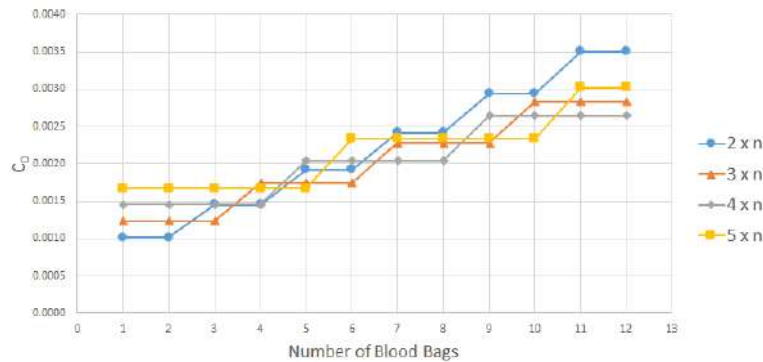
Figure 3.21: Cargo bay parasite drag estimation for different blood bag arrangements.

Low number of blood bags tend to benefit smaller m arrangements, while higher number of blood bags tend to benefit higher m arrangements. This is due to the fact that for higher m arrangements, lower blood bags create unnecessary large fuselages. On the other hand, for a higher number of blood bags, higher m arrangements have a thinner body and a lower frontal area.

From these results the best configurations are a $3 \times n$ or a $4 \times n$ pile arrangements. Since neither is objectively better than the other, the proposed model will use the lower C_D configuration for the number

of bags evaluated.

3.3.3 Rhombus Box Model

An interesting aspect of the ACC 2022 edition is the addition of a measuring rhombus box that limits the fully mounted aircraft dimensions in a ready for take-off configuration. The box is based on a quadrilateral geometry with equal sides where the inner angle β can be freely modified. Figure 3.22 presents the rhombus box design given by the ACC regulations [16].
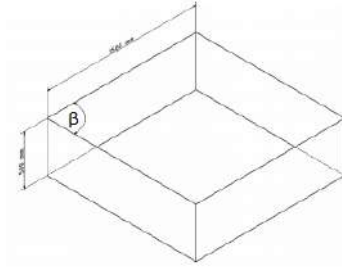
Figure 3.22: ACC 2022 competition rhombus box [16].

This new constraint is meant to limit the total aircraft size. Higher wing span is always desirable for a higher aerodynamic efficiency, however, maximizing it in the larger diagonal reduces the available tail distance which, consequently, limits the stability margin of the aircraft. A balance must be met to achieve the best performance, hence the purpose of the optimization and this work.

To model this box and the aircraft size inside it, a simple assumption is considered - the leading edge at the wing tips are coincident with the two sides of the box, with the wings positioned in the box's diagonal. Afterwards, the wing chord must fit inside the box, as well as the tail and the propulsion system ahead of the wing root leading edge. Figure 3.23 presents a general aircraft disposition inside the rhombus box with the proposed model.
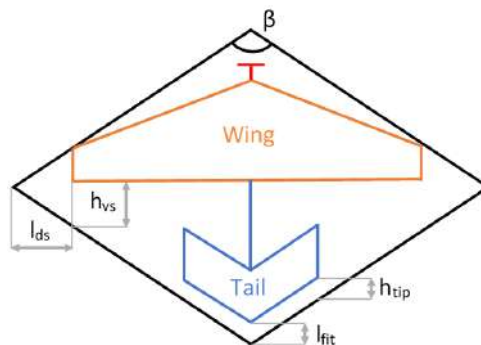
Figure 3.23: General configuration for the rhombus box model used.

For a chosen rhombus box angle β, the wing, tail and propulsion system positions are verified and, in case of failure, the optimizer changes the rhombus box angle or the aircraft geometry.

Starting with the wing geometric constraints, since the wing tips leading edge coincides with the box edges, as shown in Fig. 3.23, the available space for the wing tip chord must be determined as well

35

as the space available for the wing span. This can be achieved through the use of the wing span and rhombus box angle as to obtain the lateral diagonal space

$$l_{ds} = \sin(\frac{\beta}{2}) \times l_r - \frac{b_w}{2} \tag{3.9}$$

and the vertical space available at tip chord

$$h_{vs} = \tan(90 - \frac{\beta}{2}) \times l_{ds} \times 2 - c_{w_{tip}} \quad , \tag{3.10}$$

where l_r, b_w and $c_{w_{tip}}$ are the rhombus box lateral side length, wing span and wing tip chord length, respectively.

As for the tail, two additional verifications must be achieved, one with respect to the tail length fit distance (l_{fit}) and the other with the surface fit inside the rhombus box (h_{tip}). These equations are described as

$$l_{fit} = l_r \cos(\frac{\beta}{2}) - ((l_t - \frac{b_w}{2} \tan(\Lambda) + \tan(90 - \frac{\beta}{2})l_{ds} + 0.25c_w - 0.25c_t) + c_{t_{root}}) \tag{3.11}$$

and

$$h_{tip} = (l_r \cos(\frac{\beta}{2}) - (l_t - \frac{b_w}{2} \tan(\Lambda_w) + \tan(90 - \frac{\beta}{2})l_{ds} + 0.25c_w - 0.25c_t)$$
$$- \frac{b_t}{2} \tan(90 - \frac{\beta}{2})) - (c_{t_{tip}} - \frac{b_t}{2} \cos(\Lambda_t)) \quad , \tag{3.12}$$

where l_t, c_w, c_t, $c_{t_{root}}$, Λ_w, $c_{t_{tip}}$ and Λ_t represent the tail length, wing mean chord, tail mean chord, tail root chord, wing sweep angle, tail tip chord and tail sweep angle, respectively.

These are the metrics used for the geometric constraint of the problem and are also present in Sec. 3.23.

3.3.4 Stability Model

As mentioned throughout this work, this work only considers longitudinal motion. From a static stability point of view, only the longitudinal stability of the aircraft is considered which is based on three major aspects: wing and tail lift and the aircraft's center of gravity (CG) location.

Aircraft trim is achieved b with a null balance of forces and moments. In the context of this problem, this is achieved by the null balance of vertical forces and null balance in pitching moment.

However, longitudinal static stability implies that for a slight change in the aircraft's pitch angle, the vehicle must tend, without intervention, to a stable point. To control this behaviour, the term 'static margin' is introduced, where the variation of the aircraft pitching moment with the aircraft angle of attack (α) is evaluated - C_{m_α} [53].

The longitudinal static stability of the aircraft can be determined recurring to the coefficient of pitching moment

$$C_m = C_{m_0} + C_{m_\alpha}\alpha = C_{m_0} + C_{L_\alpha}(h - h_n)\alpha \quad , \tag{3.13}$$

where C_{m_0}, C_{L_α}, h and h_n are the coefficient of moment at zero angle of attack, derivative of C_L in respect to α, the adimensionalised CG location of the aircraft and the adimensionalised location of the neutral point, respectively. To achieve stability, a negative slope is desired, so it counters the aircraft perturbation motion. This implies positive static margin (K_n) term, with

$$K_n = h_n - h \quad . \tag{3.14}$$

The CG location is of the utmost importance, since it delimits the point where a stable aircraft becomes unstable. This position is called the neutral point, denoted as h_n and corresponds to the adimensionalised distance from the wing's leading edge to the CG's location. Following Gudmundson [53] balance equation (forward CG - Fig. 3.24), the neutral point location can be determined as

$$h_n = h_{AC} + \eta_{HT} V_{HT} \frac{C_{L\alpha_{HT}}}{C_{L\alpha_{wing}}} (1 - \frac{2C_{L\alpha_{wing}}}{\pi AR}) - \frac{C_{m\alpha_{AC}}}{C_{L\alpha_{wing}}} \quad , \tag{3.15}$$

where h_{AC}, η_{HT}, V_{HT}, $C_{L\alpha_{HT}}$, $C_{L\alpha_{wing}}$, AR and $C_{m\alpha_{AC}}$ are the distance from the wing leading edge to the wing aerodynamic center, horizontal tail efficiency, horizontal tail volume coefficient, horizontal tail lift curve slope, wing lift curve slope, wing aspect ratio and longitudinal stability contribution of components other than the wing, respectively.
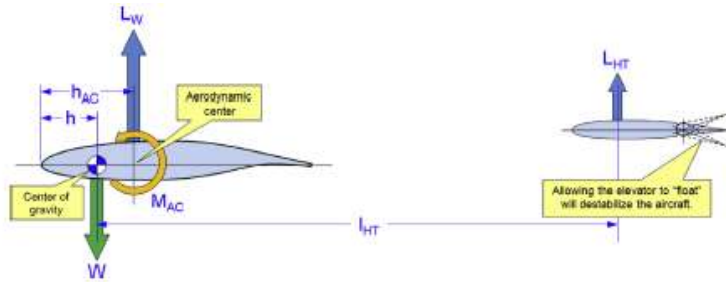
Figure 3.24: Forward CG wing - horizontal tail system [53].

Although the static margin can be calculated using the aforementioned result, it presents a high computational effort since it needs several parameters only obtained through the use of analysis in each optimization cycle (to obtain the aerodynamic derivatives). Studies from *XFLR5* [54] show that all similar configurations to the ones studied in this thesis present negative slopes, which confirms the aircraft's static stability - Fig 3.25 and helps to only consider the trim condition at each collocation point along the trajectory. Thus, only a trim model is used where, along the trajectory, the pithing moment coefficient must be null, this implies that the aircraft is trimmed at each position.

Furthermore, analysing the stability of these simulations, a static margin of around 10-15% is found.

Vertical Stabilizer

Since the aircraft is considered to have a "V" tail design, it is important to consider the vertical fin implications on the problem formulation. With this in mind and based on Gudmundson [53] recommendations, the vertical fin of the aircraft can be predicted by recurring to the vertical tail volume coefficient,

37
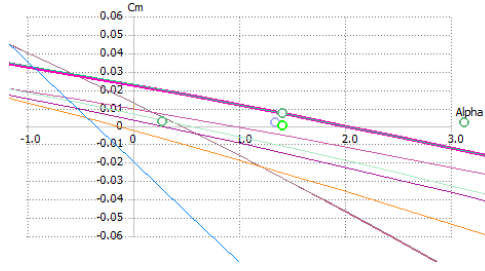
Figure 3.25: C_m values obtained through the use of XFLR5 computational capabilities.

given as

$$V_{VT} = \frac{S_{VT}l_{VT}}{S_{ref}c_{ref}} \quad , \tag{3.16}$$

where S_{VT} and l_{VT} are the vertical tail area and the distance between the wing and tail quarter chords (considering mean geometric chord).

Since the tail is a V tail configuration, the vertical fin's area is determined by considering the projected planform of the tail area on the vertical plane.

Historical values suggest the volume coefficient should be between 0.04 and 0.09, and these should be the limit values to certify the correct aircraft tail sizing,

$$0.04 \leq V_{VT} \leq 0.09 \quad . \tag{3.17}$$

3.3.5 Flight Model Integration and Usage

For this project, it is important to clarify the methodology used for the analysis of the different flight segments. In this section, the flight analysis is described as a mean to better understand not only the design variables and constraints influence on the results but also the inherently errors caused by the assumptions made throughout the work.

Take-off Segment

The take-off segment starts when the electric motor is activated and ends when the aircraft leaves the contact with the runway. There are two typical ways to calculate take-off runway behaviour - numerical integration methods and general solution of the equation of motion [55].

Since this work is a conceptual design optimization and the fidelity of the design results are low due to the errors associated with the models used (see Sec. 1.2), implementing a numerical integration method for the take-off dynamics would not be consistent with the other results. For this reason and for optimization efficiency, the general solution of the equation of motion during take-off motion equations was used based on Gudmundson [55]. This solution involves finding the take-off distance travelled by knowing the average take-off speed and all forces acting on the aircraft on the track: lift, drag, weight, thrust and wheel friction.

First, the average speed is determined, following Gudmundson [55], as

$$V_{avg} = \frac{V_{LOF}}{\sqrt{2}} \quad , \tag{3.18}$$

where V_{LOF} is the lift-off speed,

$$V_{LOF} = 1.1 \times \sqrt{\frac{2W}{\rho S C_{Lmax}}} \quad , \tag{3.19}$$

where W, ρ, S and C_{Lmax} are the aircraft weight, air density, reference area (wing surface area in this case) and maximum C_L achieved during the runway, respectively.

Second, lift and drag values are calculated assuming the C_L and C_D coefficients for the take-off. These were determined recurring to a *XFLR5* analysis (see Fig. 3.26) and the cargo bay model implemented and were defined as 0.3 and 0.02, respectively. The weight (W) and thrust (T) are given as design variables.

(a) C_D results.

(b) C_L results.
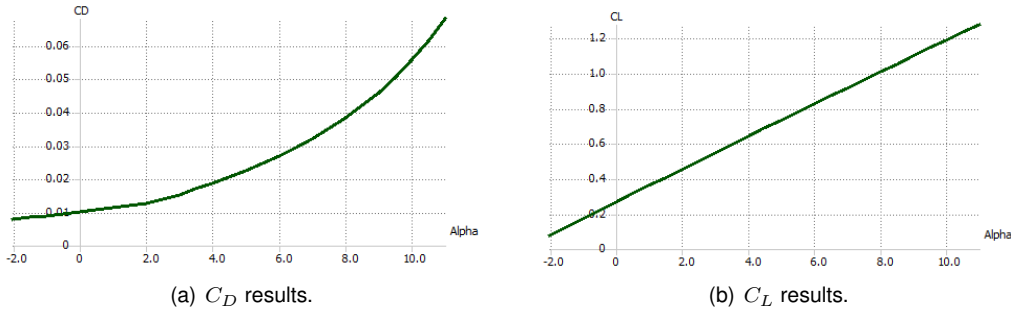
Figure 3.26: XFLR5 analysis of the C_L and C_D variation with α for the Olissipo Air Team 2021 prototype.

The wheel's friction assumes a two wheel friction model. Since this ACC's competition is located in a grass track (small dry turf), the friction coefficient is quite significant and based on bibliography [55] it should be around 0.07. The friction force is given by

$$F_{wheel} = \mu_{track} \times R \quad , \tag{3.20}$$

where μ and R describe the wheel's friction coefficient and the normal reaction on the wheels.

Assuming the design conditions described in Sec. 3.3.1 and the theory in [55], the results for the distance travelled in the take-off segment can be estimated by assuming a constant acceleration as

$$S_{to} = \frac{V_{lof}^2 W}{2g[T - D - F_{wheel}]} \quad . \tag{3.21}$$

This formulation is dependent on the wing's geometry (L and D) and structural (W) design variables as well as the propulsion variables.

Figure 3.27 shows a generic collocation point in the trajectory and all the applied forces in this segment, where R represents the ground reaction forces..
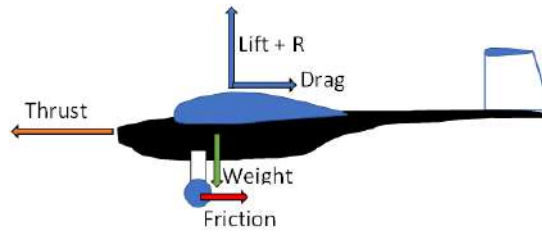
Figure 3.27: Applied forces in take-off.

Climb Segment

Climb segment is implemented in this work with a variable climb angle and the trajectory collocation method described in Sec. 2.5. For the dynamic implicit numerical integration method (collocation), the equilibrium of forces in both z and x (global referential) directions must be respected as well as the dynamic defects. For this, the forces in each collocation points must be determined.

For this segment, the weight W is given by the payload and the structural weight, the lift L and the drag D are calculated in the aerodynamics module using the VLM method of *OpenAeroStruct* and the thrust T is given by the propulsion model used as a function of time and speed.

The climb angle is set as a design variable in this segment to allow the optimization do choose the best flight trajectory in this simplified model.

Figure 3.28 shows a generic collocation point in the trajectory and all the applied forces in this segment.
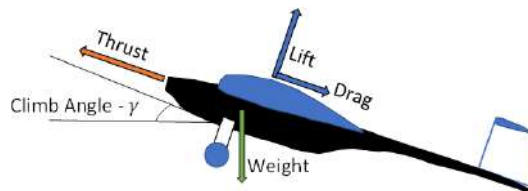
Figure 3.28: Applied forces in climb.

Cruise Segment

Cruise respects the same equilibrium and dynamic restrictions as the climb segment and also allows for a variable descent angle as a design variable.

Figure 3.29 shows a generic collocation point in the trajectory and all the applied forces in this segment.

Flight Segments Integration

Finally, all segments are integrated in the optimization as follows:

• Take-off is implemented as a calculation outside of the trajectory model used that determines the take-off distance as well as the take-off speed. Additionally, it verifies if the flight is valid and if it is worthy of bonuses (see Sec. 5.1);
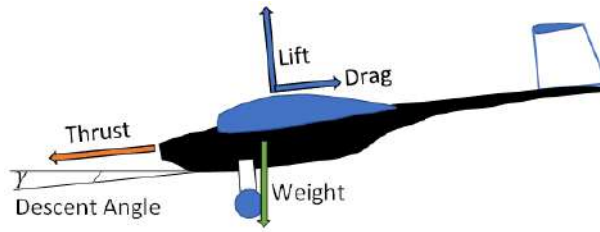
Figure 3.29: Applied forces in cruise.

- Climb starts the trajectory and the collocation method and ends when one collocation point reaches at least 60 seconds, where it is registered the altitude achieved in this segment to further calculate the climb score (see Sec. 5.1);
- Cruise starts in the last climb collocation point and ends after 120 seconds where the total distance travelled in this segment is registered and used for the distance score calculation (see Sec. 5.1).

To close all score needs, if the flight is determined valid, the payload's mass is registered and the payload score is calculated and integrated in the final score calculation along with the take-off bonus if applied.

3.3.6 Aircraft Design Variables

Having all models for the framework set, it is important to have as reference all the parameters described in the problem, their meaning and their boundaries. Some of these are design variables while others are constraints as summarized in Tab. A.1 and Tab. A.2.

As it can be seen, the problem comprises several different parameters and metrics. It is important to note that the framework handles a higher number of intrinsic problem parameters that are derived from these or necessary additional calculations from these parameters, as is the case for the aerodynamic forces or the propulsion forces.

There are four types of parameters here present: *Design* variables intend to show framework free variables, where the optimization can cycle through different values of these variables within its boundaries; *Constraint* are variables dedicated to formulate the problem as realistic as possible by applying necessary conditions for the problem; *Constants* represent fixed parameters set for the problem that are constant throughout every analysis; finally, *Fixed Design* variables are design variables that can be changed from input from the user but are not permitted to change during optimization. These last can be useful to study some aircraft parameters within pre-determined values, as is the case for the empty aircraft's CG which is constrained by the structural design of the whole aircraft.

The control points of the aircraft variables (when applicable) where chosen to allow enough freedom for the optimizer to enhance design performance but also kept realistic in terms of construction possibilities of the aircraft. Control points for trajectory variables were defined based on convergence studies presented in the next chapter.

Finally, boundaries were chosen to limit the aircraft to possible and reasonable values while allowing enough freedom for the system to search and find the optimum solution.

41

Chapter 4

Framework Structure and Verification

In this chapter, the framework developed along this thesis is explained and its results are verified.

The framework consists of a modified *OpenAeroStruct* program where a trajectory collocation method is implemented as well as a new propulsion model and a possibility to manage both control and state variables with b-spline interpolations with number of control points chosen by the user.

The purpose of this framework is the creation of a simple and quick design tool to foresee the optimized starting point for the aircraft's design.

Here the coupling between disciplines will be discussed, specially the aerodynamic-structural relations. Additionally, the models and their connections will be explored for a detailed analysis and comprehension. Verification will be the final segment of this chapter where the results will be analysed to assure they are within the acceptable boundaries of the problem.

4.1 Framework Overview

The created framework comprises three major elements: Problem variables, which include all state, control, geometric and auxiliary variables for the problem's trajectory and aircraft; Mission points calculations, which involves wing geometric variables definition, the aero-structural coupling as well as the propulsion calculations and all the needed pre-calculations; Mission performance and constraints, in which the needed measurements are taken to evaluate the aircraft performance.

Figure 4.1 comprises the N2 diagram given for the framework at hand where the three major elements are represented.

In the next subsections the full optimization process of the framework is covered from beginning to end.

4.1.1 Problem Variables

The framework starts its optimization process by defining the problem variables at first. These variables describe the trajectory of the aircraft as well as the aerodynamic and structural geometric variables
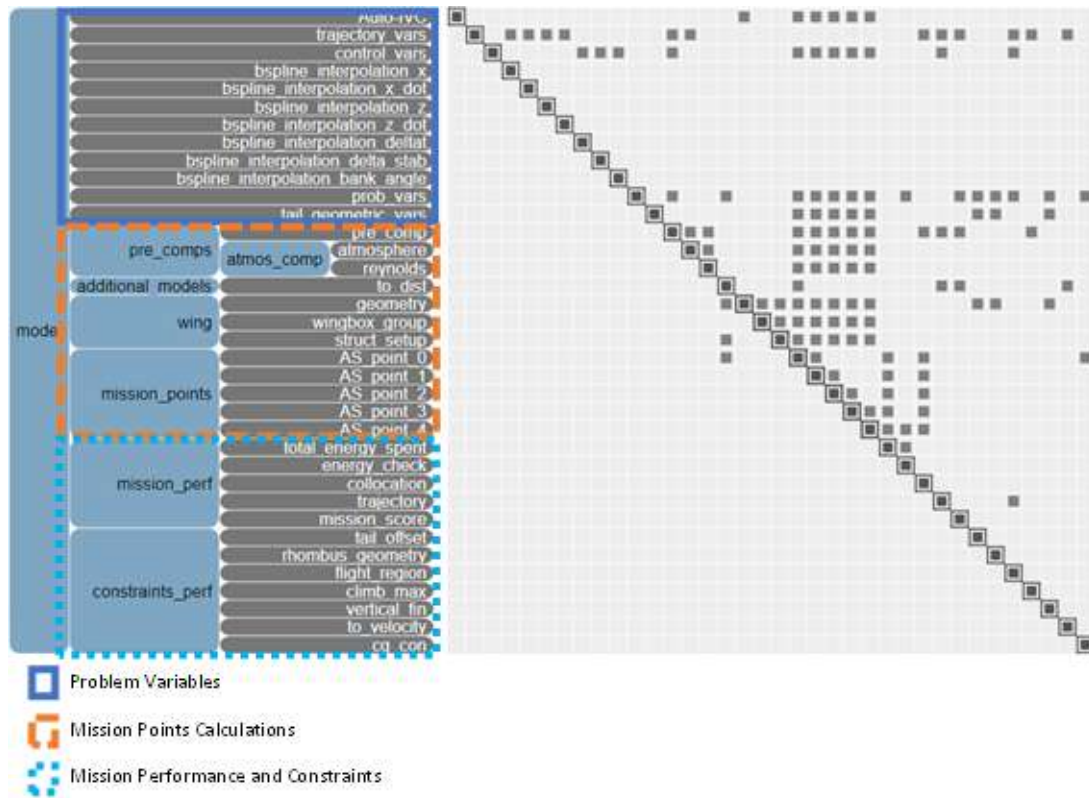
Figure 4.1: N2 diagram overview of the created framework.

that describe the aircraft and also additional variables that control payload, available energy, etc.. Figure B.1 presents the modules created for the design variables.

In its majority, these variables work only as input (green lines flowing out of the modules) for the rest of the framework modules. However, for this framework, a b-spline module for every control and state variable is added that receives control point values and produces an n point b-spline interpolation calculation (see Subsec. 3.1.3). Note that these b-spline interpolations are optional on the framework, being the user's choice to use them as well as the precision of these by controlling the number of control points.

The optimization framework asks the user to define initial values to be used for each of these variables, allowing to define these values as fixed (no change allowed) or design variables (allowing for the optimizer in each cycle to change the value and search for the optimal overall solution). These variables will then flow (in its majority) into the problem's mission points calculation.

4.1.2 Mission Points

Mission points portion of the framework starts by receiving the problem variables and transforming these into fluid related variables. Figure B.2 illustrates this flow.

Complementary to this, the wing aero-structural geometry properties are defined as well as their meshes (Fig. B.3 (a)) and the take-off is calculated following the methodology described in Subsec. 3.3.5 (Fig. B.3 (b)). Notice that it is only on this stage that the wing's aero-structural variables appear

defined in the wing module.

The following modules will be responsible for the aero-structural performance calculations along with the propulsion system evaluation and the point performance calculations that ultimately reach the equilibrium equations calculations (Moments and Forces) - Fig. B.4.

Notice that the framework does not calculate the collocation points in a vectorized form, instead all points are calculated separately, here represented simplified by a 5 point system with the first point exploded for additional information. Also, although wing definition is made outside the mission points (its a fixed geometry in each stage), the tail mesh definition is produced inside each mission point. This detail is important to guarantee trim condition as explained further in this thesis.

Aero-Structural Coupling

First, the aero-structural coupling must be defined in order to better understand the framework processing.

The aero-structural analysis uses the models described in Sec. 2.2 and 2.3 which coupled in a way that only converged aero-structural solutions pass through the optimization cycle. At start, the surface's defined mesh (wing or tail) is used to determine the aerodynamic loads through its structural points. Afterwards, these loads are placed inside the structural calculation method and a new deformed mesh is formed. This deformed mesh is then passed to the aerodynamic analysis, which in turn produces new loads for the structural system. This iterative aero-structural cycle stops once the aerodynamic loads produce an equivalent mesh, within certain convergence criteria. This cycle and be observe in Fig. B.5 in a simplified manner.

Propulsion Coupling

For the propulsive system (Fig. B.6), a thrust calculation is processed in each mission point so the performance can be calculated. In this framework, as explained in Sec. 3.2, the user can opt from two different models.

If the propulsive model is chosen to be the simple one with constant power available, only the power and thrust are calculated. if the model chosen is the battery model with power decay, then between each mission point a wasted energy variable must be passed through. This energy decay starts with the take-off model where the initial wasted capacity is calculated. Afterwards, each mission point calculates the point wasted capacity and sums to the initial capacity available. The wasted capacity in each point is then transmitted as initial capacity to the next mission point.

Mission Point Performance

Finally, in each mission point, a point performance is achieved by calculating the important metrics (Fig. B.7).

This module is responsible for the calculation of the equilibrium functions (*forces_eom* and *moment*) as well as the Cg location calculation. The forces calculated in *forces_eom* will be important for the

collocation method defects calculation and to assure the physically possible behaviour of the aircraft, since it calculates the sum of forces in the horizontal and vertical directions. The *moment* segment is important to assure the aircraft is in static equilibrium in each point by assuring (as mentioned in Subsec. 3.3.4) a null pitching moment. This is only possible by allowing the tail mesh definition to be inside each mission point, where the angle of incidence of the tail can be changed so the necessary equilibrium of the aircraft can be achieved.

4.1.3 Mission Performance and Constraints

The last segment of the framework is responsible for the calculation of the necessary metrics to evaluate the aicraft performance. Figure B.8 presents the modules in this segment.

Modules described in *mission_perf* describe mission related evaluation performance. The most relevant in this work are the *mission_score* (more explicitly presented in Sec. 5.1.1) and *collocation*. In the last one, the collocation method is implemented as described in Sec. 2.5. The other modules in this part either create auxiliary variables for the aforementioned modules or create constraint variables to simulate the problem at hand.

Modules described in *constraints_perf* represent specific aircraft constraints, such as geometry, trajectory requirements and flight continuity.

4.1.4 Final Remark

Lastly, it is worth mentioning that the framework, as an optimization method, cycles through these modules in a cyclic manner. *OpenAeroStruct* uses as base the *OpenMDAO* optimizer which has included a total of fourteen different optimizers choices. These include stochastic and gradient methods. These will evaluate each cycle results and depending on each method algorithm, will produce, at each cycle, new set of design variables until eventually optimal solution convergence is achieved.

The overall optimization scheme is presented in Fig. 4.2 where a XDSM [22] diagram is depicted describing the whole framework.
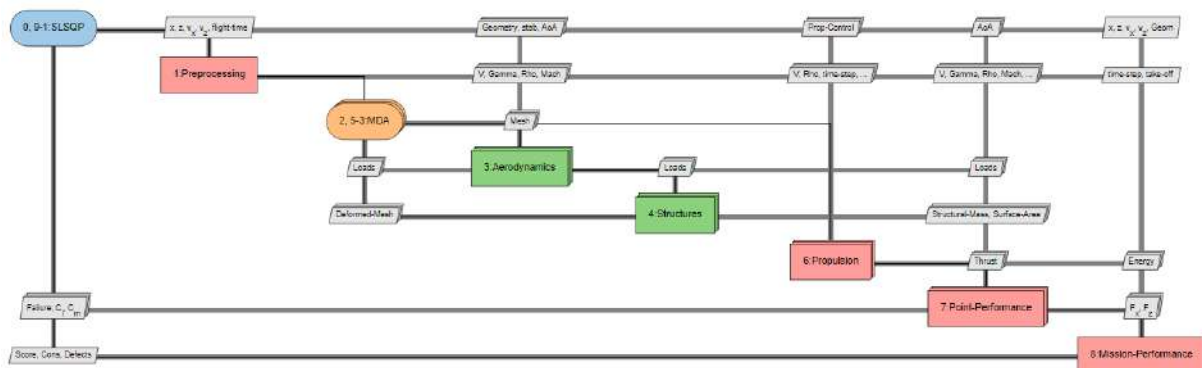
Figure 4.2: XDSM diagram for the created framework. Created with [56]

45

4.2 Framework Parameters

This section is reserved for the solver and optimizer definitions and the framework's mesh and control points parameters. A brief geometric and trajectory mesh study is presented where the number of panels in each surface and the number of trajectory control points are studied.

4.2.1 Solver and Optimizer Parameters

The MDA employed in this work uses a NLBGS with Aitken's relaxation method [57] to solve the aero-structural coupling. As for the optimizer, the SLSQP (sequential least squares programming) method [58] was used since it is a gradient based method and it is was the only optimizer able to reliably converge for the problem at hand. Table 4.1 comprises the solver and optimizer tolerances used for this framework. The solver tolerances were chosen based on the recommended parameters defined by *OpenAeroStruct*. The optimizer tolerance was chosen to achieve converged solutions without the requirement of extensive optimization computational times.

Table 4.1: Gauss-Seidel solver and SLSQP optimizer tolerances.

Parameter	Value
Solver absolute error tolerance	10^{-7}
Solver relative error tolerance	10^{-30}
Optimizer tolerance	10^{-2}

4.2.2 Mesh Study

One important aspect of optimization is to assure the models used are converged. This assures that that the solution is in fact a converged solution where the results from the aerodynamic and structural model are as close to reality as they can be. Not assuring convergence to these models can produce unrealistic results.

To assure the best results possible, a mesh convergence study was conducted. The aerodynamic surfaces' panels as well as the beam elements depend on two variables: num_x and num_y. The first corresponds to the number of chordwise panels on the surface, while the latter defines the spanwise panels. Figure 4.3 presents a wing and tail modelled through these panels.

The problem here studied is the same presented further in Chap. 5 where a feasible aircraft geometry was evaluated.

The higher the number of panels, the most accurate the solution is, but the higher is the computational cost as well. Thus, this mesh convergence study aims to find the most accurate solution with affordable computational cost.

Finally, the last important aspect of the mesh convergence is the convergence criteria and metric. For this study, the drag coefficient (C_D) of the wing and tail in one analysis is used. For the convergence criteria, a formulation was formed as
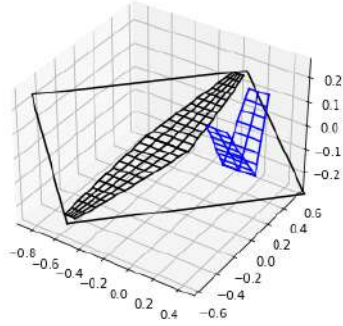
Figure 4.3: Framework mesh example for both wing and tail.

$$C_{criteria} = \frac{|C_{D_x} - C_{D_1}| - |C_{D_{converged}} - C_{D_1}|}{|C_{D_{converged}} - C_{D_1}|} \times 100\% \quad , \qquad (4.1)$$

where C_{D_x}, C_{D_1} and $C_{D_{converged}}$ represent the C_D for a given num_y in a fixed num_x environment, the first C_D value for a given fixed num_x and a initial num_y and the most converged C_D value, respectively. For this study a $C_{criteria}$ value of less than 3% was considered enough to define convergence. The mesh convergence study is presented in Fig. 4.4 and Tab. 4.2.
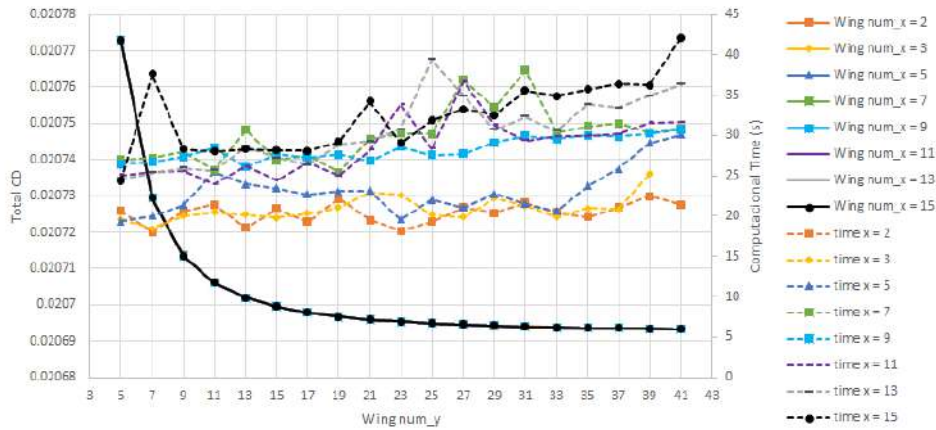
(a) Mesh convergence study.
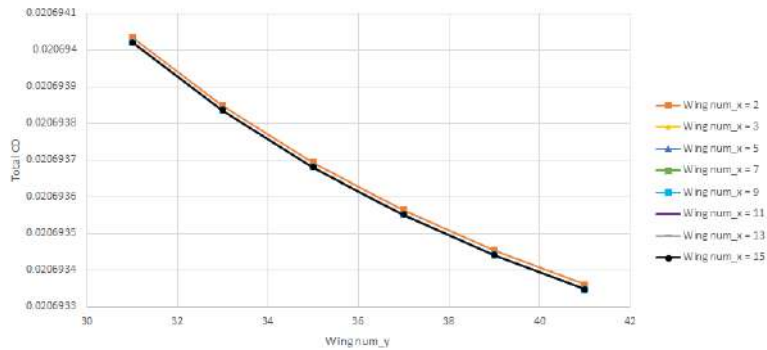
(b) Detailed mesh convergence portion.

Figure 4.4: Mesh convergence study graphical results in full spectrum and detailed.

Starting with the graphical results, it is clear that the most significant parameter for convergence is

Table 4.2: Mesh convergence results using the $C_{criteria}$ metric.

num y	num x							
	2	3	5	7	9	11	13	15
5	-	-	-	-	-	-	-	-
7	45.36	45.34	45.34	45.34	45.34	45.34	45.34	45.34
9	25.48	25.46	25.46	25.46	25.46	25.46	25.46	25.46
11	16.08	16.06	16.06	16.06	16.06	16.06	16.06	16.06
13	10.90	10.89	10.89	10.89	10.89	10.89	10.89	10.89
15	7.76	7.74	7.74	7.74	7.74	7.74	7.74	7.74
17	5.71	5.69	5.69	5.69	5.69	5.69	5.69	5.69
19	4.29	4.27	4.27	4.27	4.27	4.27	4.27	4.27
21	3.28	3.26	3.26	3.26	3.26	3.26	3.26	3.26
23	2.53	2.51	**2.51**	2.51	2.51	2.51	2.51	2.51
25	1.95	1.94	1.94	1.94	1.94	1.94	1.94	1.94
27	1.51	1.49	1.49	1.49	1.49	1.49	1.49	1.49
29	1.15	1.13	1.13	1.13	1.13	1.13	1.13	1.13
31	0.86	0.85	0.85	0.85	0.85	0.85	0.85	0.85
33	0.63	0.61	0.61	0.61	0.61	0.61	0.61	0.61
35	0.44	0.42	0.42	0.42	0.42	0.42	0.42	0.42
37	0.27	0.26	0.26	0.26	0.26	0.26	0.26	0.26
39	0.13	0.12	0.12	0.12	0.12	0.12	0.12	0.12
41	0.02	0.00	0.00	0.00	0.00	0.00	0.00	0.00

the num_y variable, while the variable num_x produces almost no change in C_D on its own. Furthermore, the computational time increases with the number of added panels.

Figure 4.4 (b) gives additional insight for this convergence study. As it can be observed, all lines (corresponding to different num_x fixed values) are very close to each other, implying that for convergence the utmost important value is num_y.

Analysing now the data in Tab. 4.2, it is clear that the convergence is gradually achieved as more panels in the spanwise direction are added. The convergence criteria is achieved for a number of spanwise panels of 23 for all num_x curves.

Following the wing mesh study results, the number of panels defined for the wing was $num_y = 23$ and $num_x = 5$, since this combination is proven converged and does not require too much computational cost.

As for the tail, since it is smaller, a mesh with $num_y = 15$ and $num_x = 3$ was used, which creates similar sized panel.

4.2.3 Control Points Study

Since the trajectory is defined by control points where the collocation method is applied, it is important to assure the number of control points that allows for the best result while maintaining low computational cost.

Similarly to the mesh convergence study, the control point study also used a metric and a convergence criteria. For the convergence criteria, a graphical observation was used. As for the metric, the final objective function - score - was used. Notice that the metric used is the optimization objective function (score) and thus the convergence should be carefully analysed. As the number of control points

increases, the odds of finding local minima increases. However, using few control points produce a low resolution trajectory and thus worse results.

Figure 4.5 presents the results for the study conducted. The problem here studied is the same presented further in Chap. 5 where a generic feasible aircraft geometry and trajectory was chosen as initial solution. This plot also presents the computational effort for each optimization conducted. As expected, the computational effort exponentially increases with the number of control points. Also, the score metric starts at a poorly value but rapidly stabilizes around 2000. It is worth mentioning that these computational times are not fixed for the number of control points but rather for the initial solution given to the optimizer. However, the gradually increasing computational demand is representative of the control points influence.
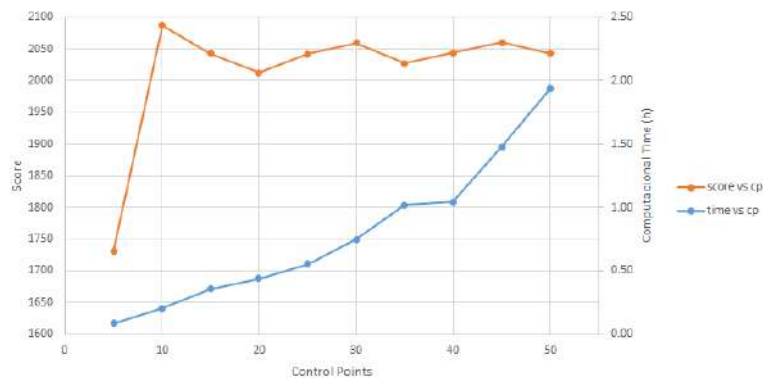
Figure 4.5: Control points convergence study graphical results.

With the results presented together with an effort to avoid high computational costs, a trajectory with 30 control points was used throughout this work.

4.3   Framework Verification

Since the purpose of this thesis is to explore the results achieved and not extensively explore the verification requirements, the verification is here simplified by examples that should be seen as generic observations of the framework. Hence, if a constraint verification is presented and assured, these should be considered transversal for the framework response and, thus, all constraints should be considered verified using the same formulated method.

To better understand and visualize the framework optimization results, a few graphical representations were made: wing and tail planform inside the rhombus box, design variables history, constraint functions history, objective function history and trajectory.

The first one presents the wing and tail mesh inside the rhombus box, which allows not only to visually verify the rhombus box constraint, but also see each iteration result. Figure 4.6 presents a preview of this result for a generic optimization cycle.

Design variable, constraint function and objective function histories simply show their value for each iteration, enabling an optimization history analysis. Such results are described further in the following

49

(a) First optimization cycle iteration aircraft planform. (b) Last optimization cycle iteration aircraft planform.
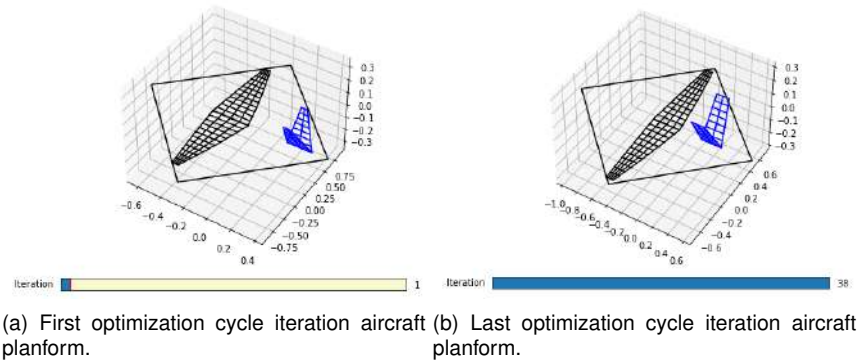
Figure 4.6: Aircraft planform inside rhombus box examples for a generic optimization.

subsections.

Finally, trajectory results preview the aircraft progression through space, where it can be clearly seen the optimization's path choice. These will also be explored further next.

Verification for this framework comprises three important aspects: Boundary compliance, Constraint compliance and Trajectory accordance. First, the typical results presented are enunciated.

4.3.1 Boundary Compliance

Boundary compliance concerns the design variables' boundaries established in the framework. Each design variable is defined within a possible search space, which helps define the problem and limit the variables to a controllable expected range. It is important that these boundaries are active and, thus, not allow for any variable to be out of its encapsulating box. As an example, the wing and tail spans are in Fig. 4.7 in a generic optimization routine.

(a) Wing span. (b) Tail span.
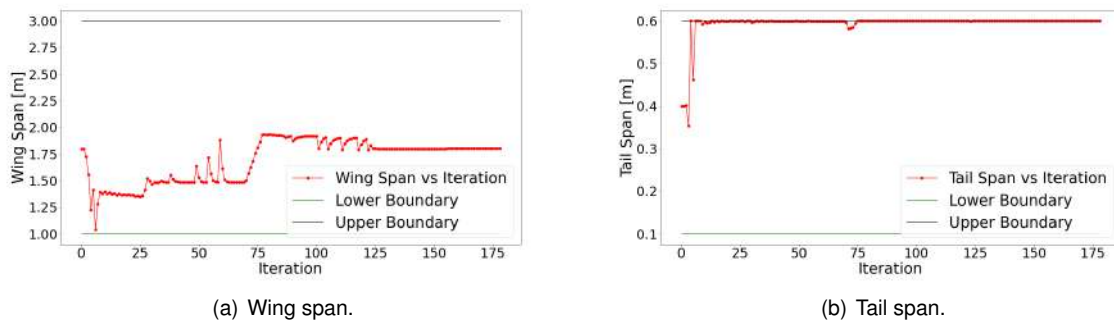
Figure 4.7: Wing and tail span history through the optimization routine.

As it can be seen, both variables respect its bounded conditions. Furthermore, in the tail span example the boundary can be seen active and thus functional.

4.3.2 Constraint Compliance

Constraint compliance concerns the constraint functions values and if they respect its bounded values and conditions.

For the framework to work properly, the constraints, depending on their type, must be bounded to their region. Otherwise, the solution would not respect at least one constraint condition and the result would be invalid. As an example the rhombus fit constraint variables are presented in Fig. 4.8 for a generic optimization routine.
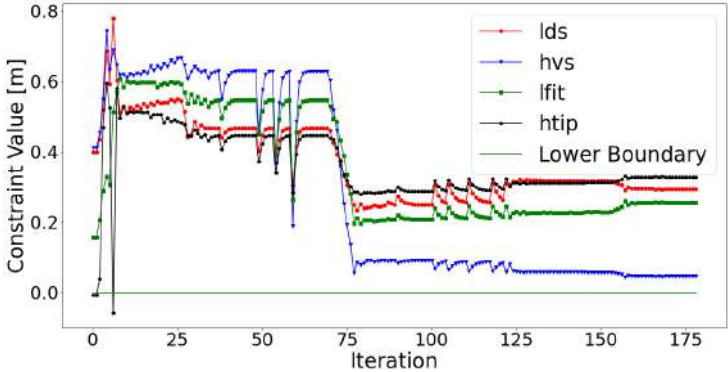
Figure 4.8: Rhombus box fit constraint variables value through the optimization iterations.

It can be seen two important aspects from this example. The first is the frameworks' capability to comply with the bounded region by correcting a constraint function value from off-boundaries to a bounded state. Additionally, the optimizer correctly searches through the available design space and stabilizes near the end of the optimization.

4.3.3   Trajectory Accordance

Trajectory accordance concerns the trajectory choices of the framework, which should be physically possible and within normal operation conditions. For this, the defects (see Sec. 2.5) shall be analysed and they should be bounded close to zero so all the control and state variables respect their physical interactions. Fig 4.9 presents the defects value for a generic optimization routine.
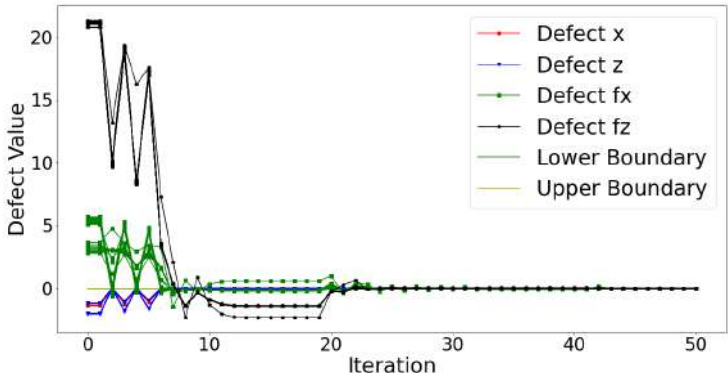
Figure 4.9: Defects values through the optimization iterations.

As shown, the defects start with values far from zero and through iterations converge to a zero value (within the tolerances defined). This indicates that the optimization started with an unfeasible trajectory and found a stabilized physically possible trajectory.

Chapter 5

MDO Setup and Results

This chapter is reserved for the results achieved with the developed framework. It comprises five sections: Mission, Base solutions, Coupled design and trajectory optimization, B-spline interpolation and Thrust model comparison. The first describes the problem formulation taking into account the mission goals and the constraints acting on the system. The second section comprises a direct approach of the framework built for the three score independent cases of the competition - payload, climb and distance. The third delivers an in-depth analysis of the pursuit of the optimal conceptual design. Finally, the last two sections analyse the influence of the b-spline method implemented and the comparison of the propulsion models.

5.1 Air Cargo Challenge 2022 - Mission

5.1.1 Mission Objectives

This event is a three category score based competition based in three distinct flight segments: take-off, climb and cruise [16].

In the Take-off the purpose is to carry as many payload bags as possible. The score function for this segment is

$$S_{payload} = 1000\frac{P_{team}}{P_{max}} \quad , \quad (5.1)$$

where P_{team} and P_{max} represent the payload of the team and the maximum payload achieved overall in the competition, respectively. Additionally, take-off must be achieved in less than 60 meters, with a 10% bonus reward for the total score of the team if accomplished in less than 40 meters.

The climb segment is characterized by the altitude achieved in 60 seconds. The score function is

$$S_{climb} = 1000\frac{PS_{altitude,team}}{PS_{altitude,max}} \quad , \quad (5.2)$$

where $PS_{altitude,team}$ and $PS_{altitude,max}$ represent the pre-score altitude of the team and the maximum pre-score altitude achieved overall in the competition, respectively. The pre-score altitude is

$$PS_{altitude} = -3.92e^{-5}h_{60s}^4 + 1.08e^{-2}h_{60s}^3 - 1.156h_{60s}^2 + 64.2h_{60s} - 537 \quad , \tag{5.3}$$

where h_{60s} is the altitude achieved in 60 seconds of climb. This function can be visualized in Fig 5.1.
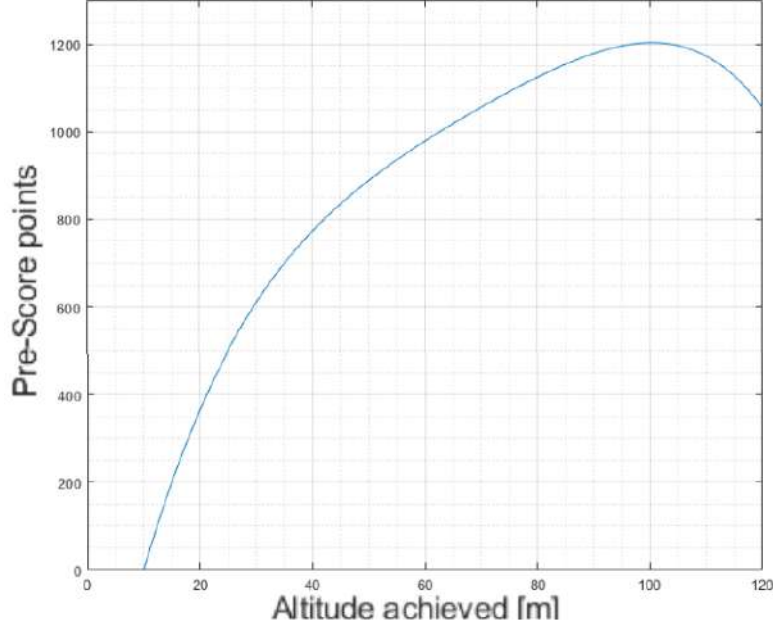
Figure 5.1: Pre-score Altitude graphical visualization [16].

The final flight segment is the cruise which may involve turns with long radius (50-100 meter radius). The score for this flight condition is

$$S_{distance} = 1000\frac{D_{team}}{D_{max}} \quad , \tag{5.4}$$

where D_{team} and D_{max} represent the distance travelled by the team and the maximum distance achieved overall in the competition, respectively. This is evaluated by the maximum distance travelled in 120 seconds.

The final score used for this thesis is

$$S_{total} = (S_{distance} + S_{climb} + S_{payload}) \times (1 + P_{to\_bonus}) \quad , \tag{5.5}$$

where P_{to_bonus} represents the take-off bonus and can assume either the value of 0 or 0.1 depending on the take-off distance (0.1 for a runway equal or less than 40m).

It is important to note that these scores are dependent in the behaviour of the best team in each segment, which causes difficulties in the problem definition. The best team will be the one that measures the importance of each segment and designs an aircraft that outperforms every team. This process is described in 5.2.

5.1.2 Mission Constraints

This event also sets baseline constraints for all participating teams to assure a fair competition. These include an electric motor, propeller limitations and geometry related regulations [16]. Here these constraints are described and the set of baseline mission constraints will be set.

Propulsion Constraint

The electric motor and propeller define the propulsion system and the thrust produced by these is only dependent on the battery used to power this system. The propulsive model is described in Sec. 2.4 and delivers the thrust produced by the motor given the propulsion control variable δ_t. With this model, the optimizer must only guarantee the aircraft has enough energy for the propulsion needs.

Consequently, the propulsion constraints deal around the energy and capacity of the battery (in case of the battery model). To simplify, the propulsion constraints that will be presented respect to the battery simulation model. The simpler propulsion model respects all constraints expect the ones related to capacity, which it does not need.

To relate battery mass and energy available with spent energy, the first propulsion constraint is described as

$$E_{max} = W_b \times e \times ue > E_{wasted} \quad , \tag{5.6}$$

where E_{max}, W_b, e, ue and E_{wasted} are the maximum available energy, battery weight, battery specific energy, possible usable energy and wasted energy, respectively.

As for the battery capacity, the next propulsion constraint states

$$C_{max} = C_b \times ue > C_{wasted} \quad , \tag{5.7}$$

where C_{max}, C_b and C_{wasted} are the maximum capacity, design battery capacity and wasted capacity, respectively.

Finally, the last constraint connects the batteries available energy with its capacity, as

$$-1e^{-2} > C_b - W_b \times e > 1e^{-2} \quad . \tag{5.8}$$

Note that in the last constraint, a bounded inequality was used instead of an equality constraint, to assure better convergence for the optimizer without negatively affecting the results. This is a common optimization workaround and was used throughout the constraints formulation to avoid equality constraint induced convergence problems.

Geometry Constraints

The competition severely constraints the geometry through mainly the rhombus box fitting regulations. Additionally some dimensions are constrained by the transport box, however those can be

constraint from the design variables' bounding limits.

The first constraint describes the wing to tail mesh formulations. *OpenAeroStruct* allows for the creation of both wing and horizontal tail lifting surfaces meshes and the initial distance between them. However, that distance must be corrected for the proper functioning of the framework, since the wing to tail distance can define if the aircraft respects the rhombus box dimensions or not.

For this matter, the constraint connects the mesh distance to the l_t design variable as

$$-1e^{-3} > |mesh_{wing}(x_0) - mesh_{tail}(x_0)| - l_t > 1e^{-3} \tag{5.9}$$

Now, the geometry constraints can be set in relation to l_t which will directly affect the mesh disposition. To assure the rhombus box geometry constraint is complied following Subsec. 3.3.3, the framework is set to respect the geometry inequality constraints as

$$l_{ds} > 0 \tag{5.10}$$

$$h_{vs} > 0 \tag{5.11}$$

$$l_{fit} > 0 \tag{5.12}$$

$$h_{tip} > 0 \tag{5.13}$$

Trim and Stability Constraints

These constraints assure the aircraft optimized solution is a good stable design. For this, two restrictions are made, one in every collocation point written as

$$C_{m_i} = 0 \quad \text{, with } i = 1...n_{points} \tag{5.14}$$

which implies the aircraft is trimmed in its position with the help of the stabilizers, and one geometric constraint to assure the vertical stabilizer volume component of the "V" tail is between historical values, as

$$0.04 > V_{VT} > 0.09 \quad . \tag{5.15}$$

Structural Constraints

Structural constraints are represented by a failure restriction where the aircraft wing and tail structure must not fail due to the aerodynamic loads they are subjected. This is done through the use of the KS (Kreisselmeier and Steinhauser 1979) function that aggregates all failure constraint (vectorized form) of a specific surface into a single constraint value which greatly enhances the optimizer efficiency while maintaining a good structural evaluation of the surface's structure. These are represented by a negative value (from 0 to -1) if the structural integrity is secured and a positive value if structural failure is found. This way, both wing and tail constraints are set as

$$KS_{failure_{w/t}} < 0 \tag{5.16}$$

Additionally, for the structural framework to work successfully, spar material properties must be defined. For both wing (wing box section) and tail (tubular section), the carbon fiber laminate material was chosen - a typical material used in the competition to create almost any structural component. The properties are the presented in Tab. 5.1.

Table 5.1: Carbon laminate properties [59].

Young modulus	Shear modulus	Yield stress	Density
$E = 70 \quad GPa$	$G = 5 \quad GPa$	$\sigma_y = 600 \quad MPa$	$\rho = 1400 \quad kg/m^3$

Aerodynamic Constraints

Aerodynamic constraints are related to the aerodynamic performance of both tail and wing. The framework, if allowed, might produce unrealistic lift coefficient distributions of C_l. For this matter, a limitation must be imposed to obtain an applicable solution based on the optimized 2D airfoil produced by the team.

Through XFLR5 [54], a maximum C_l can be estimated for both wing and tail airfoils. First, the fluid regime must be determined. For the typical values of the aircraft's flight, the speed of the aircraft is around 18 m/s and, with a standard sea-level air properties, the Reynolds number can be estimated as

$$Re = \frac{\rho v c_w}{\mu} \approx 3.5 \times 10^5 \quad . \tag{5.17}$$

The XFLR5 results are shown in Fig. 5.2.

(a) Wing airfoil analysis - Olissipo Air Team optimized airfoil.

(b) Tail airfoil analysis - NACA 0009
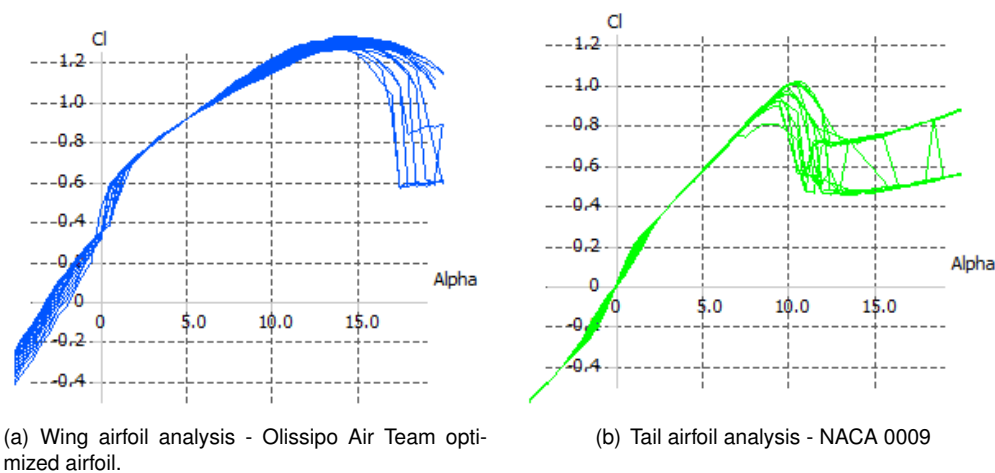
Figure 5.2: XFLR5 C_l-α analyses for the wing and tail airfoils

Through observation of Fig. 5.2, the maximum values can be determined, leading to the aerodynamic constraints

$$C_{l_w} < 1.3 \tag{5.18}$$

$$C_{l_t} < 0.95 \tag{5.19}$$

Trajectory Constraints

Trajectory on the framework needs to be constrained for two main reasons. One is aligned with flight continuity - take-off calculations are made outside of the mission points calculations. As opposed to climb and cruise continuity, where both are part of the same calculations and therefore are only sub-parts of a flight segment, take-off is calculated as a another flight segment. The other reason is to make the optimizer more aligned with the optimization's objective.

For the first reason, the velocity in the longitudinal axis of the aircraft must coincide. This is implemented as

$$- 1e^{-2} > \dot{x}_{to} - \dot{x}_i > 1e^{-2} \quad . \tag{5.20}$$

where $\dot{x}_{to}$ and $\dot{x}_i$ are the final take-off speed and the initial flight speed, respectively.

For the second reason, a climb helping mechanism is implemented where the maximum possible achievable altitude is the one registered in the 60s mark after take-off (z_{60s}). This also allows for the aircraft to cruise with a negative pitch angle, which results in a better use of the aircraft's weight contribution to the velocity. This constraint is implemented on the vertical component of the aircraft position,

$$z <= z_{60s} \quad . \tag{5.21}$$

Additionally, to comply with the flight ceiling of the competition, according to the European regulations for flying,

$$z <= 120m \quad . \tag{5.22}$$

Finally, to assure the good functioning of the collocation method (Sec. 2.5), the defects are bounded close to a null value,

$$-1e^{-4} < \zeta_x < 1e^{-4} \tag{5.23}$$

$$-1e^{-4} < \zeta_z < 1e^{-4} \tag{5.24}$$

$$-1e^{-4} < \zeta_{fx} < 1e^{-4} \tag{5.25}$$

$$-1e^{-4} < \zeta_{fz} < 1e^{-4} \tag{5.26}$$

$$\tag{5.27}$$

These last two constraints will assure that the optimal trajectory is physically realistic.

Payload Constraints

To comply with the requirements set by the competition, the payload must not interfere with the CG location of the aircraft, thus it does not change the longitudinal stability regardless of the payload choice. The framework handles this problem by limiting the position of the payload. Since the regulation only implies the CG position in the longitudinal x-axis, the formulation implemented states

$$- 1e-2 < CG_x - CG_{Payload_x} < 1e-2 \quad . \tag{5.28}$$

5.1.3 Problem Formulation

Having presented all design variables and constraints, the problem formulation may be stated. Through the search for the optimal solution for this thesis problem, there are three objective functions analysed - one for each score segment - payload, climb, distance and total scores. Since the framework is pre-defined for minimization and the purpose of this work is to maximize a score value, it was defined to use the inverse of the score function, converting a maximum optimization to a minimum optimization with the same results. The objective function, in this work called generically by *F(x)*, is based on the design variables *x* and is formulated as:

$$F(x) = \frac{1}{S_{paylaod}} \quad \text{, for payload optimization} \tag{5.29a}$$

$$F(x) = \frac{1}{S_{climb}} \quad \text{, for climb optimization} \tag{5.29b}$$

$$F(x) = \frac{1}{S_{distance}} \quad \text{, for distance optimization} \tag{5.29c}$$

$$F(x) = \frac{1}{S_{total}} \quad \text{, for global optimization} \tag{5.29d}$$

Assuming, generically again, the aforementioned constraint functions as $C(x)$ and the design variables described in Tab. A.2 as x, the optimization can now be completely established and formulated as

$$
\begin{aligned}
\text{Minimize} \quad & F(x) \\
\text{w.r.t.} \quad & x \\
\text{subject to} \quad & C(x) \, .
\end{aligned}
\tag{5.30}
$$

To conclude, it is important to evaluate the dimension of the problem formulated. Table 5.2 comprises information about the optimization problem dimension.

Table 5.2: Optimization problem size.

Design Variables	Constraint Functions
$6 \times n + 26$	$9 \times n + 13$

Here n represents the number of control points. As seen, there are a fixed number of design variables and constraint functions and a variable number as well. The problem's dimension is very dependent on the number of control point and consequently the time efficiency is also very dependent. Following the results presented in Subsec. 4.2.3, the number of control points chosen for this work is 30, which produces a total of 206 design variables and 283 constraint functions. Note that each collocation point is a set of 4 state variables and 2 control variables. In a similar manner, each collocation point comprises 4 constraint functions for the trajectory and several other to limit some metrics (stability, C_l) in each flight stage.

This overall optimization size reveals the complexity of a simplified problem and the power of these optimization methods that can optimize this size related problems in a few hours.

With the problem now completely formulated, the search for the optimal solution can now begin. The following sections will describe the procedures followed in this pursuit.

5.2 Air Cargo Challenge 2022 Competition Base Solutions

Following the problem formulation, the framework was used to determine, at first, the best conceptual design tendencies for each of the score parts: Payload, Climb and Distance, using the framework objective function defined as the inverse (for minimization) of Eqs. 5.1, 5.2 and 5.4, respectively. Climb and distance optimizations are expected to reduce payload and aircraft's weight, while the payload optimization should do the opposite.

Before analysing the results, the initial design point was defined with the initial flight profile presented in Fig. 5.3 and aircraft geometry Fig. 5.4, where the wing and tail planform is presented accompanied by the rhombus box limitations. The initial results and parameters can be seen in Tab. C.1.

(a) Aircraft's x displacement through time.   (b) Aircraft's z displacement through time.
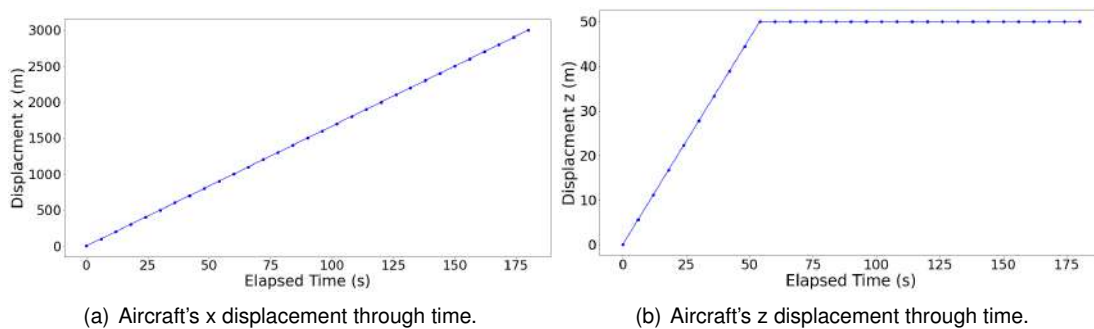
Figure 5.3: Initial trajectory given for the optimizations.

The initial flight profile was intended to be sub-optimal in climb and distance to promote the framework to search for the optimal solution. The initial aircraft geometry and properties were also defined sub-optimal to allow not only for freedom in the optimization but also to verify if the optimizer correctly searches the design space.

The results will now be presented in sequential form where each part is analysed in detail.
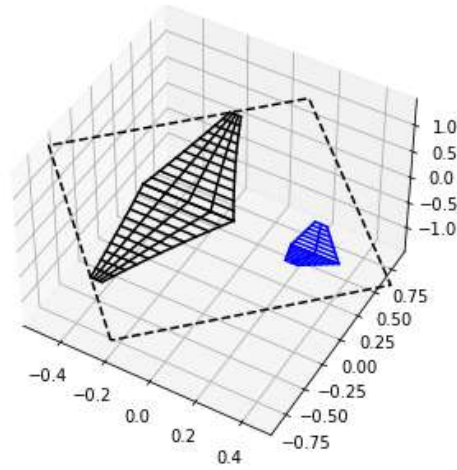
Figure 5.4: Aircraft initial configuration.

5.2.1 Climb

The climb segment is characterized by the first 60 seconds of the flight where the altitude of the aircraft shall reach 100m for maximum points. It is expected that the optimizer reduces the aircraft weight by minimizing the payload and choosing the best suited trajectory to enhance the climb points. The optimization results (trajectory and planform) are presented in Figs. 5.5 and 5.6.

(a) Aircraft's x displacement.

(b) Aircraft's z displacement.

(c) Aircraft's velocity in x axis.

(d) Aircraft's velocity in z axis.
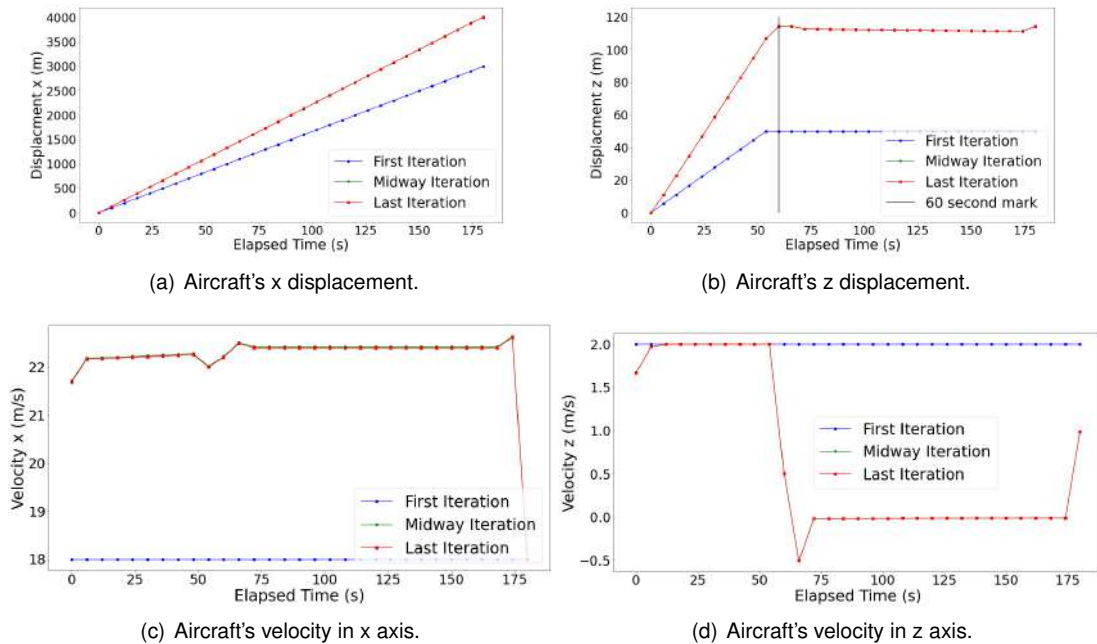
Figure 5.5: Trajectory results for climb optimization.

As expected, the optimized configuration is a light weight (1.3kg compared to the usual 2kg) solution where the trajectory chosen clearly optimizes the climb achieved at the 60 seconds mark. It is important to note that this result is improved by the use of the altitude constraint implemented. Furthermore, the result observed is not the optimal climb solution - the best is 100m. However, the optimization's search
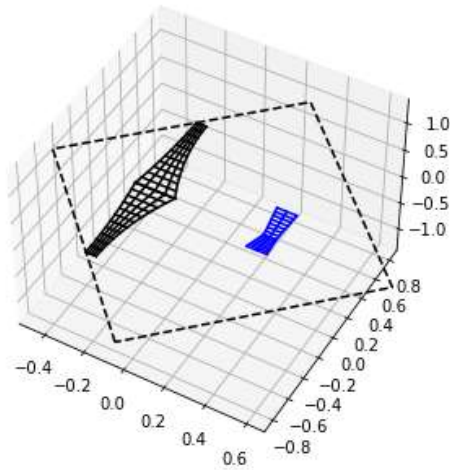
Figure 5.6: Aircraft climb optimized planform.

path is in correlation with the ultimate purpose of this single objective formulation. A more deep search could be sought for to achieve the global optimum but that study is not relevant for the climb alone.

Additionally, it can be observed that the distance travelled (4000m compared to the initial 3000m) for this solution is also high, which correlates well with the light weight option for the system.

5.2.2 Distance

For the distance results, the optimizer is expected to reduce the aircraft's weight and choose a straightforward trajectory to optimize its distance. Since acceleration is very dependent on the aircraft's mass, the wing should be defined to be only sufficient to keep the aircraft flying. Following the same methodology as before, the results are presented in Figs. 5.7 and 5.8.

In this scenario, the framework correctly identified the optimal goal to increase the velocity in the longitudinal axis to increase the maximum. It is important to note that in this optimization the altitude constraint to improve climb results was disconnected to allow a better verification of the optimization search decisions.

Notice that the configuration achieved is very similar to the one achieved through optimizing the climb, which is expected since both require a light weight aircraft but with different trajectory choices.

It was also expected for the thrust of the aircraft to be capped at full throttle, since this would optimize the force in the aircraft's longitudinal axis. However this was not the case. Figure 5.9 shows the thrust results for this configuration. It seems to indicate a sub-optimal choice for the thrust results. However, there are other factors that play a role in this problem. Higher thrust will imply higher Lift that ultimately changes the aircraft's trim condition, thus leading to a higher elevation, which is not permitted by the maximum altitude constraint. This can be analysed by assuming different initial empty weight CG assumptions but for this validation analysis, the scope does not include this approach.
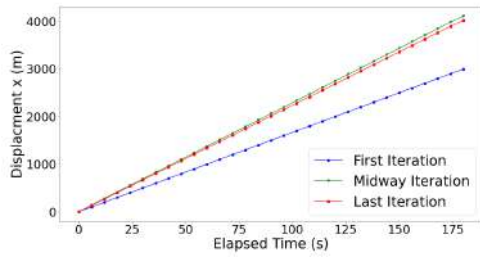
(a) Aircraft's x displacement.
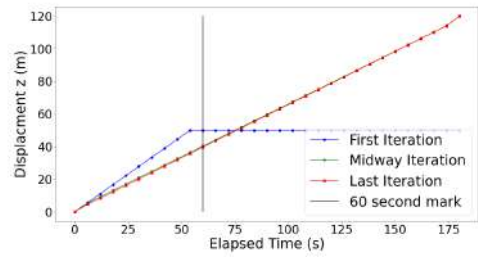
(b) Aircraft's z displacement.
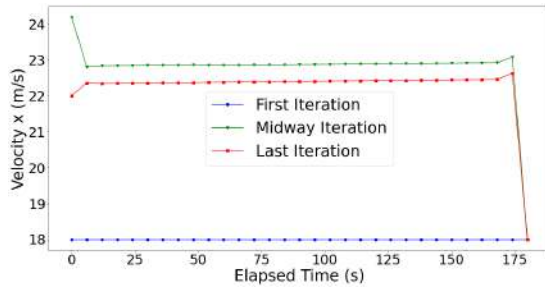
(c) Aircraft's velocity in x axis.
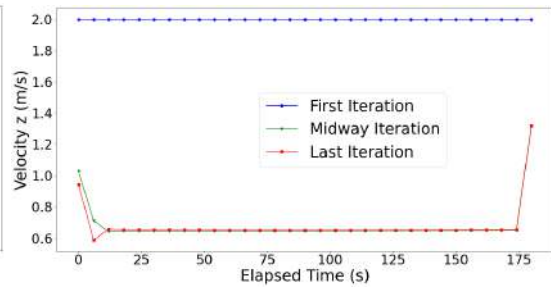
(d) Aircraft's velocity in z axis.

Figure 5.7: Trajectory results for distance optimization.
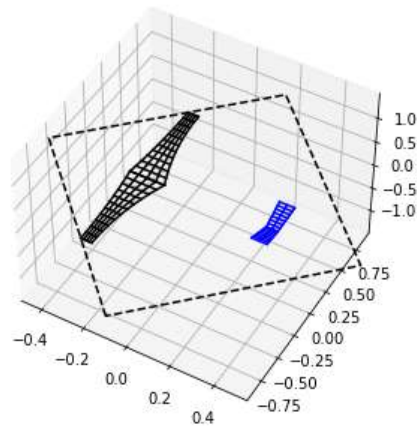
Figure 5.8: Aircraft distance optimized planform.
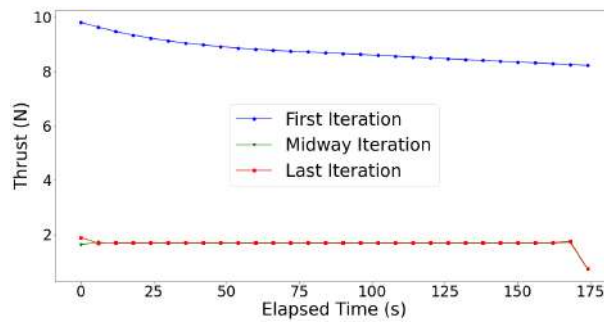
Figure 5.9: Aircraft thrust.

5.2.3 Payload

For the payload part, contrasting with the previous optimizations, the purpose is to carry as much cargo as possible, meaning the wing surface area should be maximized and a low speed should also be chosen since the distance travelled is not considered for the objective function. The results are presented in Figs. 5.10 and 5.11.

(a) Aircraft's x displacement.

(b) Aircraft's z displacement.

(c) Aircraft's velocity in x axis.

(d) Aircraft's velocity in z axis.
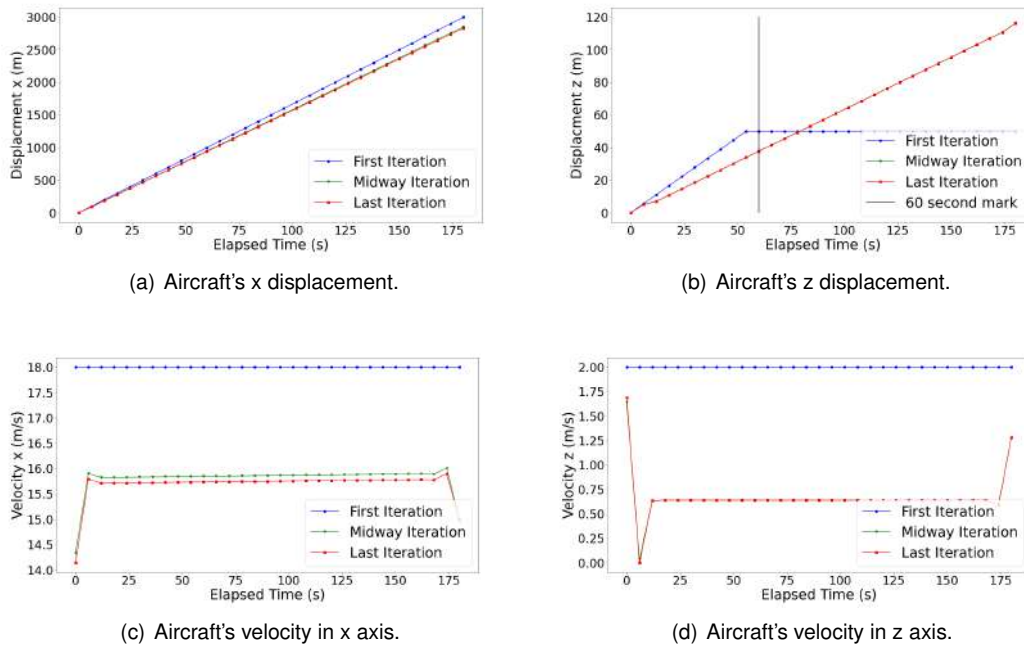
Figure 5.10: Trajectory results for payload optimization.
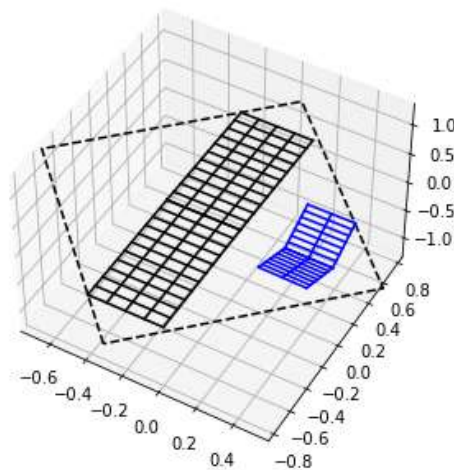
Figure 5.11: Aircraft payload optimization planform.

In this optimization, the framework sought, as expected, a higher surface area wing ($0.72m^2$ compared to the initial $0.39m^2$) to maximize its lift and a loss in speed. As the distance optimization, the altitude improving constraint was not used to validate the framework's decisions.

5.2.4 Final Remarks

As a final note, it was clearly shown that the optimizer search for the optimal solutions in each case were expected results, which validates its final purpose - to optimize all score parts together.

The results from the previous optimizations are presented in Tab. 5.3.

Table 5.3: Score points for each optimization.

	Climb Score	Distance Score	Payload Score	Total Score
Climb Optimization	943.60	929.36	83.33	2151.92
Distance Optimization	638.79	930.12	0	1725.80
Payload Optimization	615.49	656.30	750	2223.97

Notice that the highest score total configuration is the payload one although its poor speed and climb results. This happens due to the payload effect on the score. While no payload leads to no score points in the payload segment, a heavier slower aircraft still earns a good amount of score points in both climb and distance parts. This is the ultimate purpose of this thesis - to find the optimum conceptual decision that takes into consideration all three parts.

5.3 Coupled Design and Trajectory Optimization

The goal of the framework is to lead to the optimal conceptual design for the ACC's 2022 competition. To achieve this, one must define the metrics and goals in terms of general wing geometry properties and trajectory preferences. The results will be analysed in respect to the wing's span, chord and area, trajectory's choice in each flight segment, and general aircraft needs - structural weight and energy.

The method proposed in this thesis is the analysis of three independent cases where different starting design points are chosen. The score progression and what the optimizer tends to normally develop into will be analysed.

5.3.1 Case Study #1

For the first case, the same initial configuration as the previous individual segment studies is used as a mean to couple together the best aspects in each optimization.

Figure 5.12 previews the initial and final configuration and the score progression, while Fig. 5.13 shows the optimizer's trajectory choice.

The optimizer successfully maximized the aircraft score by manipulating the wing geometry, to produce higher wing loads, and the trajectory by increasing the altitude in the first 60 seconds. Furthermore, the optimizer gradually increased the aircraft payload in each iteration till the configuration reaches a plateau and stabilizes - Fig. 5.12. Also, the optimizer correctly found the best vertical velocity pattern, which is to maximize in the first 60 seconds and reduce it in the rest of the flight to comply with the competition maximum altitude requirements.

These results show a good comprise between all disciplines and ultimately shows the framework's capabilities of finding optimal solutions for the problem at hand.

(a) Initial configuration. (b) Score progression. (c) Optimized configuration.
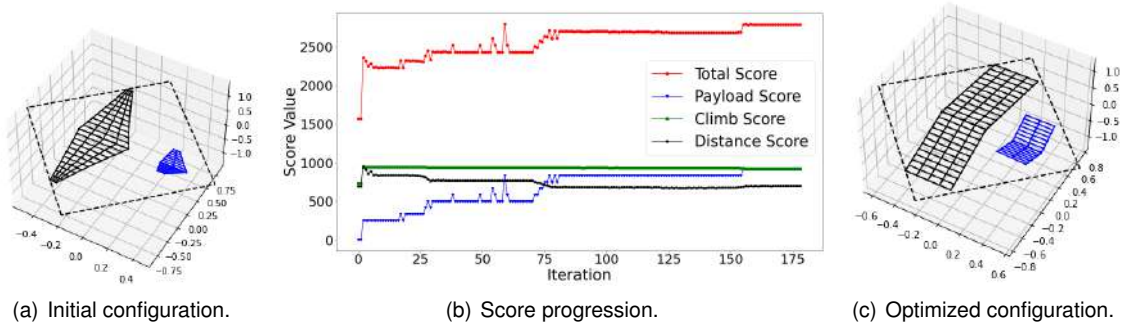
Figure 5.12: Aircraft visual results for case study #1.

(a) Aircraft's x displacement. (b) Aircraft's z displacement.
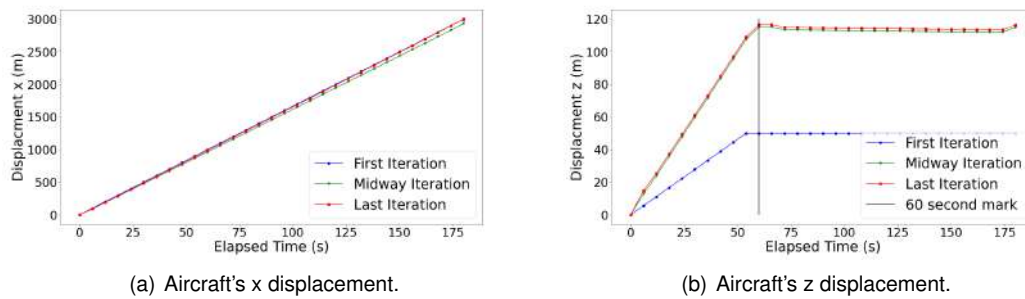
Figure 5.13: Trajectory results for for case study #1.

5.3.2 Case Study #2

In this case, the aircraft initial solution comprises a more defined wing shape with the same initial trajectory as before except for the initial climb solution that is better in this case (80m at 60 seconds). The results are presented in Figs. 5.14 and 5.15.

(a) Initial configuration. (b) Score Progression. (c) Optimized configuration.
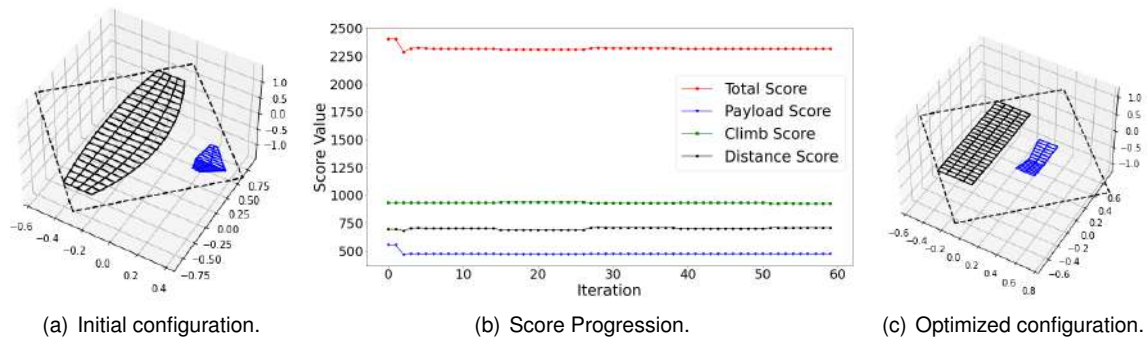
Figure 5.14: Aircraft visual results for case study #2.

For this case study, the optimized aircraft progressed into a smaller configuration to maximize climb and distance score. However, one characteristic remains: although the optimizes configuration got smaller, the wing yields a high chord to maximize the wing's surface area. This allows for more payload to be carried and thus an optimized solution for all three score parts.

The distance results in this case prove to be better than the first case studied, however, the final score is lower. This highlights the payload importance in this competition. The payload maximization

(a) Aircraft's x displacement. (b) Aircraft's z displacement.
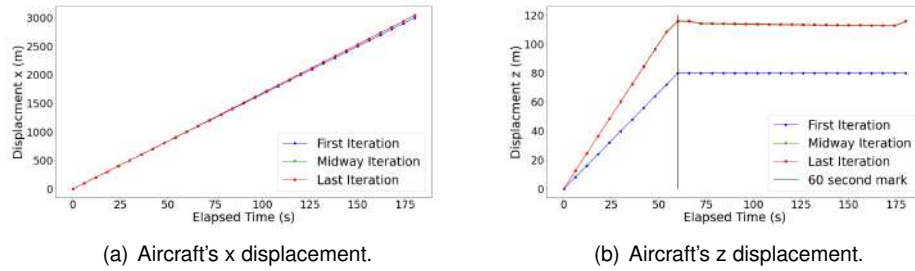
Figure 5.15: Trajectory results for for case study #2.

plays a bigger role than the other two score contributions.

Finally, the tail configuration presents an unusual design with higher tip chord when compared to the tail's root chord. This can prove that the result could have been better determined if the optimizer was allowed to pursue its search longer. However, since the results are qualitative, the important aspect of the tail are its area and mean chord, which can be taken from this result. Other unusual results follow the same fate.

5.3.3 Case Study #3

To study the importance of boundary restrictions on the optimization's routine, the aforementioned case study initial planform was used as initial solution and a lower bound restriction for the wing span of 1.8m was given. The trajectory followed the same initial configuration as the first studied case. Results are presented in Figs. 5.16 and 5.17.

(a) Initial configuration. (b) Score progression. (c) Optimized configuration.
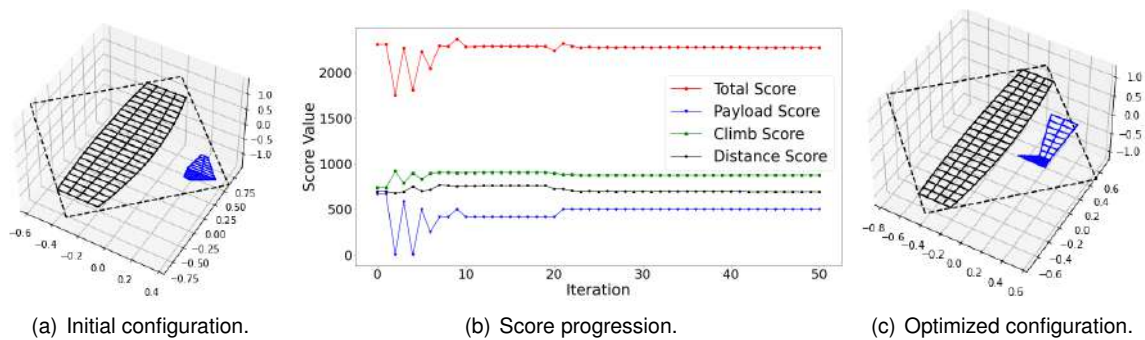
Figure 5.16: Aircraft visual results for case study #3.

By prohibiting the wing to reduce its span, the case study #2 optimized solution was converted from a smaller aircraft to a higher span solution, which produced a worst final score result, but a similar solution to the first case study. This result shows two important aspects of optimization: boundary conditions can limit an optimized design to be closer to expected results; this action can lead to worst results even if a better solution may lay near (example case study #1).

As for the trajectory, a similar trajectory to the one found in the first study is encountered, which proves their similarities.

(a) Aircraft's x displacement.   (b) Aircraft's z displacement.
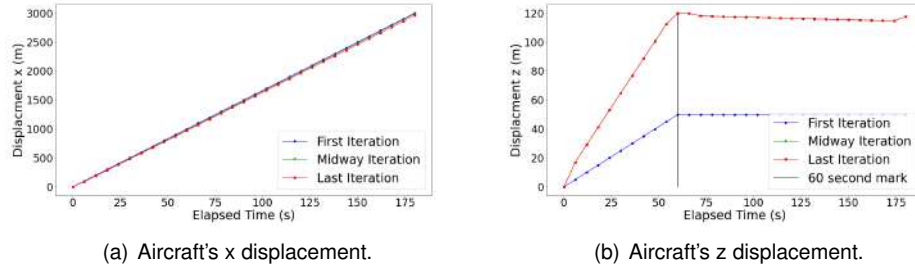
Figure 5.17: Trajectory results for for case study #3.

These results will now be analysed in more detail where the reason behind this case study poor solution in comparison to the first case study is explored.

5.3.4 In-depth Analysis

As aforementioned, in this optimization study, the purpose is to find the best set of overall metrics the aircraft should have in order to better succeed in the competition. To represent such metrics, Tab. 5.4 presents the sought for qualities in the aircraft and their values in each case study.

Table 5.4: Wing and tail conceptual design metrics for all case studies.

	Wing					Tail			
	#1	#2	#3	Average		#1	#2	#3	Average
$\overline{c_w}$ [m]	0.4	0.37	0.37	0.38	S_t [m^2]	0.15	0.08	0.10	0.11
S_w [m^2]	0.72	0.43	0.68	0.61	Λ_t [°]	-0.14	0.00	-0.09	-0.08
AR_w	4.51	3.18	5.06	4.25	τ_t [°]	35.23	35.04	59.68	43.32
Λ_w [°]	1.01	0.00	0.07	0.36					
t/c_w	0.08	0.08	0.12	0.09					
λ_w	1.00	0.98	0.77	0.92					

Results indicate three major aspects of the wing's geometric preferences for the optimized solutions: (i) the wing area is relatively high; (ii) the sweep is preferred close to null values and (iii) the wing chord is kept at the maximum.

All three studied cases present close to maximum chord values, which reveals that for all optimization cycles, the chord was maximized for the achieved wing span, which represents the wing surface area maximization for a fixed optimized span. Additionally, the thickness of the wing is kept in average at low values, which benefits a faster aircraft and increases the climb and distance score points while maintaining high wing area.

As for the tail, sweep is kept close to null or negative and the area is kept between 15 to 20 % of the wing's area. Additionally, the dihedral for the first two cases is lower and higher for the last one.

Although geometric variables give important insight about the optimized result, structural reliability must also be analysed as well as its influence on the design. Figure 5.18 presents all of the case study structural failure results for the wing and tail.

As it can be seen, the KS function values are near its minimum value, which is -1. This means the structural integrity of the wing and tail are far from being affected. This is due to the structural

(a) Case study #1. (b) Case study #2. (c) Case study #3.
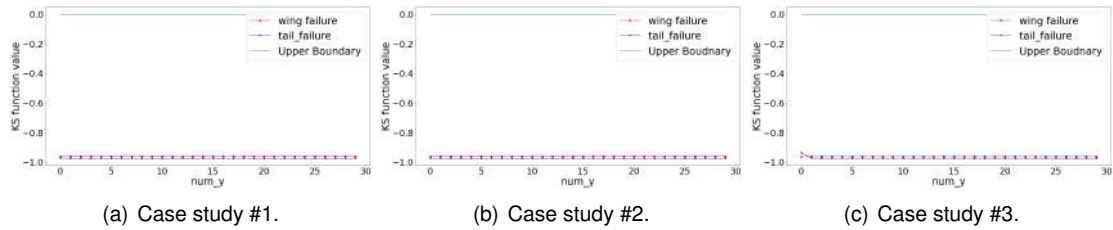
Figure 5.18: KS failure function results for the case studies presented for the wing and tail.

simplifications of the method, the high stiffness properties of the composite materials and the high box scheme chosen for the wing. Since the composites are only modelled with pure laminates instead of foam-laminate components, error arises. However, the high stiffness of the wing comes from the introduced shape of the spar. For the structural geometry of the wing, following Olissipo Air Team's recent studies, the spar is a wingbox scheme with two spars - one at around 20% of the wing's chord and the other at around 80%. This creates a large wing box scheme with high bending and torsional stiffness. Nonetheless, the results prove the reliability of such materials on the wing while still evaluating correctly the empty weight of the aircraft. The real Olissipo Air Team's prototype reveals an empty mass of 2.5kg and the optimization results lay between 2 and 3kg.

Finally, the optimized trajectory and propulsion system must be evaluated. First taking the trajectory depicted in Figs. 5.13, 5.15 and 5.17, the optimized result focus on climbing to maximize the climb score and, afterwards, focus on increasing the velocity to increase the distance score. Figure 5.19 presents the both horizontal and vertical velocities for the best solution found (case study #1).

(a) Velocity in the global x axis. (b) Velocity in the global z axis.
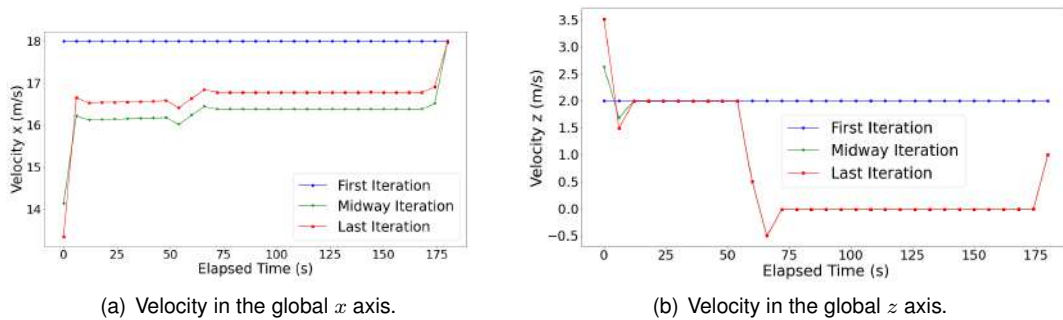
Figure 5.19: Velocity results for case study #1.

As seen, the vertical velocity has the highest values in the first 60 seconds and rapidly decreases to a null value for the rest of the flight. On the other hand, the horizontal velocity has an increase in value at the 60 seconds mark, where the aircraft finishes the climb flight segment.

As for the propulsion, Fig. 5.20 presents the Throtle results and Fig. 5.21 presents the Thrust results for all case studies.

Two distinct yet similar results arise from the studied cases. Starting with the similarities, the propulsion system engages with higher effort in the climb stage, which is expected since this is the flight segment more demanding in terms of propulsion. However, while both cases #1 and #3 seem to cap the thrust values near the maximum at the beginning, case study #2 presents more margin. This is due

(a) Case study #1.　　　　　　(b) Case study #2.　　　　　　(c) Case study #3.
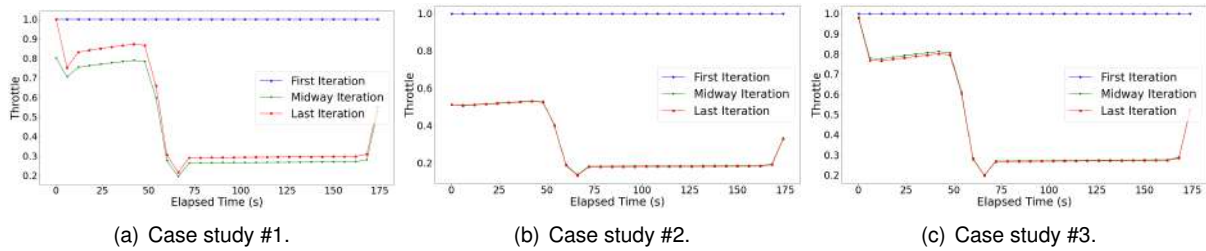
Figure 5.20: Throttle results for all studied cases.

(a) Case study #1.　　　　　　(b) Case study #2.　　　　　　(c) Case study #3.
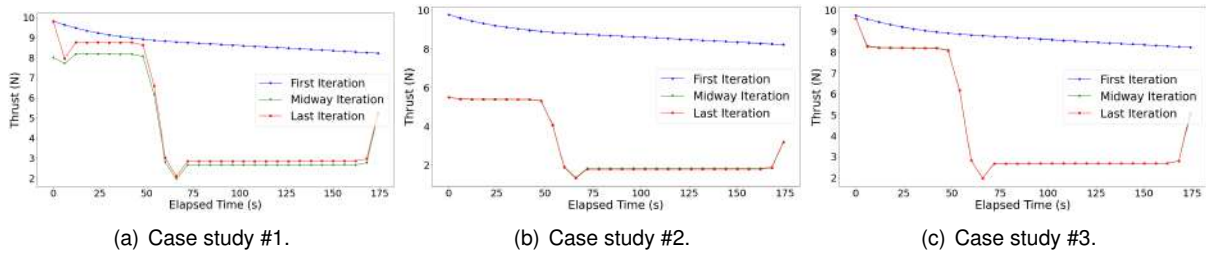
Figure 5.21: Thrust results for all studied cases.

to the aircraft weight. The aircraft in case study #2 presents smaller dimensions and thus is a lighter aircraft that requires less propulsion thrust to climb the maximum altitude score (100m).

These results show important details about the aircraft flight pattern and requirements. The most effort is produced in the climb segment and the cruise segment is less demanding for the propulsion system. This should advise carefully the design for the climb stage. Near limit designs might fail the best performance in climb stage and a margin should be given to not compromise the best result.

Another interesting result is the low throttle values for the cruise segment. This indicates that the trimmed flight occurred for a 20% to 40% of the available thrust, depending on the aircraft used. This is due to the flight region constraint: if no altitude limit was present, the throttle could have been enhanced and the aircraft's speed would increase as well, but increasing throttle changes the aircraft balance which tends to increase the aircraft altitude (different trim condition). However, this data also shows that the cruise flight can be further optimized to achieve a trimmed configuration with higher throttle and speed while maintaining similar climb behaviour.

As a last note, the voltage declining battery model is clearly present in the system, where most constant thrust regions are due to non-constant throttle inputs, which compensate the battery's decay. As for the batteries capacity, in all optimization cases it was kept at the value of around 2800 mAh, which is expected since the flight is of a short duration and the throttle at cruise is low.

Summaring the aforementioned information, the best conceptual design is a high area wing, with higher mean chord values and a small thickness ratio. The tail should have a null or negative sweep geometry with around 20 % of the wing's area. Additionally, the trajectory should aim for maximizing the climb in the first 60 seconds, where the 100m mark can be possible to achieve, and rapidly change the attitude of the aircraft to achieve maximum distance in the following cruise segment. Attention should be given on the propulsion effort in the climb segment and in the trim configuration for the cruise segment.

Furthermore, the optimized aircraft is expected to carry 8-12 bags of payload depending on the flight behaviour.

5.4 B-Spline Interpolation Usage

It was observed in Sec. 3.1 the potential of including b-spline interpolations for the control and state variables of the problem for increasing the computational efficiency without jeopardizing the optimization results. Here, a study is conducted to analyse the potentiality of using such methods using the case studies aforementioned.

5.4.1 Individual Influence

Starting with the second case study, b-spline interpolations were used independently to study their individual influence on the results. Table 5.5 yields these results where, for each variable, a 10 and 20 point controlled b-spline was used.

Table 5.5: B-spline interpolation results comparison with an optimized solution.

	CP	Score	Score $\triangle$%	Comp Time (s)	Comp Time $\triangle$%
normal	-	2337.6	-	3184.7	-
x	10	2364.7	1.16	2370.7	-25.56
	20	2360.0	0.96	2904.0	-8.81
$\dot{x}$	10	2353.9	0.70	1970.7	-38.12
	20	2424.8	3.73	4194.0	31.69
z	10	2373.3	1.53	4785.9	50.28
	20	2370.8	1.42	3173.7	-0.35
$\dot{z}$	10	2377.2	1.69	3791.0	19.04
	20	2386.0	2.07	3117.7	-2.10
δ_t	10	2392.2	2.34	4030.3	26.55
	20	2350.2	0.54	5053.0	58.67
δ_{stab}	10	2427.0	3.82	2850.0	-10.51
	20	2337.3	-0.01	3076.1	-3.41

The results present, at first, interesting results - although the final score value change has minimal differences (maximum is 3.82%), the computational time yields large differences, both positive and negative. Furthermore, all results with b-spline interpolation methods produced slightly higher score responses.

These results prove, once more, that single variable b-spline interpolation exploitation may not interfere with the results but do, however, have an impact on the optimization efficiency.

Results show that lower control point inputs produce higher computational times when comparing with higher number of control points, except for the throttle variable that will be discussed later on. This is due to the low flexibility the low control point b-splines methods deliver. By definition of the method used within the created framework, a lower number of control points will always produce a lower computational time for each iteration in the optimization. However, the lower the control points are, the stiffer is the curve produced by them, which delivers a more complex search and thus more optimization

iterations.

Another interesting detail is how the shape of the result function affects the optimal number of control points. For the state variable x, a lower control point method produces better computational efficiency. This is due to the fact that the x optimal values are almost a linear function through time, which can almost be defined by a 2 point control point scheme. However, if the state variable z is considered, a low control point method will poorly define the optimal solution while a higher number of control points will create a better approximation - notice that for the state variable z, the computational efficiency increases from a 50% loss to a 0.3% gain when changing from 10 to 20 control points.

Next, a better visualization of the results will be given where all b-spline functions will be evaluated simultaneously considering case study (#3).

5.4.2 Global Influence

To study the performance influence of global b-spline interpolation usage, the control points used were chosen based on the previous individual influence results and on experimental optimization runs. These are presented in Tab. 5.6, where the summarized results are also included.

Table 5.6: Control points used for global influence analysis of the b-spline interpolation method.

	x	$\dot{x}$	z	$\dot{z}$	δ_t	δ_{stab}
CP	20	20	25	25	10	20
Score	2374.5		Score $\Delta\%$		4.33	
Comp time (s)	4186.9		Comp time $\Delta\%$		-42.73	

Clearly, the b-spline method implemented not only increases the obtained score value by more than 4%, but also decreases the computational time efforts by almost 43%. These results prove the importance of the implemented method and the benefits of using such method in more complex systems with higher computational efforts. Additionally, by representing each state and control variable by interpolating functions, this method creates more realistic smooth function curves that are closer to the aircraft's real scenario. Figure 5.22 present the b-spline interpolation trajectory state variables results.

Furthermore, the b-spline method accurately found the maximum climb point, whereas the traditional method did not. Similar results appear for the control variables (propulsion) - Fig. 5.23.

Finally, the modified model aircraft geometry result was also different from the one found without the b-spline implementation. Figure 5.24 comprises the new found design.

In this scenario, the optimizer converged to a higher aspect ratio wing and smaller mean wing chord, which allowed for a higher climb and distance scores with a small decrease in the payload score.

With further control point study, a better solution might be found and/or a better computational gain can be achieved as well. Although the control points attributing is problem dependent and need analysis from previous optimization cycles, it can prove useful to describe the state and control variables with b-spline interpolations, since it can greatly reduce the cost of optimizing the overall design.

(a) Displacement in the x axis.

(b) Velocity in the x axis.

(c) Displacement in the z axis.

(d) Velocity in the x axis.
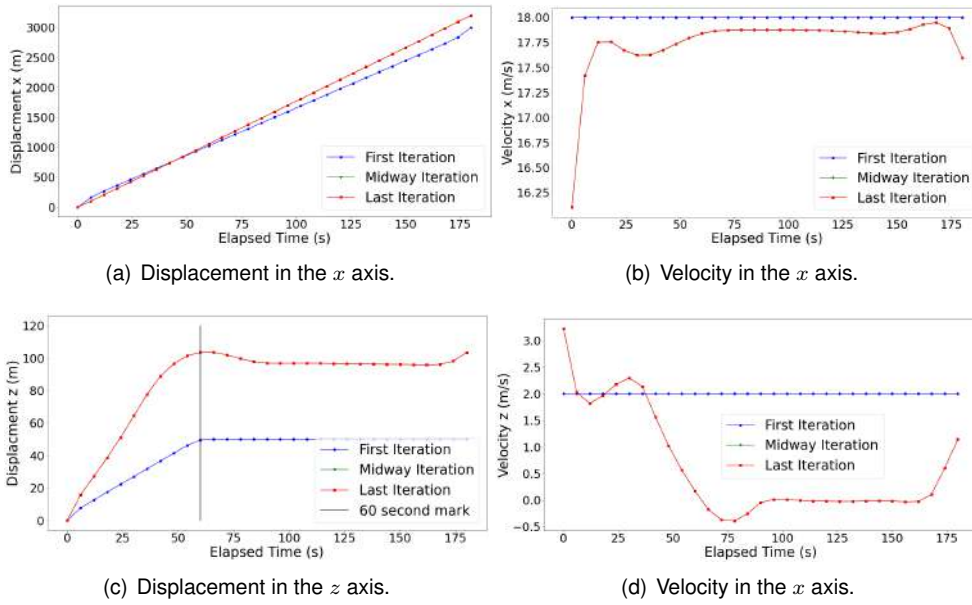
Figure 5.22: Trajectory state variables results for the implemented b-spline interpolation method for all state and control variables.

(a) Throttle results.

(b) Thrust results.
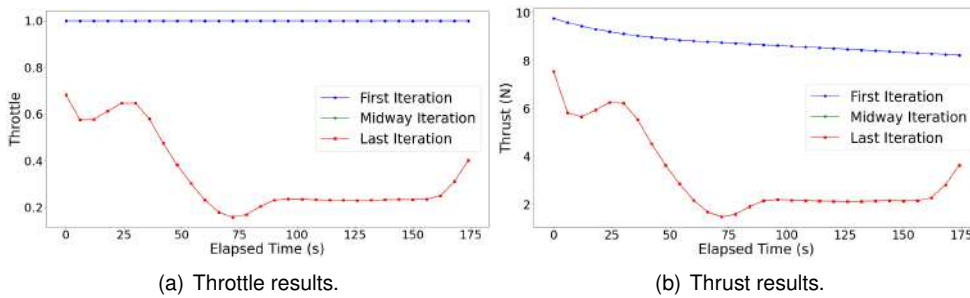
Figure 5.23: Trajectory control variables results for the implemented b-spline interpolation method for all state and control variables.
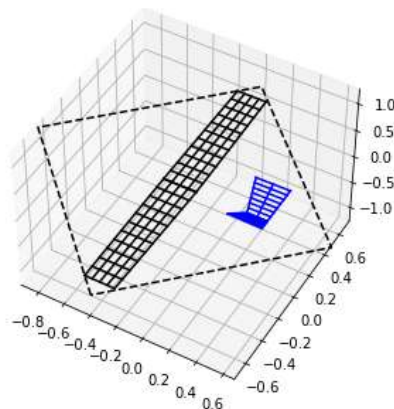
Figure 5.24: Aircraft planform result for the implemented b-spline method for all state and control variables.

5.5 Thrust Model Comparison

To visualize the influence of the battery model in the optimization results, case study #3 was used to achieve a propulsive model comparison between the two models implemented.

Both optimizations started with the same initial configuration and the propulsive response of the simpler propulsion model is presented in Fig 5.25.

| (a) Throttle results. | (b) Thrust results. |
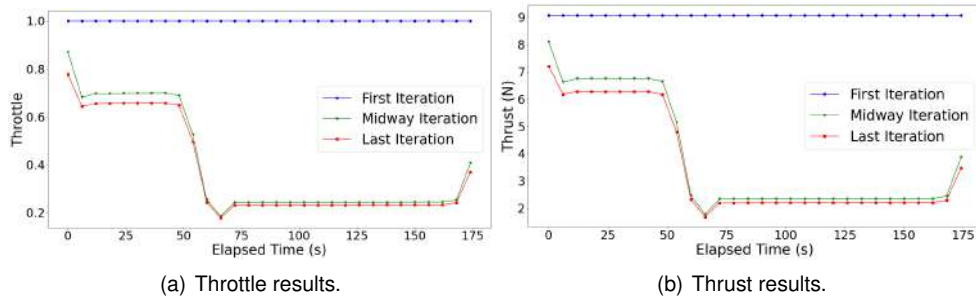
Figure 5.25: Propulsion system results for the simpler propulsive model implemented.

Comparing these with the results shown in 5.20(c) and 5.21(c), the thrust curve is almost identical, however the throttle curve is different. For the decay battery model, the throttle input must be corrected to a non-constant curve to perform a constant curve for the thrust curve. On the other hand, for the constant power model, the throttle and thrust curves have a linear correspondence.

Additionally, optimization results were also different, increasing the total score by 3.27% (from 2275.9 to 2350.4) and reducing the computational time by 25.73%. The optimized planform is present in Fig. 5.26.
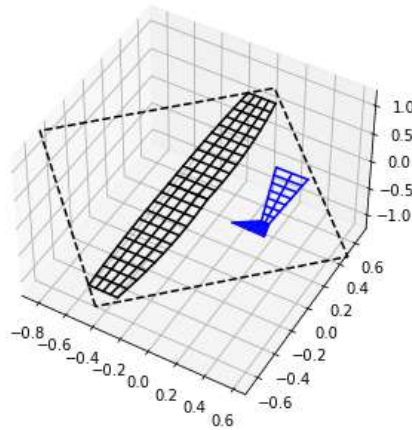
Figure 5.26: Optimized planform for the constant power propulsive model.

Similar to the results found in the b-spline interpolation integration, the optimized wing is a higher aspect ratio wing with smaller mean chord values.

Although these results improve the optimizer efficiency and results, it proves that a poor representative model of the propulsive system can induce unrealistic score results and consequently provide an unrealistic optimized solution.

Chapter 6

Conclusions

6.1 Achievements

In this work, a framework was developed to study the ACC 2022 competition optimal conceptual design. The framework, based on *OpenAeroStruct*, includes problem specific modules to fully comply with the competition rules [16]. Additionally to the aerostructural module present, a trajectory optimization module was implemented based on a collocation point method with the option for b-spline interpolation functions to increase optimization efficiency. Constant and decay power propulsion models were implemented to model the propulsion system response to a control input. The additional aircraft modules were introduced according to the competition conditions and to the Olissipo Air Team recent developments.

The ACC 2022 optimal design characteristics were determined based on different singular and global case studies. Coupled design and trajectory optimizations were conducted leading to the following conclusions: (i) climb maximum height is possible to achieve and should be the focus of the first sixty seconds of flight; (ii) the wing area should be maximized within the bounded limits to maximize cargo; (iii) tail and wing geometries follow similar tendencies in all optimization cases, which helps defining a optimal conceptual region; (iv) to maximize travelled distance, trim conditions should be carefully analysed to assure a near maximum thrust condition on the cruise part.

As for the trajectory efficiency b-spline interpolation model implemented, results show higher computational efficiency with better search paths are found using this method. Also, the computational efficiency gains depend on the control points used for each control and state variables. A control point study can lead to large computational efficiency gains. In this thesis a 42.73% computational efficiency gain was acquired.

Finally, propulsive models implemented gave information about the importance of the usage of realistic models. Non-realistic models can induce better but unrealistic results. The constant power model presented an unrealistic control input to throttle response - constant throttle through time produced constant thrust. However, the power decay method had a non-linear behaviour that more accurately represented the model at hand. To produce a constant thrust flight segment, a non-linear throttle input had to be given.

6.2 Future Work

This work was based on conceptual design models that led to conceptual design solutions to better understand the problem studied. However, future work can be done to increase the results accuracy and achieve a better framework. These include:

- **Inclusion of 3D trajectory analysis** - this thesis only considered longitudinal behaviour. With the inclusion of complete 3D flight behaviour a more precise trajectory result can be obtained, which could accuratlly represent lateral behaviour needed to comply with the Air Cargo Challenge 2022 [16] flight region requirement. However, the imposition of 3D coordinates increases each collocation point variable dimension from 4 to 9 and the constraints for the collocation method from 4 to 9 as well, which increases the optimization problem by $n \times 5$ for both variable size and constraint size. This effect can be mitigated using the b-spline method presented in this thesis;

- **Better stability models** - this thesis considered only trimmed flight conditions, whereas a full stability model might produce more accurate solutions. The inclusion of a more accurate stability model with aerodynamic calculations inside each optimization cycle would create a more realistic aircraft design. However, it would imply a higher computational effort since for stability a range of angle attack evaluations must be made;

- **Higher fidelity aerodynamic and structural model** - this work uses low fidelity structural and aerodynamic models that can be improved to more accurate problem specific models. However, attention should be taken to maintain the computational efficiency. A better aerodynamic model, such as 3D panel method, could be implemented to better represent 3D aspects of the wing. In the same manner, a more accurate structural model with composite failure mechanisms and a more precise section property determination can increase the reliability of the final results. However, the inclusion of such models would create computational efficiency problems, which for a conceptual initial design may not be optimal;

- **Inclusion of b-spline methods for the final results** - this work only analysed the results of a non-modified trajectory collocation point method. The inclusion of the b-spline method would reduce each optimization cycle efficiency and produce more optimal conceptual designs. However, an in-depth control point analysis should be taken to correctly evaluate the influence of each b-spline interpolation to correctly use a standard b-spline interpolation formulation for every analyses while securing convergence and efficiency. Nonetheless, if a study is conducted, b-spline methods should be used throughout the analyses.

Bibliography

[1] J. Jonh D. Anderson. *Aircraft Performance and Design*, volume 1, chapter The Evolution of the Airplane and its Performance: A Short History, pages 3–47. McGraw-Hill, 1999.

[2] D. Keidel, G. Molinari, and P. Ermanni. Aero-structural optimization and analysis of a camber-morphing flying wing: Structural and wind tunnel testing. *Journal of Intelligent Material Systems and Structures*, 30(6):908–923, 2019. doi: 10.1177/1045389X19828501.

[3] R. Onishi, T. Kimura, Z. Guo, and T. Iwamiya. *Coupled aero-structural model - Approach and application to high aspect-ratio wing-box structures*. doi: 10.2514/6.1998-4837.

[4] J. R. R. A. Martins, J. J. Alonso, and J. J. Reuther. High-fidelity aerostructural design optimization of a supersonic business jet. *Journal of Aircraft*, 41(3):523–530, 2004. doi: 10.2514/1.11478.

[5] A. Jameson, K. Leoviriyakit, and S. Shankaran. Multi-point aero-structural optimization of wings including planform variations. *Collection of Technical Papers - 45th AIAA Aerospace Sciences Meeting*, 14, 01 2007. doi: 10.2514/6.2007-764.

[6] D. P. Raymer. *Aicraft Design: A Conceptual Approach*. American Institute of Aeronautics and Astronautics, Inc., 2nd edition, 1992. ISBN:0-930403-51-7.

[7] C. You and R. Zhang. 3d trajectory optimization in rician fading for UAV-enabled data harvesting. *IEEE Transactions on Wireless Communications*, 18(6):3192–3207, 2019. doi: 10.1109/TWC.2019.2911939.

[8] S. Carabaza, J. Scherer, B. Rinner, J. Lopez-Orozco, and E. Besada. UAV trajectory optimization for minimum time search with communication constraints and collision avoidance. *Engineering Applications of Artificial Intelligence*, 85:357–371, 07 2019. doi: 10.1016/j.engappai.2019.06.002.

[9] V. Dobrokhodov, K. Jones, C. Walton, and I. Kaminer. Energy-optimal trajectory planning of hybrid ultra-long endurance UAV in time-varying energy fields. 01 2020. doi: 10.2514/6.2020-2299.

[10] R. Liem, G. Kenway, and J. Martins. Multimission aircraft fuel-burn minimization via multipoint aerostructural optimization. *AIAA Journal*, 53:104–122, 01 2015. doi: 10.2514/1.J052940.

[11] S. Gudmundson. *General Aviation Aircraft Design: Applied Methods and Procedures*, volume 1, chapter Performance - Range Analysis, pages 896–923. Elsevier Inc., 2014.

[12] J. Gray, J. Hwang, J. Martins, K. Moore, and B. Naylor. Openmdao: An open-source framework for multidisciplinary design, analysis, and optimization. *Structural and Multidisciplinary Optimization*, pages 1075–1104, 04 2019. doi: 10.1007/s00158-019-02211-z.

[13] D. Burdette and J. Martins. Design of a transonic wing with an adaptive morphing trailing edge via aerostructural optimization. *Aerospace Science and Technology*, 81, 08 2018. doi: 10.1016/j.ast.2018.08.004.

[14] G. J. K. Timothy R. Brooks, Joaquim R. R. A. Martins. High-fidelity aerostructural optimization of tow-steered composite wings. *Journal of Fluids and Structures*, 88:122–147, Feb. 2019. doi:10.1016/j.jfluidstructs.2019.04.005.

[15] G. Oliveira. Coupled aircraft design and trajectory optimization of an electric UAV. Master's thesis, Instituto Superior Técnico, 2021.

[16] Air cargo challenge 2022 participation handbook, March 2021. version 01.11.

[17] D. P. Raymer. *Enhancing Aircraft Conceptual Design Using Multidisciplinary Optimization*. PhD thesis, Royal Institute of Technology, May 2002. ISBN 91-7283-259-2.

[18] S. K. Abdelkader Benaouali. Multidisciplinary design optimization of aircraft wing using commercial software integration. *Aerospace Science and Technology*, 92:766–776, Sept. 2019. doi:10.1016/j.ast.2019.06.040.

[19] P. E. Giulio Molinari, Andres F. Arrieta. Aero-structural optimization of three dimensional adaptive wings with embedded smart actuators. *AIAA Journal*, 52(9):1940–1950, Sept. 2014. doi:10.2514/1.J052715.

[20] J. Martins and A. Lambe. Multidisciplinary design optimization: A survey of architectures. *AIAA Journal*, 51:2049–2075, 09 2013. doi: 10.2514/1.J051895.

[21] I. M. Kroo. *Multidisciplinary Design Optimization: State-of-the-Art*, chapter MDO for Large-Scale Design, pages 22–44. Society for Industrial and Applied Mathematics, 1997.

[22] A. Lambe and J. Martins. Extensions to the design structure matrix for the description of multidisciplinary design, analysis, and optimization processes. *Structural and Multidisciplinary Optimization*, 08 2012. doi: 10.1007/s00158-012-0763-y.

[23] G. Kennedy and J. R. R. A. Martins. *Parallel Solution Methods for Aerostructural Analysis and Design Optimization*. doi: 10.2514/6.2010-9308.

[24] N. P. Tedford and J. R. R. A. Martins. On the common structure of MDO problems: A comparison of architectures. In *Proceedings of the 11th AIAA/ISSMO Multidisciplinary Analysis and Optimization Conference*, Sept. 2006. AIAA 2006-7080.

[25] A. C. Marta. Aircraft optimal design. MSc Course Notes, 2019, Insituto Superior Técnico, Lisbon, Portugal.

[26] P. Mohammad Zadeh and M. Sayadi. An efficient aerodynamic shape optimization of blended wing body UAV using multi-fidelity models. *Chinese Journal of Aeronautics*, 31, 04 2018. doi: 10.1016/j.cja.2018.04.004.

[27] Z.-H. Han, J. Chen, K.-S. Zhang, Z.-M. Xu, Z. Zhu, and W.-P. Song. Aerodynamic shape optimization of natural-laminar-flow wing using surrogate-based approach. *AIAA Journal*, 56(7):2579–2593, 2018. doi: 10.2514/1.J056661.

[28] J. Anderson. *Fundamentals of Aerodynamics*. McGraw-Hill Education, 6th edition, 2016. ISBN-13: 978-1259129919.

[29] W. F. Phillips and D. O. Snyder. Modern adaptation of Prandtl's classic lifting-line theory. *Journal of Aircraft*, 37(4):662–670, 2000. doi: 10.2514/2.2649.

[30] J. P. Jasa, J. T. Hwang, and J. R. R. A. Martins. Open-source coupled aerostructural optimization using python. *Structural and Multidisciplinary Optimization*, 57:1815–1827, 2018.

[31] Wing-connector: Glass / carbon tube (26.5/25) x 1000 mm. https://shop1.r-g.de/en/art/74272523S.

[32] G. Zucco, V. Oliveri, M. Rouhi, R. Telford, D. Peeters, G. Clancy, C. McHale, R. O'Higgins, T. Young, and P. Weaver. Static test of a variable stiffness thermoplastic composite wingbox under shear, bending and torsion. *Aeronautical Journal -New Series-*, 124, 12 2019. doi: 10.1017/aer.2019.161.

[33] S. S. Chauhan and J. R. R. A. Martins. Low-fidelity aerostructural optimization of aircraft wings with a simplified wingbox model using OpenAeroStruct. In *Proceedings of the 6th International Conference on Engineering Optimization, EngOpt 2018*, pages 418–431, Lisbon, Portugal, Sept. 2018. Springer. doi: 10.1007/978-3-319-97773-7_38.

[34] T. Megson. *Aircraft Structures for Engineering Students*. Elsevier aerospace engineering series. Elsevier Science, 2007. ISBN 9780080488318.

[35] G. Kreisselmeier and R. Steinhauser. Systematic control design by optimizing a vector performance index. *IFAC Proceedings Volumes*, 12(7):113–117, 1979. ISSN 1474-6670. doi: 10.1016/S1474-6670(17)65584-8. IFAC Symposium on computer Aided Design of Control Systems, Zurich, Switzerland, 29-31 August.

[36] L. Traub. Calculation of constant power lithium battery discharge curves. *Batteries*, 2:17, 06 2016. doi: 10.3390/batteries2020017.

[37] Rc lipo battery guide: Explanation, safety, and care. http://learningrc.com/lipo-battery/.

[38] M. Bronz, J. M. Moschetta, and G. Hattenberger. Multi-point optimisation of a propulsion set as applied to a multi-tasking MAV.

[39] A. Junid, S. A. Zaki, S. Susilawati, and Y. A. Abakr. Efficiency of brushed and brushless electronic speed control systems and lithium batteries. In *2017 IEEE 15th Student Conference on Research and Development (SCOReD)*, pages 332–337, 2017. doi: 10.1109/SCORED.2017.8305369.

[40] M. Bronz, J.-M. Moschetta, and G. Hattenberger. Multi-point optimisation of a propulsion set as applied to a multi-tasking MAV. 07 2012.

[41] C. Tjhai. Developing stochastic model of thrust and flight dynamics for small UAVs. Master's thesis, University of Minnesota, 2013.

[42] S. Chauhan and J. Martins. Tilt-wing eVTOL takeoff trajectory optimization. *Journal of Aircraft*, 57: 1–20, 11 2019. doi: 10.2514/1.C035476.

[43] F. Weick. *Aircraft Propeller Design*. McGraw-Hill Book Company, Incorporated, 1930. ISBN 9780598630872.

[44] B. McCormick. *Aerodynamics, Aeronautics, and Flight Mechanics*. Wiley, 1994. ISBN 9780471575061.

[45] M. Kelly. An introduction to trajectory optimization: How to do your own direct collocation. *SIAM Review*, 59(4):849–904, 2017. doi: 10.1137/16M1062569.

[46] J. T. Betts. Survey of numerical methods for trajectory optimization. *Journal of Guidance, Control, and Dynamics*, 21(2):193–207, 1998. doi: 10.2514/2.4231.

[47] V. M. Becerra. *Practical Direct Collocation Methods for Computational Optimal Control*, pages 33–60. Springer New York, New York, NY, 2013.

[48] ICLOCS2. Example: Bang-bang control (multi-phase). http://www.ee.ic.ac.uk/ICLOCS

[49] PowerStream. Discharge rate. https://www.powerstream.com/18650-high-discharge-rate.html.

[50] S. Gudmundson. *General Aviation Aircraft Design: Applied Methods and Procedures*, volume 1, chapter Aircraft Drag Analysis, pages 663–759. Elsevier Inc., 2014.

[51] S. Hoerner. *Fluid-dynamic Drag: Practical Information on Aerodynamic Drag and Hydrodynamic Resistance*. Hoerner Fluid Dynamics, 1965.

[52] H. Schlichting and K. Gersten. *Boundary-Layer Theory*. Springer, 8th edition, 2000. ISBN 978-3-642-85829-1.

[53] S. Gudmundson. *General Aviation Aircraft Design: Applied Methods and Procedures*, volume 1, chapter The Anatomy of the Tail, pages 460–519. Elsevier Inc., 2014.

[54] A. Deperrois. Xflr5. http://www.xflr5.tech/xflr5.htm.

[55] S. Gudmundson. *General Aviation Aircraft Design: Applied Methods and Procedures*, volume 1, chapter Performance - Take-Off, pages 791–820. Elsevier Inc., 2014.

[56] R. Lafage, S. Defoort, and T. Lefebvre. Whatsopt: a web application for multidisciplinary design analysis and optimization. In *AIAA Aviation 2019 Forum*, page 2990, 2019. doi: 10.2514/ 6.2019-2990.

[57] R. Lewis, G. Shubin, E. Cramer, J. Dennis, P. Frank, R. Michael, L. Gregory, and R. Shubin. Problem formulation for multidisciplinary optimization. *SIAM Journal on Optimization*, 4, 02 1997. doi: 10.1137/0804044.

[58] SciPy. minimize(method='slsqp'). https://docs.scipy.org/doc/scipy/reference/optimize.minimize-slsqp.html.

[59] GoodFellow. Carbon/epoxy composite - material information. http://www.goodfellow.com/A/Carbon-Epoxy-Composite.html.

Appendix A

Problem Variables

A.1 Problem Variables

Table A.1: Other problem parameters described in the framework.

	Variable	Meaning	Type	Control Points	Value/Boundaries
Trajectory	x	displacement x	Design	n	[0, 10000] m
	z	displacement z	Design	n	[0, 120] m
	$\dot{x}$	velocity x	Design	n	[0, 25] m/s
	$\dot{z}$	velocity z	Design	n	[0, 18] m/s
	$t_{elapsed}$	elapsed time	Constant	-	180 s
	δ_t	throttle	Design	n	[0, 1]
	δ_{stab}	stabilator angle	Design	n	[-25, 25] [°]
	ϕ	bank angle	Design	n	[-60, 60] [°]
	α	angle of attack	Design	n	[-15, 15] [°]
	ζ_x	displacement x's defect	Constraint	-	[-1e-3, 1e-3]
	ζ_z	displacement z's defect	Constraint	-	[-1e-3, 1e-3]
	ζ_{fx}	force x's defect	Constraint	-	[-1e-3, 1e-3]
	ζ_{fz}	force z's defect	Constraint	-	[-1e-3, 1e-3]
Energy	C_b	battery's capacity	Design	-	[2, 10] Ah
	e	specific energy	Constant	-	600000 J/kg
	ue	usable energy factor	Constant	-	60 %
	Model	propulsion model	Fixed Design	-	0 or 1
	C_{max}	usable capacity	Constraint	-	-
	E_{max}	usable energy	Constraint	-	-
Geometry	l_t	tail-wing distance	Design	-	[-1e-3, 1e-3]
	β	rhombus box angle	Design	-	[70, 140] [°]
	l_{ds}	lateral diagonal available space	Constraint	-	>0
	h_{vs}	vertical space available at tip chord	Constraint	-	>0
	l_{fit}	tail diagonal available space	Constraint	-	>0
	h_{tip}	tail available space at tip chord	Constraint	-	>0
	V_{VT}	tail volume coefficient	Constraint	-	[0.04, 0.09]

Table A.2: Aircraft problem parameters described in the framework.

	Variable	Meaning	Type	Control Points	Value/Boundaries
Wing	b_w	wing's span	Design	-	[1, 3] m
	τ_w	wing's dihedral angle	Fixed Design	-	-
	Λ_w	wing's sweep angle	Design	-	[-5, 30] [°]
	CL_{0_w}	wing's CL_0	Constant	-	0.4
	CD_{0_w}	wing's CD_0	Constant	-	0.008
	Cl_w	wing's 2D Cl	Constraint	-	<1.3
	t/c_{max_w}	wing's maximum thickness ratio	Constant	-	0.2533
	t_{spar}	spar's thickness	Design	2	[0.15, 1] mm
	t_{skin}	skin's thickness	Design	2	[0.15, 1] mm
	t/c_w	wing's thickness	Design	2	[0.08, 0.12]
	c_w	wing's chord	Design	3	[0.05, 0.4] m
	θ_w	wing's twist	Design	3	[-5, 5] [°]
	$KS_{failure_w}$	wing's KS failure function	Constraint	-	<0
Tail	b_t	tail's span	Design	-	[0.1, 0.6] m
	τ_t	tail's dihedral angle	Fixed Design	-	-
	Λ_t	tail's sweep angle	Design	-	[-3 ,10] [°]
	CL_{0_t}	tail's CL_0	Constant	-	0
	CD_{0_t}	tail's CD_0	Constant	-	0.006
	Cl_t	tail's 2D Cl	Constraint	-	0.95
	t/c_{max_t}	tail's maximum thickness ratio	Constant	-	0.2953
	t/c_t	tail's thickness	Constant	1	0.09
	t_{tube}	tube thickness	Design	1	[0.15, 0.5] mm
	c_t	tail's chord	Design	2	[0.05, 0.25] m
	θ_t	tail's twist	Constant	1	0
	$KS_{failure_t}$	tail's KS failure function	Constraint	-	<0
	$t_{intersect}$	tail's tube intersection	Constraint	-	<0
Mass	W_0	empty weight	Constant	-	1 kg
	CG_{empty}	W_0's CG location	Fixed Design	-	-
	W_b	battery weight	Design	-	[0.2, 2]
	W_p	payload weight	Design	-	[0, 4]
	CG_p	payload's CG location	Design	-	[-1 to 1, 0, 0] m
Take-off	CL_{to}	Take-off CL	Constant	-	0.3
	CD_{to}	Take-off CD	Constant	-	0.02
	CL_{max}	Maximum CL	Constant	-	1.5 (with flaps)
	μ_{track}	track's friction coefficient	Constant	-	0.07
Stability	C_m	moment coefficient	Constraint	-	[-1e-3, 1e-3]

Appendix B

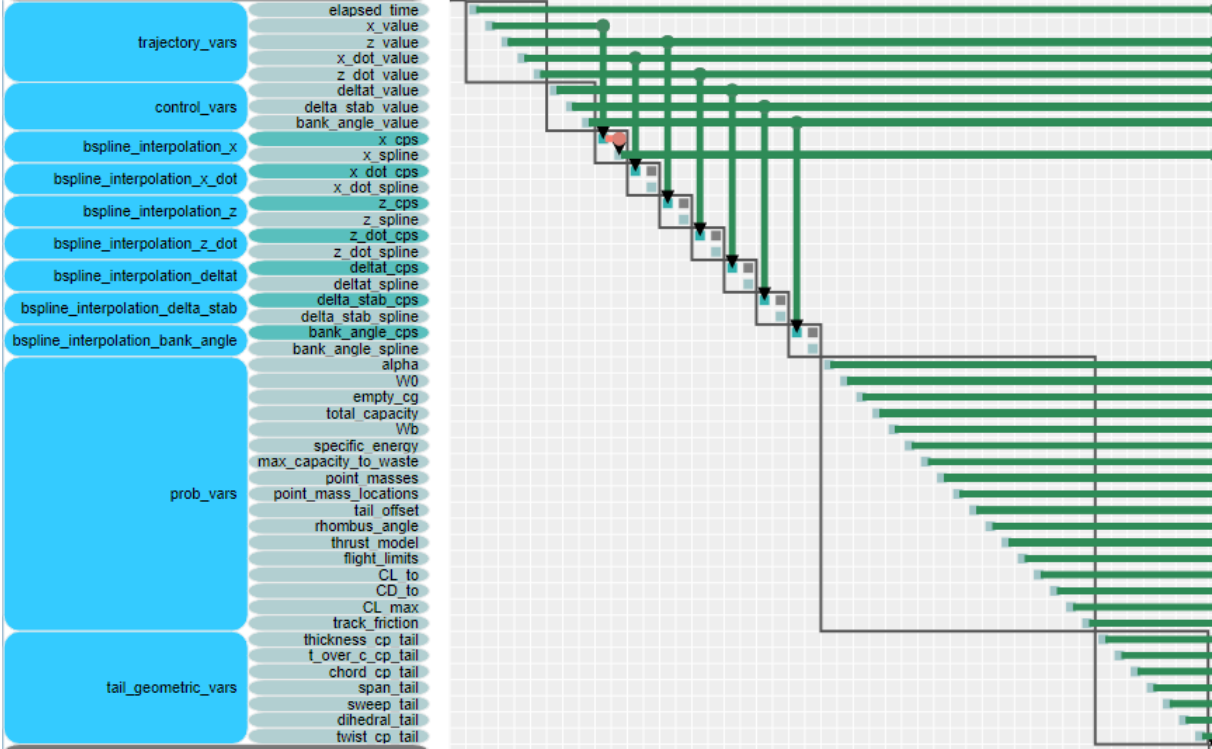# Framework Diagrams

B.1 N2 Diagrams

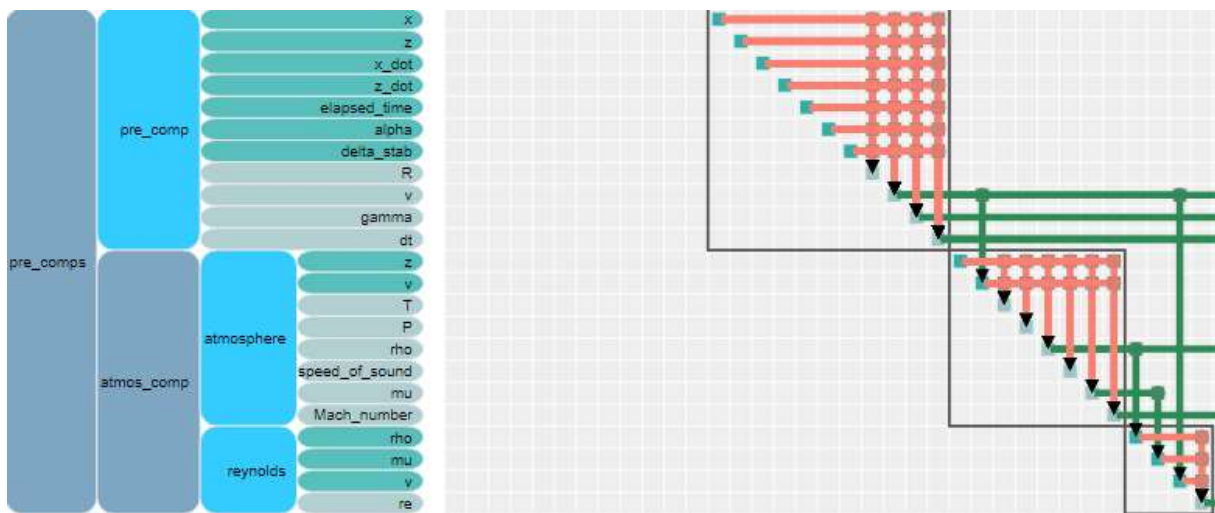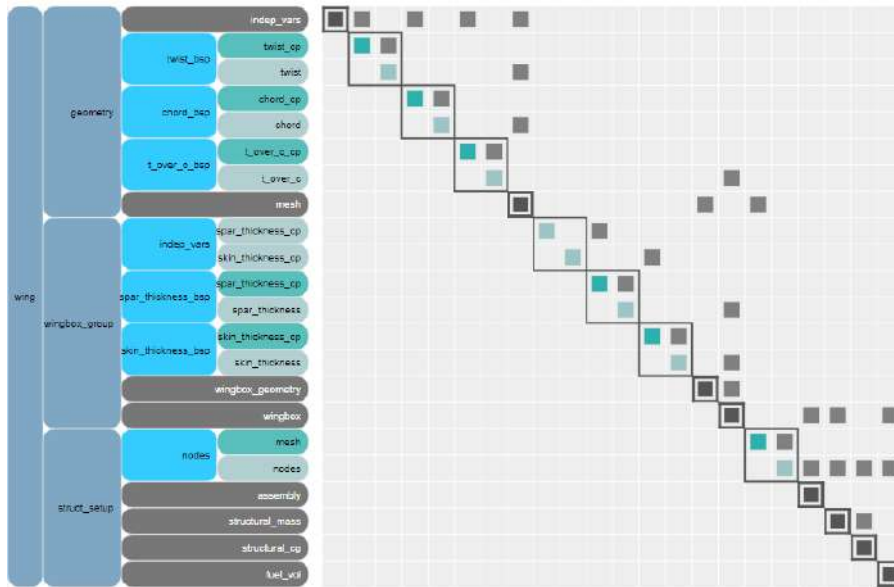Figure B.1: N2 diagram for the problem variables modules.

Figure B.2: N2 diagram portion for the pre calculation modules

(a) N2 diagram portion for the wing's aero-structural definition

(b) N2 diagram portion for the take-off module.

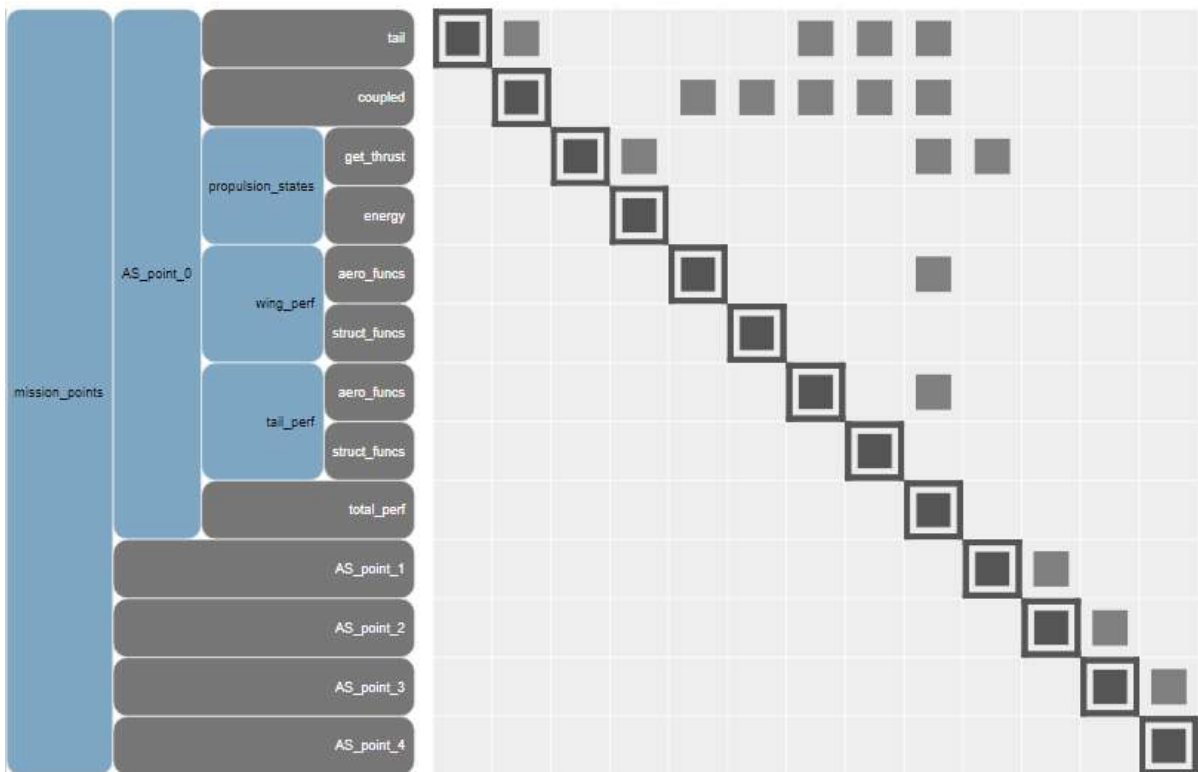Figure B.3: N2 diagrams for the wing and take-off modules.

Figure B.4: N2 diagram portion for the mission points calculations using 5 points.
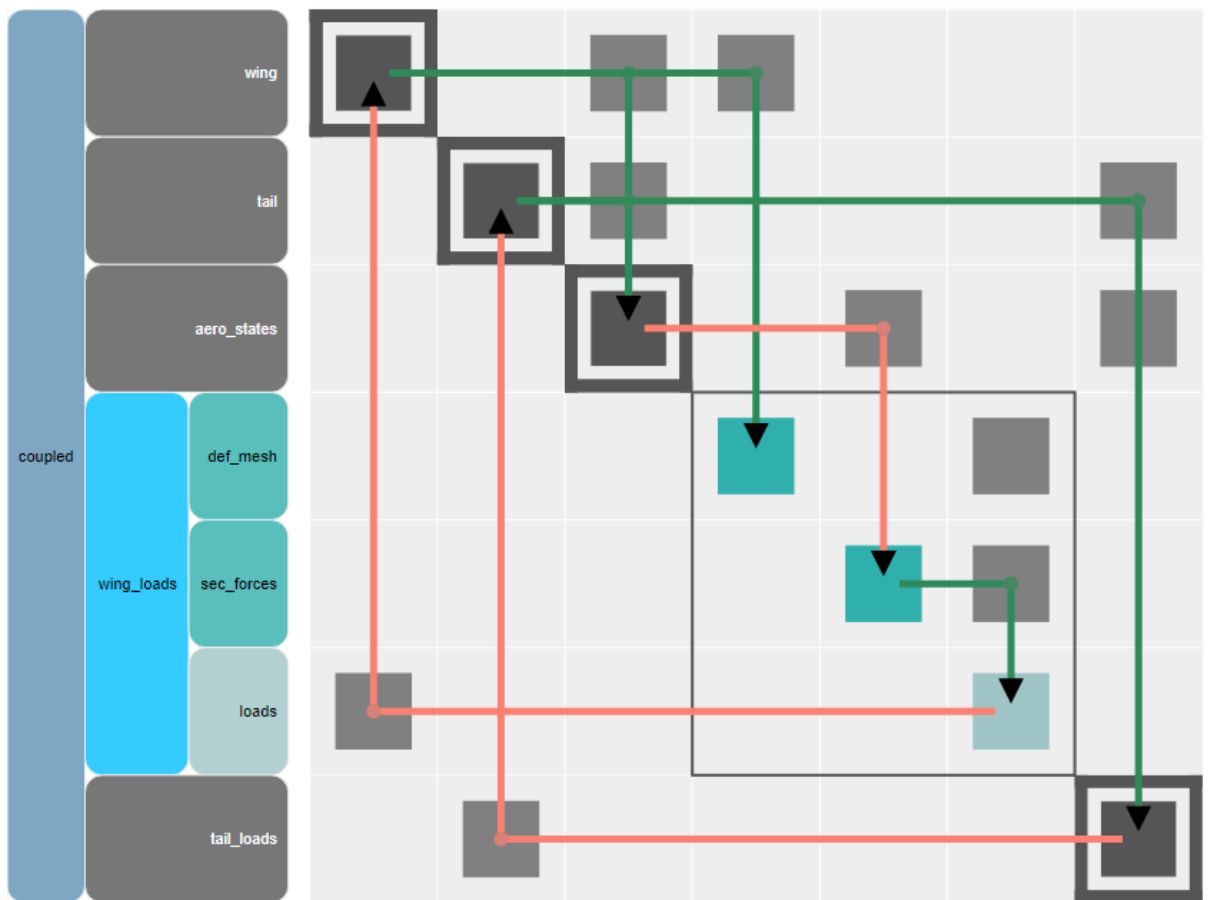
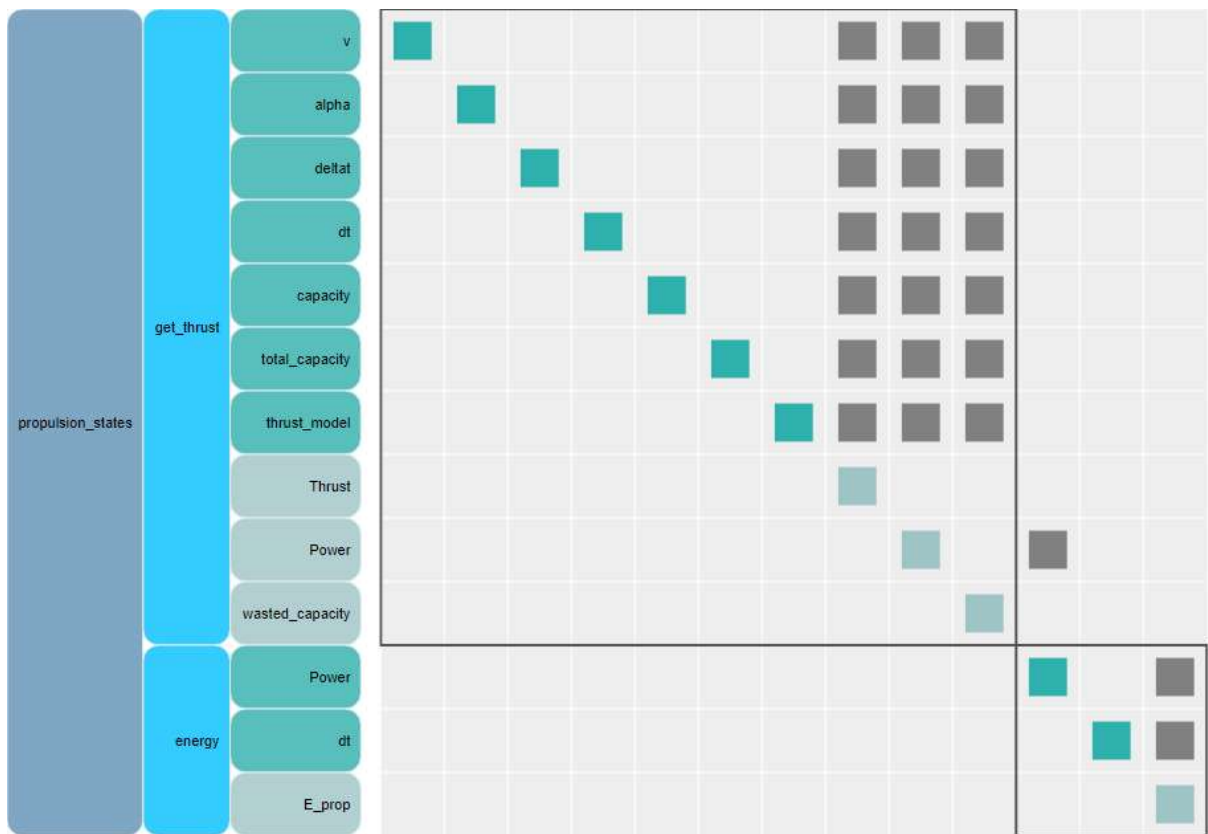Figure B.5: N2 diagram portion for aero-structural cycle.

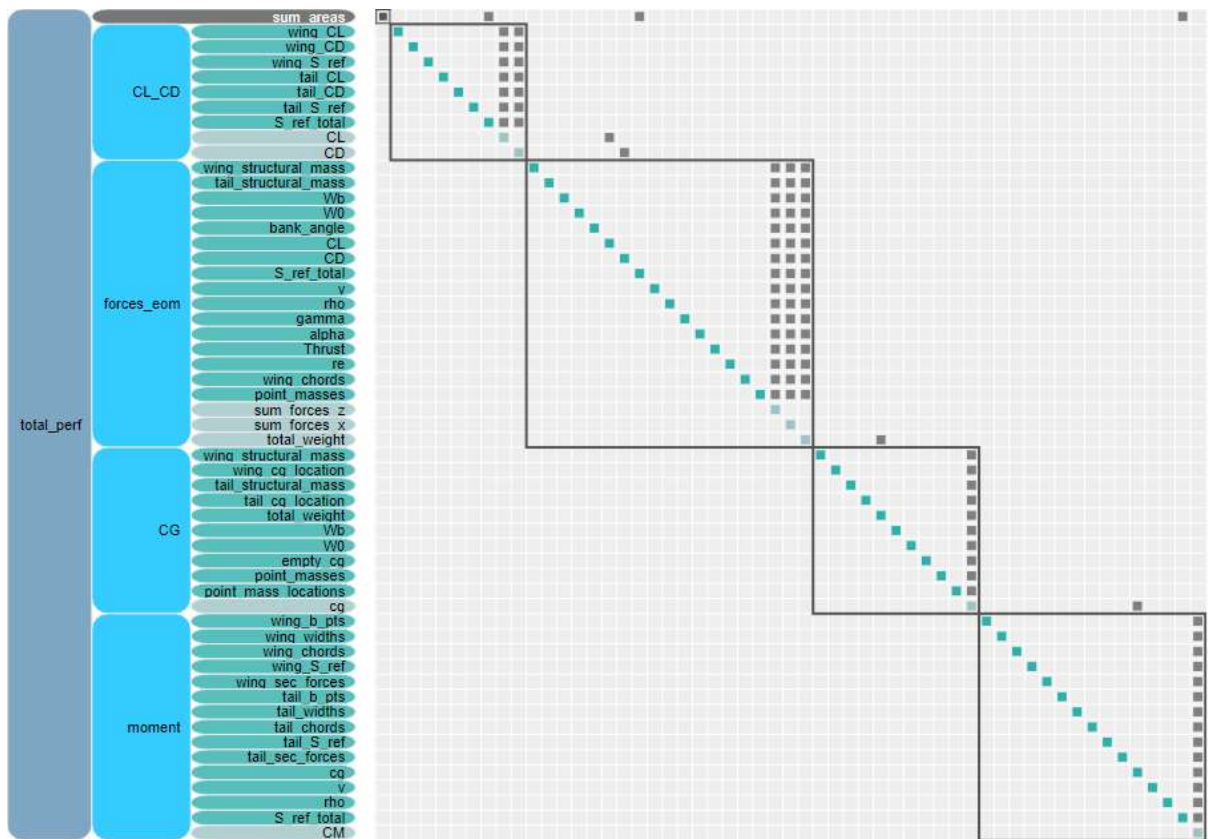Figure B.6: N2 diagram portion for the propulsion module.

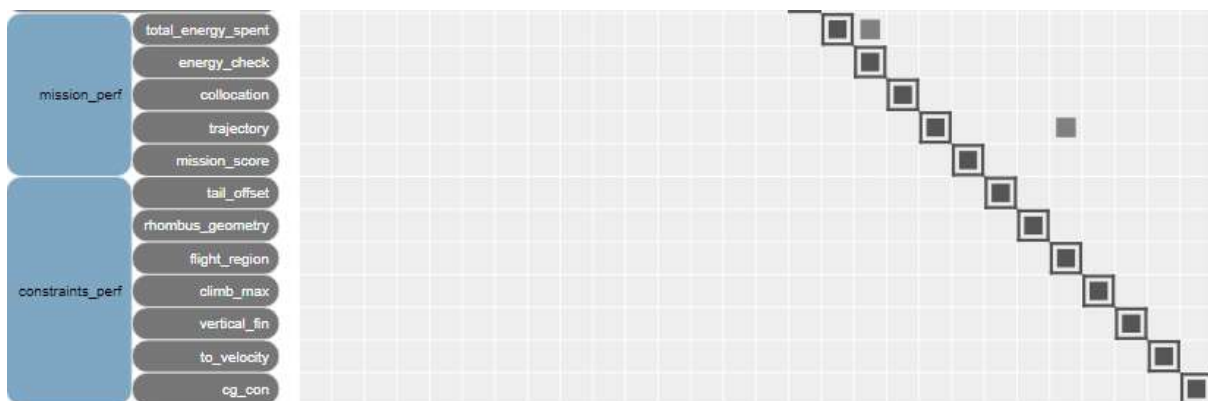Figure B.7: N2 diagram portion for each mission point performance module.

Figure B.8: N2 diagram portion for the mission performance and constraints.

Appendix C

Overall Results

C.1 Results Summary

Table C.1: Optimization results summary.

| | Single Optimization | | | | Global Optmization | | | | | | | |
| | | | | | #1 | | #2 | | | | #3 | |
	Ini	Climb	Distance	Payload	Ini	Opt	Ini	Opt	Ini	Opt	B-spline	Const. Power
Mass												
W_0 [kg]	1.345	1.362	1.497	1.472	1.345	1.466	1.437	1.388	1.460	2.719	1.789	1.798
W_p [kg]	0.100	0.364	0.180	2.996	0.100	3.561	2.000	1.692	2.400	1.871	1.537	1.810
W_b [kg]	0.200	0.200	0.200	0.200	0.200	0.200	0.200	0.200	0.200	0.200	0.200	0.200
CG_x [m]	0.000	-0.031	-0.053	-0.035	0.000	-0.022	0.000	-0.029	0.000	-0.120	-0.078	-0.074
Energy												
C_b [mAh]	2500	2778	2778	2779	2500	2778	2500	2778	2500	2781	2778	2779
Wing												
b_w [m]	1.80	1.38	1.54	1.80	1.80	1.80	2.00	1.17	2.00	1.85	1.80	1.80
$\overline{c_w}$ [m]	0.217	0.102	0.089	0.400	0.217	0.400	0.330	0.369	0.365	0.366	0.234	0.262
S_w [m2]	0.391	0.141	0.137	0.720	0.391	0.721	0.661	0.433	0.730	0.677	0.420	0.472
$\overline{\theta_w}$ [º]	0.0	0.0	0.0	0.0	0.0	0.0	0.0	0.0	0.0	0.0	0.0	0.0
t/c_w	0.10	0.10	0.12	0.08	0.10	0.08	0.10	0.08	0.10	0.12	0.11	0.10
Λ_w [º]	0.0	0.0	0.0	0.0	0.0	1.0	0.0	0.0	0.0	0.1	0.0	0.0
$\overline{t_{spar}}$ [mm]	0.15	0.46	0.98	0.17	0.15	0.15	0.15	0.15	0.15	0.97	0.60	0.54
$\overline{t_{skin}}$ [mm]	0.15	0.30	1.00	0.16	0.15	0.15	0.15	0.57	0.15	1.00	0.74	0.68
Tail												
b_t [m]	0.40	0.39	0.42	0.60	0.40	0.60	0.40	0.47	0.40	0.60	0.35	0.51
$\overline{c_t}$ [m]	0.125	0.077	0.060	0.250	0.125	0.250	0.125	0.174	0.125	0.172	0.199	0.134
S_t [m2]	0.050	0.030	0.025	0.150	0.050	0.150	0.050	0.082	0.050	0.103	0.069	0.068
Λ_t [º]	0.0	0.0	0.0	-0.1	0.0	-0.1	0.0	0.0	0.0	-0.1	-0.2	-0.1
τ_t [º]	35.0	35.0	35.0	35.1	35.0	35.2	35.0	35.0	35.0	59.7	59.3	59.4
t_{tube} [mm]	0.50	0.30	0.40	0.15	0.50	0.36	0.50	0.21	0.50	0.22	0.23	0.40
Score												
Climb	738.2	943.6	638.8	615.5	738.2	920.8	934.8	936.9	738.2	877.6	997.4	906.2
Distance	694.4	929.4	930.1	656.3	694.4	700.7	694.4	718.2	694.4	691.5	744.5	730.5
Payload	0.0	83.3	0.0	750.0	0.0	916.7	555.6	470.0	666.7	500.0	416.7	500.0
Total	1575.9	2151.9	1725.8	2224.0	1575.9	2792.0	2403.3	2337.6	2309.2	2275.9	2374.5	2350.4